TENSILE PROPERTIES, WATER ABSORPTION AND ENZYMATIC DEGRADATION STUDIES OF POLYETHYLENE/STARCH FILLED HYDROXYAPATITE BLEND FOR ORTHOPAEDIC APPLICATIONS

By

Bernard Owusu Asimeng, MSc (Hons.)

A Thesis submitted to the Department of Physics,

Kwame Nkrumah University of Science and Technology

in partial fulfillment of the requirements for the degree

of

DOCTOR OF PHILOSOPHY

(Materials Science)

College of Science

June, 2016.

Declaration

I hereby declare that this submission is my own work towards the PhD and that, to the best of my knowledge; it contains no material previously published by another person or material which has been accepted for the award of any other degree of the University, except where due acknowledgement has been made in the text.

Bernard Owusu Asimeng (PG6165011)

.....	.....	.....
Student Name & ID,	Signature,	Date

Certified by:

Dr. Bright Kwakye-Awuah

.....	.....	.....
Supervisor Name,	Signature,	Date

Certified by:

Dr. Elsie Effah Kaufmann

.....	.....	.....
Supervisor Name,	Signature,	Date

Certified by:

Prof. S. K Danuor

.....	.....	.....
Head of Dept. Name,	Signature,	Date

Acknowledgements

The story of this journey began like a dream, sometimes so easy and straight forward but difficult to interpret. A journey interspersed with difficult life events and frustrations. It is with such august gratitude that I honour and I acknowledge all those whose hand of support and words of encouragement guided me to achieve this dream - the end of this journey.

I, first of all, extend my profound gratitude to the Almighty God for His gifts of life, of what I am, and His endless love and forever enduring mercies.

I am greatly indebted to my late father, Mr Bernard Kofi Asimeng, for his passionate and unflinching belief in me as a child and for being the one whose dream, I share today. May his soul rest in eternal bliss. Also, the love of my family - the Asimeng family – is tremendous and in so many ways they have helped to sustain me. I could not have achieved without them and I am forever grateful.

May I say a big thank you to my supervisors, Dr. Bright Kwakye-Awuah (Department of Physics, KNUST) and Dr. Elsie Effah Kaufmann (Department of Biomedical Engineering, University of Ghana) for their consistent support, guidance and motivation. I just cannot fathom the completion of this project without their assistance. I am greatly indebted to them.

I extend my gratitude also to Dr. A Kuditure (Department of Physics, University of Ghana) for his excellent counsel and assistance in the XRD characterisation of samples. Furthermore, I greatly appreciate The Office for Research, Innovation and Development, University of Ghana, Legon, for their financial support awarded me through the Faculty Development Grant. This grant has been very invaluable in bringing this project to fruition. I also acknowledge Mr. Eric Tawiah at Metrology laboratory, KNUST for mould design and sample fabrication. I am thankful to Mr. Daniel Vincent Arthur, Mr. Barton Arkhurst and Rachel

Amanfu, all of Ghana Standard Authority for their permission and assistance to use the Titan tensile test machine.

I thank Mr. Shadrack Aseidu Coffie, Mr. Benjamin Otoo, and Mr. Kwaku Aquah all of Biotechnology Center, University of Ghana for their help in the acquisition of consumables and preparation of enzymatic solution for degradation studies.

Lastly I thank all staff members of Department of Biomedical Engineering for their persistent motivation, and a big thank you to my students; Mr. Edmund Aidoo Offei and Mr. Christopher Nyakpo of Department of Biomedical engineering, University of Ghana, Legon for their help in the computational model in COMSOL Multiphysics and in ChemDrew.

Abstract

Linear low-density polyethylene (LLDPE)/starch blends filled with hydroxyapatite have been synthesized by injection moulding. The aim was to control the rate of biodegradation of LLDPE/starch blends for bone screw fixation using hydroxyapatite (HA). Hydroxyapatite contents were varied from 1.0% to 3.0% in intervals of 0.5% by parts and the blend phases were characterised using X-ray diffractometry (XRD) and scanning electron microscopy (SEM). Biodegradation was studied by performing water absorption and enzymatic tests. Water uptakes by the samples were carried out according to ASTM D570 and enzymatic test was carried out on samples in phosphate buffered saline (PBS) containing α-amylase. Tensile properties of the samples before and after enzymatic degradation were determined using Titan and Testometric's universal testing machine while the surface changes were determined with Meiji Techno optical microscope. Seven different samples were formed for the study, two of the samples; one composed of LLDPE only and the other of 60% LLDPE, 40% starch and 0% hydroxyapatite, were used as controls. The results obtained show that the incorporation of starch granules into the LLDPE reduces the tensile strength but almost doubles the tensile modulus and this was attributed to starch granules expanding the amorphous tie chain of LLDPE. Addition of hydroxyapatite into the blend gave an increase in the tensile strength. The increase in strength with increasing HA content was statistically significant at a p-value of 0.0008 and the improvement slowed the rate at which the blend degraded. Hydroxyapatite is suspected to have affected the intermediate phase of the LLDPE by the hydroxyl group through hydrogen bonding. The water absorption by the blends showed that as hydroxyapatite content increased, the moisture uptake of the blends increased and enzymatic degradation rate increased, giving rise to high percentage loss in tensile strength and modulus. Conversely there was a high gain in

percentage elongation. Optical micrographs of the surfaces of the degraded samples showed surface erosion and agglomerates. The samples that showed higher erosion and more agglomerates had the highest water uptake and highest percentage loss in tensile strength and those with less erosion and fewer agglomerates had less water uptake and less percentage loss in tensile strength.

Table of Contents

List of Figures

List of Tables

List of Abbreviations and Acronyms

$\%Xtal$	Percentage crystallinity
$B_{inst.}$	Instrumental broadening values
ASTM	American society of testing and materials
BS EN ISO	British standard European norm and international standard organization
DSC	Differential scanning calorimetry
EHT	High tension voltage
EVA	Ethylene vinyl acetate
FWHM	Full width half maximum
HA	Hydroxyapatite
HDPE	High density polyethylene
LDPE	Low density polyethylene
LLDPE	Linear low density polyethylene
MR	Moisture ratio
PA	Polyamide
PBAT	Poly (butylene succinate-co-terephthalate)
PBS	Phosphate buffered saline
PBSA	Poly (butylene succinate)-co-(butylene adipate)
PCL	Polycaprolactones
PE	Polyethylene
PEA	Polyesteramides
PET	Polyesthylene terephthalate
PGA	Polyglycolic acid
PHA	Poly(hydroxyalkanoates)
PHB	Polyhdroxybutyrate
PHBv	Poly(hydroxybutyrate-co-hydroxyvalerate)
PLA	Polylactic acid
PLDLA	Copolymer of L-lactic acid and D – lactic acid

PLGA	Copolymers of L-lactic acid and polyglycolic acid
PM	Polarized light microscopy
PMMA	Poly(methylmethacrylate)
PVC	Polyvinyl chloride
RPM	Residual property module
SEM	Scanning electron microscopy
TEM	Transmission electron microscopy
TGA	Thermal gravimetry analysis
UHMWPE	Ultra high molecular weight polyethylene
VLDPE	Very low density polyethylene
XRD	X-ray diffraction

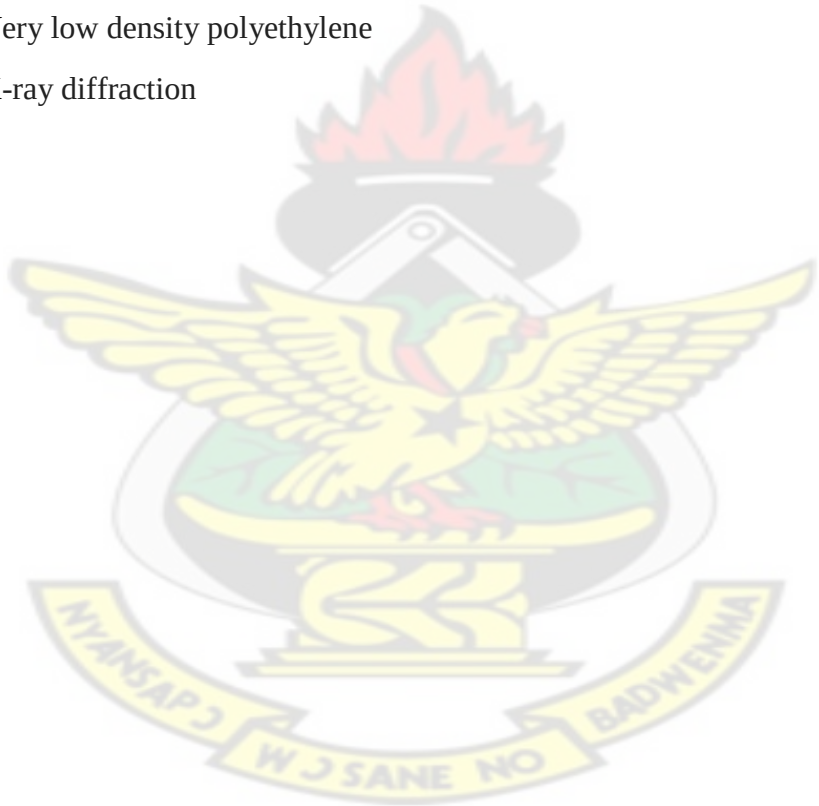

List of Symbols

$\dot{\gamma}^{(\alpha)}$	Viscoplastic shear rate
$\dot{\gamma}_a$	Distant shear rate
$\dot{\gamma}^o$	Reference strain rate
E_a	Rubbery shear modulus
F_{int}	Free energy of intermediate layer
G_a	Microdomain elastic modulus
M_d	Mass of specimen after immersion
M_w	Mass of specimen before immersion
P_∞	Residual property at infinity
P_o	Residual property value of dry specimen
P_r	Residual property value at current time
$R_{(\alpha)}$	Schmid tensor attributed to the slip system
R_o	Radius of microdomain unloaded state of amorphous layer
T_g	Glass transition temperature
f_d	Distortion free energy
$g^{(\alpha)}$	Shear strength of slip system
k_B	Boltzmann constant
l_{int}	Intermediate layer thickness
$m^{(\alpha)}$	Slip direction vector
$\dot{m}$	Strain rate sensitivity
m_e	Equilibrium moisture content
m_i	Initial moisture content
$n^{(\alpha)}$	Slip plane normal vector
β_L	Crystallite size broadening
β_e	Microstain broadening
ε_p	Porosity

η_a	Layer's viscosity
ν_a	Number of active polymer strands per unit volume
σ_c	Crystal stress
$\tau^{(\alpha)}$	Resolved shear stress acting on slip system,
τ_a	Shear stress acting on the amorphous phase of PE
χ_a	Volume fraction of the amorphous phase
χ_c	Crystallinity phase constant
χ_c	Volume fraction of crystalline phase
$\dot{\epsilon}$	Total strain rate
D	Diffusion coefficient
M	Instantaneous moisture content
R	Radius of microdomain in steady state shear
T	Absolute temperature
V	Intermediate volume
W	Workdone to shrink a microdomain
Δn	Density difference between two phases of PE
a	Proportionality coefficient
p	Pressure
u	Velocity fluid
β	Peak width of diffraction peak at FWHM
ε	Strain
κ	Permeability of medium
λ	Wavelength
μ	Fluid viscosity

Chapter one

Introduction

1.0 Background

Metallic implants have been extensively used for orthopaedic purposes but have quite profound drawbacks; their heavy weight and high corrosiveness affect their biocompatibility. Therefore, there has been much research into polymer-blends and composite materials as a better substitute to address these drawbacks.

Polymer-blends and composites present enormous potential for uses in bone replacement implants, tissue engineering scaffolds, bone cements and drug delivery systems (**Arutchelvi et al., 2008; Guo and Ait-Kadi, 2002; Marques et al., 2002**). The conventional plastics high cost and performance limitation has called for blending natural biodegradable polymers with non-degradable polymers. Starch is an extensively used natural degradable polymer because it is wholly biodegradable and less expensive when compared to other biodegradable polymers like polylactic acid (PLA), polyglycolic acid (PGA) and polyhydroxybutyrate (PHB) (**McGlashan and Halley, 2003; Yu et al., 2006; Zhang and Fazeli, 2010**). These biopolymers are completely biodegradable, but they degrade and lose the required strength needed for the application before tissue is remodelled. The novel way is to blend polyolefin (polyethylene) and starch to produce a bio-based material with controlled degradation and strength. Starch has retrogradation issues but since it has the same modulus as polyolefin, when blended introduces flexibility (**Babu and Seeram, 2013**). Starch was used as a filler of polyolefin in concentrations as low as 6 – 15% (**Lu et al., 2009**) but such a combination is not wholly biodegradable and not feasible for biomedical

application. This is because incorporating such low amounts of starch does not promote biodegradability of the implant or composite. Efforts to raise polyolefin (polyethylene) biodegradability have been studied by integrating 40% starch to a backbone matrix (**Alberta Araújo et al., 2004**). Microorganisms invade the blend surface since the surface area has been enriched, thus promoting biodegradation (**Arutchelvi et al., 2008; Avérous, 2004; Vroman and Tighzert, 2009**).

There is effective loss of mechanical strength since polyethylene is hydrophobic as opposed to a typical hydrophilic starch. The interfacial interaction between starch granules and polyethylene molecules is weak (**Matzinos et al., 2001; Sailaja and Chanda, 2001**). This behaviour is because of van der Waals forces emanating from saturated hydrocarbons (**Lohse, 2005**). Low degree of adhesion thus exist with high surface energy between the blends (**Fabunmi et al., 2007**). A stronger interaction between the polyethylene matrix and the starch fillers can be attained with destructive or gelatinized starches or in the chemically revamped form (**Fabunmi et al., 2007**).

Glycerol is normally used as a plasticizer to reduce torque during processing and this does delay degradation. In addition, it is believed that a small amount of bioactive filler such as hydroxyapatite (HA) which forms a major inorganic portion of bone can be introduced to improve tensile properties of the blend (**Bang Lee et al., 2000; Clarke, 2008; Wahl and Czernuszka, 2006**). Apatite is biocompatibility with periodontal ligament, osteoblast and fibroblast periodontal cells that are found in hard tissues. HA is evaluated as a modifying agent with several polymers such as starch PLLA, HDPE, PMMA, P (HB-HV) copolymers, PHB homopolymer and poly-ester-ester to form bioactive compounds (**Correlo et al., 2005**). HA particles disperse and distribute into the galleries of the blends and this changes the structure of

the blend as the molecules are entangled with the particles. Exfoliated and intercalated are basic structures that are formed (**Zhu and Narh, 2004**). Intercalation involves sometimes more than one particle inserted between the blend. This results in an ordered layer morphology. In the exfoliated structure the inorganic particles are totally distributed in a continuous matrix of the polymer (**Zhu and Narh, 2004**).The Young's modulus is strongly enhanced when nanoparticles are introduced and this depends on whether the structure is exfoliated or intercalated. Increasing inorganic content in a polymer may result in intercalation and the blend constituent may become immiscible and/or incompatible (**Ibos et al., 2011; Zhu et al., 1999**). Multiple phases in a structure are unwanted and can be stabilized during processing by addition of stabilisers or compatiblisers (**Guo and Ait-Kadi, 2002; Matzinos et al., 2001; Tokiwa et al., 2009; Cláudia et al., 2012**). The problems with stabilisers are that, they may either be toxic to organisms or slow down the rate of biodegradation of the material (**Arutchelvi et al., 2008**). It is therefore important to control phase separations and fabricate single phase blends for biological applications.

The individual polymer crystal structure has great influences on the mechanical properties of the blends. For example, polyethylene (PE) has two crystalline phases; orthorhombic unit cell and monoclinic unit cell. The orthorhombic unit cell overlaps with the second crystalline phase; monoclinic unit cell. The orthorhombic unit cell is easily seen with analytical techniques (X-ray diffraction or magnetic angle NMR spectroscopy), in commercial PEs a small portion of the monoclinic unit cell is only exposed during processing, that is when an excessive stress (trauma) is applied. However, the monoclinic phase is not stable and may disappear at temperatures below 60-80℃. It is believed that maximising the monoclinic phase improves the mechanical properties towards advantage (**Russell et al., 1997**).

In this work native cassava (*manihot esculenta crantz*) starch was introduced into linear low-density polyethylene (LLDPE) to maximise the monoclinic phase using hydroxyapatite as a reinforcing agent for bone screw fixation and hydroxyapatite content was varied to control biodegradation. LLDPE was selected among the polyolefin. LLDPE has a high draw-down ratio distinguished from LDPE of the same moulding density, its grades are tougher and stiffer at high temperatures than LDPE and HDPE. Furthermore, it has exceptional properties than polypropylene in terms of low impact. (**Rivero et al., 2009**). The blends were synthesized using injection moulding. Injection moulding was selected over extrusion since extrusion can partially or totally destroyed the semi-crystalline structure of native starches. It changes the double helical starch structures to a single helical one. This has been noticed by polarised light microscopy (PM), XRD and DSC (**van Soest et al., 1996**). The crystallinity is entirely destroyed and (**Sriburi et al., 1999**) hence negatively affects the mechanical properties (**Matzinos et al., 2001**).

1.1 Motivation for the Study

Metallic implants corrode *in-vivo* rapidly (earlier than expected) because the body fluids contain not only water but also delocalised ions, proteins and cells. This makes the implant environment; *in-vivo* more aggressive than in *in-vitro*. The corrosion affects both the implants and the body cells. The grain boundaries of the implants are attacked because biological entities prevent formation of a passivated oxide layer on the implant, by proteins blocking oxygen diffusion or cells influencing the local pH. The implants begin to wear due to pitting and this results in sudden failure. The wearing produces corrosion debris which causes Adverse Local Tissues Response (ALTRs) (**Joshua, 2012**). One of the ALTRs, is osteolysis, which often occurs in the proximity of an implant that either causes an immunological response or changes in the bone's

structure load. Patient's individual reaction to debris and the type of debris they are exposed is mainly caused by the nature and intensity of ALTR (**Joshua, 2012**). Another problem with metallic implants is stress-shielding. Here, the metallic implant's high Young's modulus compared to cortical bone causes a reduction of the normal stresses on the bone leading ultimately to bone atrophy. All these drawbacks suggest a need to remove metallic implants after bone remodelling but this imposes an extra cost and risk of a secondary surgery on the patient.

Bioinert and biodegradable polymers have been exploited in implant design. UHMWPE has been favourably developed with better wear resistance and is used in designing hip sockets and femoral heads of hip implants (**Kurtz, 2009**). UHMWPE's chemical and physical properties are unchanged with its application time (**Kurtz, 2009**). In applications such as pins, screws, bone fixation plates, biodegradable materials have been used. PGA and PLA and their copolymers are the current gold standard for biodegradable implants (**Pillai and Panchagnula, 2001**). PGA mechanical performance corresponds excellently to that of the bone but has poor degradation behaviour. The observed strength lost occurs between 30 and 60 days. PLA rather takes ten years for total degradation with an observed strength lost occurring after 180 days. Efforts to supress the drawbacks of these polymers is by blending with macromolecules such as starch, chitosan, chitin, fibrin, and others. The major challenge with these blends is that implants made from such blends can trigger inflammatory responses because of low molecular weight components that leach acidic products (**Dorozhkin, 2011**). There is therefore the need to develop bio-based materials from higher molecular weight polymers (e.g polyolifins) and macromolecules.

1.2 Objectives

This work seeks to propose a bio-based material for bone screw fixation using high molecular weight polymers from polyolifins (LLDPE) and macromolecules (starch) to eliminate metallic implants. This was done by using hydroxyapatite to mediate LLDPE/starch blend to control intermediate bonding and degradation. This material will eliminate stress shielding and corrosion posed by metallic implants as the Young's modulus is much lower than that of metals for this application and the material does not undergo corrosion. It is expected that hard tissue will infiltrate the pores vacated by macromolecules. To achieve this objective the following specific activities were conducted:

- hydroxyapatite particles were synthesised from bovine bone and particle size determined using Williamson-Hall plot in HighScore (Plus) 4.0.
- LLDPE/starch (40 wt %) blend and LLDPE/starch (40 wt %) blend filled with varying amounts of hydroxyapatite were synthesised using injection moulding, and the blends were characterized to determine their tensile properties. The tensile properties were interpreted based on XRD patterns and SEM images.
- water uptake and enzymatic degradation rate of the synthesized blends were determined and the mechanical degradation modelled using residual property module.

1.3 Thesis Layout

Chapter 1 acquaints the reader with some fundamental background understanding and applications of polyethylene crystal structure, polymer/starch, polymer/inorganic composites, and provides the motivation, and project objectives. **Chapter 2** provides a review on structure

and properties of polyethylene, starch and hydroxyapatite. The chapter continues to review various polymer/starch blends, starch enhancement of polyethylene biodegradation, Biodegradable polymer materials and implants, and analytical techniques of charactering biodegradation. Water absorption theories are also considered. **Chapter 3** gives the detailed experimental methods of this research; these include synthesis and design procedure of samples, characterization techniques and sample testing technique used. **Chapter 4** reports on the results obtained from various characterizations and testing techniques. **Chapter 5** discusses the results presented in chapter 4 and **Chapter 6** draws conclusions on the major findings obtained in this project and provides recommendations for future work.

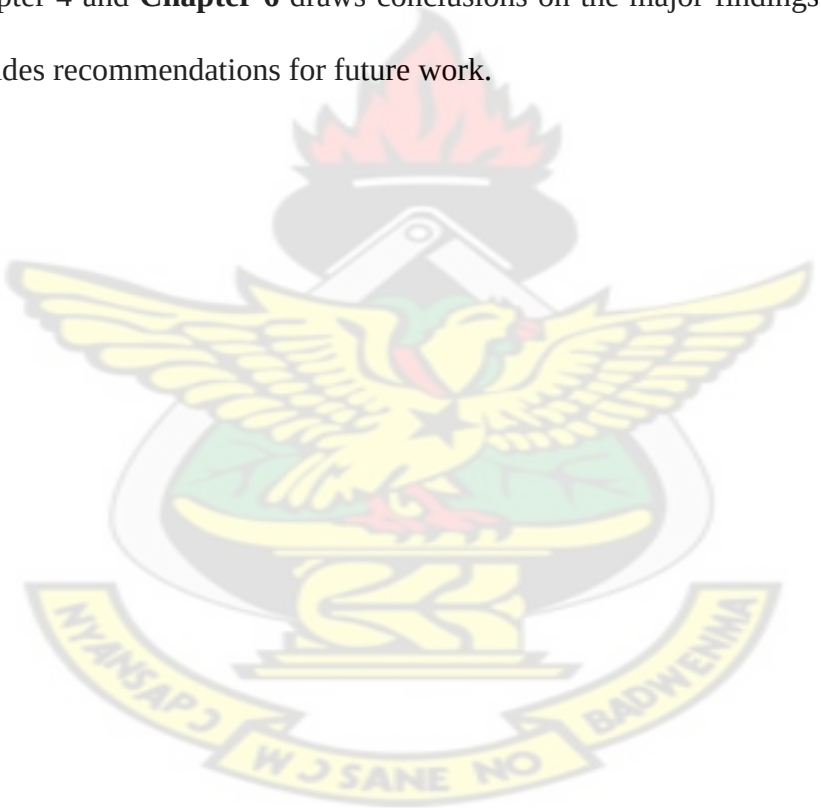

Chapter two

Literature Review

2. 1 Semi-crystalline Morphology of Polyethylene

Polyethylene (PE) is a polyolefin and it is among the second largest group of materials which is applied in various fields worldwide. Polyolefins are characterized by unsaturated double-bond, which describes alkene series with non-polar backbone. The unsaturated double-bond characteristic of alkene series with non-polar backbone is known by the term polyolefin **(Subramanian, 2013; Nwabunma and Thein, 2008)**.

Polyethylene is a semi-crystalline material which is made up of three phase morphology. A crystalline phase bounded by a non-crystalline phase. The third phase is a partly ordered layer adjoining the crystalline phase and the non-crystalline phase (amorphous phase) in the intervening spaces as illustrated schematically in **Figure 2.0**. The crystallites are separated by the non-crystalline region, and this between 50 Å to 300 Å approximately **(McFaddin et al., 1993; Simanke et al., 2001; Sajkiewicz et al., 2005; Peacock, 2000)**. The third phase is a transition phase (intermediate component) which adds up to the crystalline and amorphous phases. The transition phase plays the role of an interface and how to tailor made PE's of appropriate rigid interface, has been a subject of discussion **(Kolgjini et al., 2011)**. Raman spectroscopy analysis revealed that chains involved in the transition phase are in anisotropic disordered form but are stretched in non-lateral order.

The concept of semi-crytallinity is of great significance because polyethylene can be regarded as a composite of amorphous and crystalline regions. PE that consists solely of

crystalline matrices would be a friable material and wholly amorphous sample would also be a very viscous fluid. A major contributor to the mechanical property of semi-crytalline polymer is the crystalline phase, which usually improves their stiffness. It is quite difficult to predict these properties because the arrangement of the three phases with respect to each other, their relative proportions, and their degree of connectivity determine their properties, rather its quite practicable to determine the mechanical properties of amorphous polymers. The properties of both pure crystalline and pure amorphous polymers is derived from partially crystalline samples because, samples of pure crystalline and pure amorphous is not readily available.

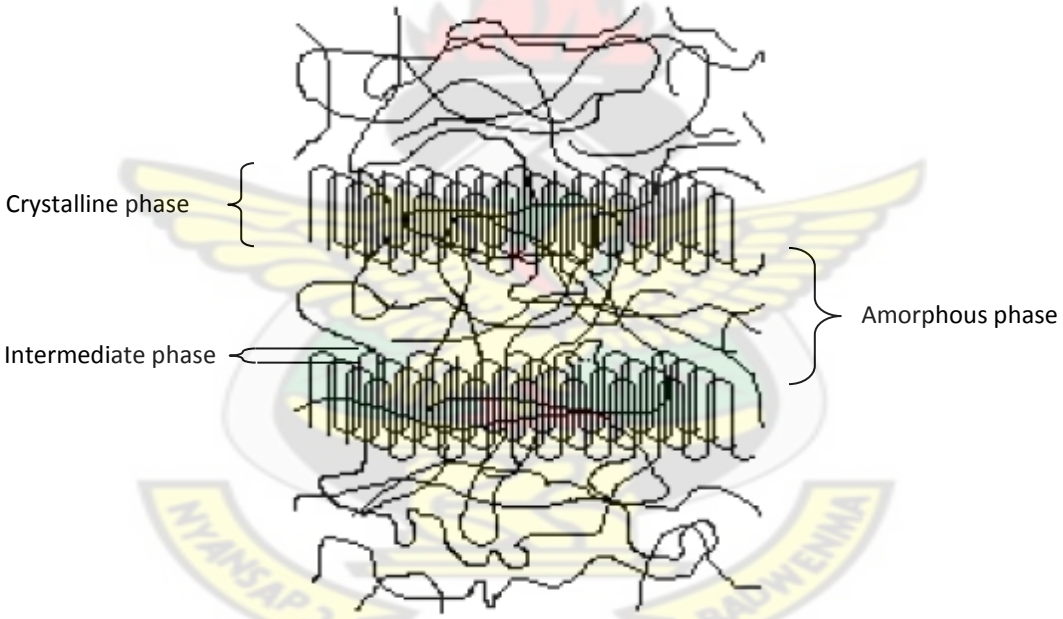

Figure 2.0 Representation of the three phases present in solid polyethylene.

Given the estimated properties of each phase and assuming a model of connectivity via the interface, it is possible to explain the mechanical behaviour of polyethylene samples. To carry out this type of analysis it is desirable to have an accurate knowledge of the relative proportions of each of the three phases. In practical situations, the degree of crystallinity is frequently used to

characterize the semi-crystalline nature of polyethylene samples. Quantification of the three phases of polyethylene can be made experimentally. **Kolgjini et al., (2011)** have been able to characterise a cold-drawn LLDPE three phase morphology using Raman spectroscopy, differential scanning calorimetry, and X-ray measurement. Some of the most commonly used and most important descriptors of a polyethylene sample, such as density and stiffness are closely related to its crystallinity level. The high crystallinity (between 70% and 80%) and crystal slip systems that exist in high-density polyethylene (HDPE) **(Yang & Chen, 2001)** makes it suitable for most of the micromechanical constitute model for polyethylene.

2. 1.1 Micromechanical Constitutive Modeling of PE

Theoretically, the microstructure of PE can be studied as a two-phase composite; entangled amorphous layers separating flat crystalline lamella (**Sedighiamiri et al., 2011**; **Men et al., 2003**). Since HDPE has enough crystalline peaks than the other examples of PE, it has enough slip planes for constitute models hence HDPE is used for such models for PE. The lamellae are found in unstrained melt solidified PE which is outspreading in structures of spherulitc, hence rendering the material macroscopically isotropic **(Gleiter, 2000**).The crystals of PE are developed through the folding and linking of long polymer molecule consisting of regularly ordered chain segments in an orthorhombic packing. However distinct morphologies are emerged during processing (melt solidification) depending on the strain rate produced and the temperatures at which the melts are crystalline; normally occurred undercooling. If the crystallization temperature of the melt is high and the strain rate is small then a stacked lamellar morphology is produced (see **Figure 2.1**(a)), a higher crystallization temperature with a higher strain rate gives a needle-like arrangement (**Figure 2.1**(b)).Crystallization at reduced

temperatures and a higher strain rate results in oriented micellar structure (see **Figure 2.1**(c)). The morphological evolutions occurring during the melt solidification is endless and combinations of the melt conditions could also evolved different morphologies (see **Figure 2.1**(d)) (**Gleiter, 2000**). In contrast, the main present accepted methods of amorphous phase deformation in semi-crystalline polymers are interlamelar separation, stack rotation, and interlamellar slip. Shear forces when applied in the opposite and parallel to the lamellar causes interlamellar slip. Consequently, the amorphous phase undergoes shear. The method of straining is presented in **Figure 2.2 (a)**. Interlaminar slip is a comparably easy way of deformation for materials beyond the glass transition temperature (Tg). Reversible interlamellar slip can be explained comprehensibly by the elastic region of the deformation.

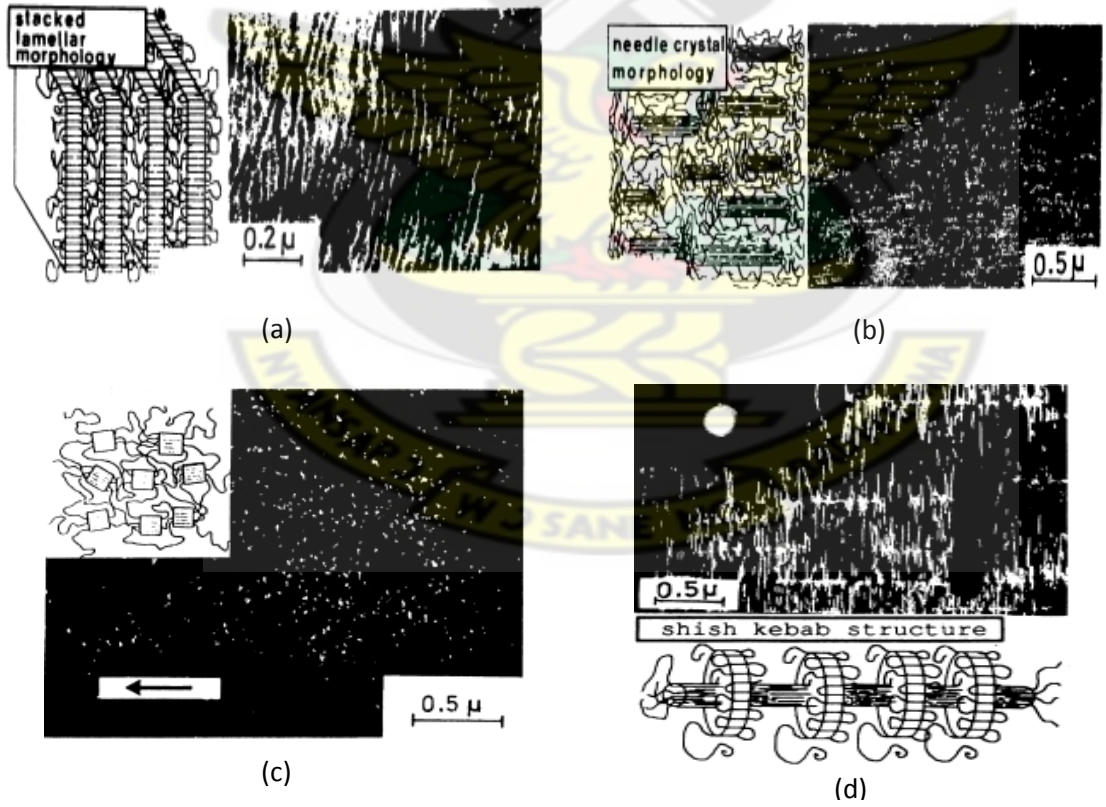

Figure 2.1 (a) Stacked lamellar morphology in polyethylene (TEM bright field) (b) Needle-like morphology in polybutene-1 (TEM bright field). (c) Oriented micellar morphology in polyethylene terephthalate (TEM dark field micrograph). (d) Shish-kebab morphology in is isotactic polystyrene (TEM dark field micrograph) (Petermann, 1991)

Consequently, the amorphous phase undergoes shear. The method of straining is presented in **Figure 2.2** (b). Interlaminar slip is a comparably easy way of deformation for materials beyond the glass transition temperature (Tg). Reversible interlamellar slip can be explained comprehensibly by the elastic region of the deformation. Stack rotation is presented schematically in **Figure 2.2** (c). It is required to have the lamellae in the form of stacks; fused in the amorphous matrix. When subjected to applied stresses, it promotes free rotation. A shift in the crystalline lamellae is required in all other forms of deformation of the amorphous phase. The deformation in the amorphous phase is determined by the extent of deformation of the crystalline phase (**Galeski, 2003**).

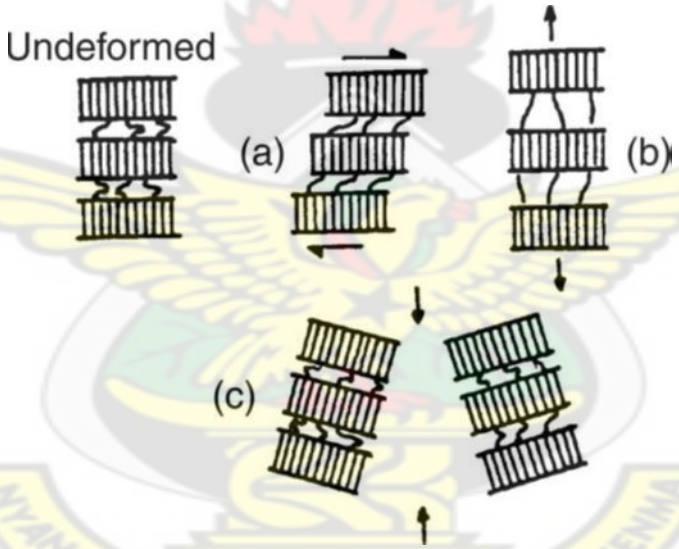

Figure 2.2 Deformation modes of the amorphous phase in semicrystalline polymers: (a) interlamellar slip, (b) interlamellar separation, (c) rotation of stacks of lamellae (Galeski, 2003).

Polymer crystals also undergo large plastic deformations despite the fact that they are in their solid state. Thermoforming and spinning; with a post drawing operations, are some of the ways of achieving large plastic deformations of solid polymers. The technique does not only points to modifications of the material shape but also introduces cavitation and voiding leading

to structural evolution probably resulting from crystallinity increment or a cleavage and re-position of the crystalline phase (**Thévenon and René, 2014**). Cystallographic slip is the primary deformation mechanism in polymer crystals (**Bowden and Young, 1974**), which take place on privileged planes (**Table 2.0**) and in (110) and (310) twinning systems (**Lee et al, 1993)**. **Lee et al., (1993)** employed a micromechanical based-composite model to study large plastic strain plastic deformation, the findings add to the fact the mechanical properties are affected by the changes in structure. Nevertheless it is complicated to develop thermomechanical models for semi-crystalline polymers (**Thévenon and René, 2014**).

Table 2.0: slip systems and corresponding slip resistances for HDPE (Nikolov and Issam, 2000).

Slip system	$g^{(\alpha)}$ (MPa)
(100) [001]	8
(010) [001]	20
{110} [001]	20
(100) [010]	13.3
(010) [100]	20
{110} >$\langle 1\bar{1}0 \rangle$	17.6

Nikolov and Issam (**2000)** took into account the micromechanical model of interlamellar shear with the consideration of a fundamental cell made of a pile of parallel lamellae along with their corresponding amorphous layers. (**Figure 2.3**). As **Figure 2.3** depicts, the normal unit vector to the lamellae surfaces is represented by 'n' with 'c' being the unit vector of the direction of PE molecules in the lamellae. The chain orientation obtained from an experiment makes an angle of 17 to 40° with the normal vector (**Lee et al., 1993**). In their model (**n**, **c)** = 30°. For ease of handling with the total performance, *inclusion* was define for the stacked lamellae and the corresponding amorphous layers. χ_c denotes the total crystallinity of the

polymer, which is the crystalline phase content. PE is assumed to have unchanging density with Poisson's ratio, n = 0.41 **(Lee, Argon, et al., 1993)**. For any given inclusion where interlamellar separation is desired, a flow of amorphous region into the crystalline region is highly required to cause the interlamellar separation.This will lead to deformations such as microcavities leading to introduction of small strains. It is expected that these small strains produced will not yield cavitation in the PE and hence, this method of deformation would be a minor contributor to the net strain. However, deformation of PE can only be achieved by slip on well-defined planes since it is regarded as a combination of inclusions distributed haphazardly. Consequently, a pile of lamallae can accommodate an arbitrary deformation however that is not the case in single polymer crystal due to the inflexibility of polymer crystals in directions parallel to the chains. Therefore, the inclusion of PE has five separate slip systems, and this helps it to withstand any form of loading **(Nikolov and Issam, 2000)**.

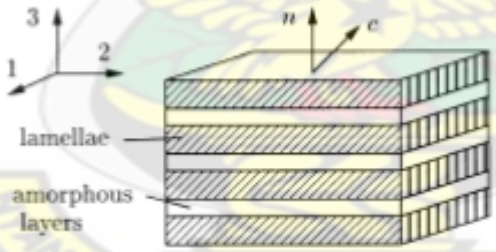

Figure 2.3 The basic structure unit of two-phase composite inclusion of PE (Nikolov and Issam, 2000).

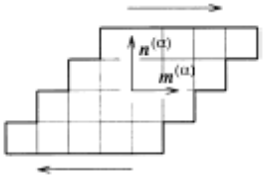

Figure 2.4 Shear deformation of a single crystal (Nikolov and Issam, 2000; Séguéla, 2007).

2. 1.1.1 Crystalline Phase

The small-molecule crystals constitutive relations is used to modeled the crystalline phase deformation in PE. For simple understanding, **Nikolov and Issam** in **2000** assume that the crystalline phase consists of rigid-viscoplastic crystallites. Consider a crystal with one crystal structure. Stresses acting on a particular slip system (α) is the resultant shear stress, $\tau^{(\alpha)}$ defined as follows **(Lemonds et al., 1985)**:

$$\tau^{(\alpha)} = \sigma_c : R^{(\alpha)}, \tag{2.1}$$

where σ_c is the stress in the crystal and $R^{(\alpha)}$ is the Schmid tensor attributed to the slip system (α):

$$R^{(\alpha)} = \frac{1}{2}\left(n^{(\alpha)} \otimes m^{(\alpha)} + m^{(\alpha)} \otimes n^{(\alpha)}\right) \tag{2.2}$$

where $n^{(\alpha)}$ and $m^{(\alpha)}$ are the "slip plane" normal vector and the "slip direction" vector, respectively (**Figure 2.4**). For rate-dependent materials, the resolved shear stress $\tau^{(\alpha)}$ can be related to the corresponding shear rate, $\dot{\gamma}^{(\alpha)}$ via a power law expression:

$$\dot{\gamma}^{(\alpha)} = \dot{\gamma}_{\circ} sinh(\tau^{(\alpha)} \left|\frac{\tau^{(\alpha)}}{g^{(\alpha)}}\right|^{1/m}), \quad (2.3)$$

where $\dot{\gamma}_{\circ}$ is a reference strain rate, $g^{(\alpha)}$ is the shear strength of the slip system (α) and m is the strain rate sensitivity. **Equation (2.3)** suggests that plastic flow is always present on the slip system (α) as long as the shear stress $\tau^{(\alpha)}$ is not identically equal to zero, but if $\left|\tau^{(\alpha)}\right| \leq g^{(\alpha)}$ the viscoplastic shear rate $\dot{\gamma}^{(\alpha)}$ is negligible. The total strain rate in the crystal is:

$$\dot{\epsilon}_c = \sum_{\alpha} \dot{\gamma}^{(\alpha)} R^{(\alpha)}, \quad (2.4)$$

where α represents the slip systems of PE crystallites. **Table 2.0** provides a list of the slip systems for HDPE and its associated slip resistances at room temperature. The slip resistances are affected by the following; lamellar thickness, normal stress acting on the slip planes and temperature **(Lee, Parks, and Ahzi, 1993; Pawlak and Galeski, 2005)**. The thickness of the lamellar (5-25 nm) implies, dislocations can undergo displacement on lamellar surfaces with ease due to thermal processes that activates the slip systems. Therefore, the model fails to include strain-induced hardening of slip systems. Clearly, the normal stress values change as the slip resistances. Dislocation theory postulates that the mean lamellar thickness varies proportionally to the weakest resistance, the higher the resistance, the thicker lamellae. At reduced temperatures and above relaxation temperature of about 60, there is significant deviation from the experimental results, but the theory gives acceptable results at room temperatures.

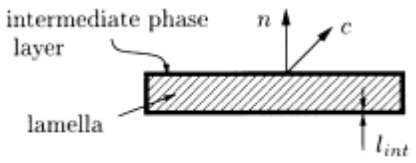

Figure 2.5 Intermediate phases in PE

Nikolov and Issam (2000) explain the role of the transition phase joining the amorphous layers and the crystalline lamellae in the yield behaviour of PE. The propagation of the screw dislocations along the lamellae c axis and nucleation contributes to the yielding. The density gradient in semi-crystalline polymers which results from spatial inhomogeneity in density and/or orientation, results in chain folding on lamellae surface. The chains most of the time bends more in one direction of the lamellae surface than in the other, this provides a density difference between the crystalline lamellae and amorphous layers, thus resulting in entropy loss. Hence, intermediate phase is isolated by wrapping with a layer membrane from every crystalline lamella in semi-crystalline structure (see **Figure 2.5**). The intermediate layer free energy, for a given lamella is defined by the difference in density between the two phases, $\Delta \boldsymbol{n}$ the thickness of the layer, $\boldsymbol{l_{int}}$ and the intermediate layer volume V, is given by:

$$F_{int} = \frac{aTV\Delta n}{l_{int}^2}, \tag{2.5}$$

where **T** is the temperature and $\boldsymbol{a}$, the proportionality coefficient.

Considering a membrane stress state, σ in the intermediate phase layer, its surface tension can be calculated as:

$$\sigma = \frac{F_{int}}{V} = \frac{aT\Delta n}{l_{int}^2}, \tag{2.6}$$

Alamo et al., (1994) measured the intermediate phase volume fraction, V and it has been shown that V changes with crystallinity and thus relate directly to the intermediate layer thickness. A decrease in the intermediate phase volume fraction corresponds to an increase in the overall crystallinity, and thus causes an increase in surface tension as a result of thinner intermediate layers. The yield behaviour of PEs can be explained by the failure of the intermediate phase, at the second yield point localized lamellar-to-fibrillar and localized coarse slip (see **Figure 2.6**) transition occurs. The dislocation theory can be used to explain the first yield point, as it is more sensitive to crystallinity. The function of intermediate phase is to prevent them from localized deformation and also to provide a homogeneous slip in the lamellae.

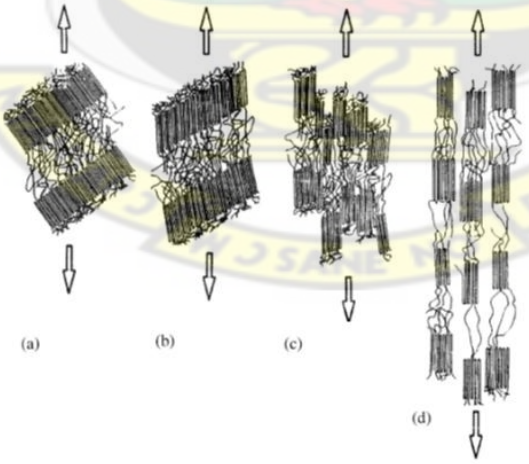

Figure 2.6 Morphology changes during lamellae stack deformation in a tensile test, after (Schultz, 1974): (a) interlamellar shear; (b) interlamellar shear plus fine slip in the crystals; (c) coarse slip plus initiation of lamellae breakage; (d) fibrillar state with residual crystalline block portions. Arrows show the loading direction. The imposed deformation increases from left to right.

2. 1.1.2 Amorphous Phase

The amorphous phase layers cannot be easily isolated from the bulk polymer phase for independent study. This makes the microstructure obscure so a complex microstructure with orderly arranged microdomains has been defined to elucidate large viscoplastic deformation of the amorphous phase of HDP. The idea is similar but looks different in context to small plastic deformation behaviour modelled by **Nikolov and Issam (2000)**. The crystalline lamellae of thin layers with thickness, 10 nm imposes high stresses on the ordered microdomains in the amorphous phase. This is modelled in the molten state at room temperature and the relationship between the shear rate and the shear viscosity determined during deformation. Distortions arising from deformation produced viscoelastic stresses as a result of resistances of the ordered microdomains. The stress applied due to coincidently stretching and releasing of polymer fibers or by repeating of polymer molecules in a tube of neighbouring molecules comprehensively explains the viscoelasticity of homogeneous polymer melts. These processes cannot be adopted for shearing of thin layers that are confined in lamellae. Distortion elastic constant of molecules is introduced to give back a contrasting mechanism of viscoelasticity. The fundamental inference here is that each amorphous layer is created as a polydomain structure (**Figure 2.7**) with each microdomain possessing a local free energy minimum.

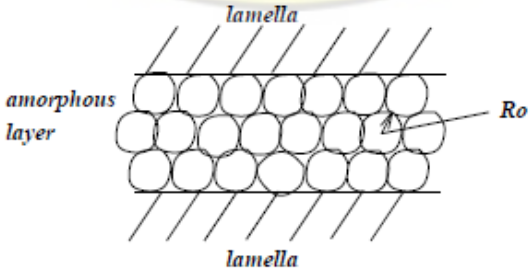

Figure 2.7 Amorphous layers microstructure

Prior to loading, the orientations of the chain segments in a particular microdomain were not considered. The continuum theory of nematic class of liquid crystals give the distortion free energy, $\boldsymbol{f_d}$ of the micro domain chains per unit volume as:

$$\boldsymbol{f_d = \frac{K}{R^2}} \tag{2.7}$$

where K is the average elastic constant of distortion of a single micro domain, R is the radius of the microdomain. The distortion elasticity of polymer molecule relates to K and is dependent on the following: the molecular structure and temperature.

There is usually a change in the radius of the domains from $R_\circ$ in the unloaded state to R in the steady state ($R_\circ$>R) whenever there is an application of shear rate ($\dot{\gamma}_a$) to the amorphous layer eventually causing an increment of distortion energy in the layer. The growth of micro domains is inversely proportional to their radius as stated in the conservation of volume

$$\frac{K}{R^2} - \frac{K}{R_\circ^2} = \eta_a \dot{\gamma}_a, \tag{2.8}$$

where η_a is the layer's viscosity.

Based on these conditions, the domain radius in steady state shear, R should be dependent on the applied shear rate. In order to establish a relation between $R_\circ$, R and $\dot{\gamma}_a$ we introduce the probability for a microdomain, subjected to distant shear rate, $\dot{\gamma}_a$ to have radius R as $P = \frac{R}{R_\circ}$ thus expecting that at equilibrium $P|_{\dot{\gamma}_{a=0}} = 1$. When the interaction between the microdomains is ignored, then according to statistical mechanics, P can be expressed as

$$P = exp\left(-\frac{W}{k_B T}\right) \tag{2.9}$$

where W is the energy (or work) necessary to shrink the microdomain to radius R, k_B is the Boltzmann constant and T the absolute temperature. We assume that W is a power law function of $\dot{\gamma}_a$ and **Equation (2.9)** can be rewritten as:

$$R = R_\circ exp\left(-\frac{\alpha \dot{\gamma}_a^n}{K_B T}\right) \tag{2.10}$$

where $W = \alpha \dot{\gamma}_a^n$ is the "shear rate sensitivity" of the microdomains and α is a proportionality constant. Introducing **Equation (2.10)** in **(2.8)** we write the shear viscosity of the amorphous phase as:

$$\eta_a = \frac{K}{(R_\circ)^2 \dot{\gamma}_a}\left[\left(exp\frac{2\alpha \dot{\gamma}_a^n}{K_B T}\right) - 1\right] \tag{2.11}$$

When computed numerically the equation above is equivalent to the shear thinning power-law function $\eta_a = C\dot{\gamma}_a^m$ up to extremely high strain rates where a plateau of $\eta_a(\dot{\gamma}_a)$ is attained.

Not only do they experience shrinkage, the microdomains slide past each other. The elastic modulus G_a resulting from microdomains' slip is given as:

$$G_a = \frac{K}{RL} = \frac{K}{R_\circ L} exp\left(\frac{\alpha \dot{\gamma}_a^n}{K_B T}\right), \tag{2.12}$$

where L is the persistent length of the polymer molecule (The maximum chain length which can be regarded as part of a straight line). However the G_a depends on $\dot{\gamma}_a$ through R even though there has been an established assumption of a linear relation between shear stress and strain Note that despite the assumption of a linear relation between shear stress and strain, G_a depends on $\dot{\gamma}_a$ through R.

It is presupposed that upon shear, there is an instantaneous drop in the microdomains' radius from R_o to R. This is a reasonable approximation because of the low energy required to shrink microdomains. R will however, increase to its equilibrium value R_o through thermal diffusion, when the deformation is suddenly frozen in a relaxation test, but this process would involve more time than shrinking upon exertion of external force.

It is a known fact that two neighbouring lamellae are connected through entangled chains anchored on lamellae surface upon straining the rubber-like stretching of the polymer molecules which will produce elastic stress in the amorphous phase, and also through numerous tie molecules passing from one lamella to another. Neo-Hookean constitutive equation can be used to model the entropic elasticity at small strains. The only material parameter needed is the rubber shear modulus, as a result of the incompressibility, which at microlevel is given as;

$$E_a = \upsilon_a K_B T \tag{2.13}$$

with υ_a being the number of the active polymer strands per unit volume.

So far, the parameters which should enter in the amorphous phase has been dealt with in the constitutive equation. In order for the above equations to be derived, additional hypotheses needs to be backed by experimental results.

A well-known three-element rheological model of **Figure 2.8** can be developed by a viscoelastic constitutive model for the amorphous phase. The viscoelastic semi-crystalline polymer is described by a slight modification of this model, which is called the overstress theory. Holding the usual assumption constant, the following differential equation relates the strain, **Ga** and the shear stress, $\boldsymbol{\tau_a}$ acting on the amorphous phase is found by

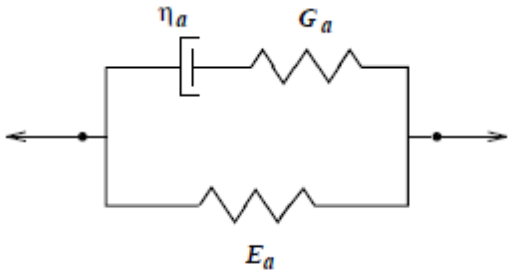

Figure 2.8 Three-element rheological models for the amorphous phase behaviour.

$$\tau_a + \eta_a \frac{\partial}{\partial t}\left(\frac{\tau_a}{G_a}\right) = E_a\gamma_a + \eta_a\left[\dot{\gamma}_a + \frac{\partial}{\partial t}\left(\frac{E_a}{G_a}\gamma_a\right)\right] \quad (2.14)$$

where a superposed dot denotes a time derivative. If the coefficients Ea and Ga are constants, then **Equation (2.14)** reduces to the three-element linear viscoelastic model:

$$\tau_a + \left(\frac{\eta_a}{G_a}\dot{\tau}_a\right) = E_a\gamma_a + \eta_a\left(1 + \frac{E_a}{G_a}\right)\dot{\gamma}_a \quad (2.15)$$

However, the strain rate, $\dot{\gamma}_a$ depends on the elastic modulus and therefore it is not constant according to **equation (2.15)**; accordingly, the differential equation as presented in **equation (2.14)** in the general form is used. Except when the material is loaded with $\dot{\gamma}_a$ = constant from stress-and-strain-free state, where **equation (2.14)** does not reduce to the linear case.

2. 1.1.3 Constitutive Equation of a Single Inclusion

By assuming uniform stress, the constitutive equations of the inclusion can be developed.

This approximation is most appropriate for laminate composite that are subjected to off-plane shear. Let χ_c be the volume fraction of the amorphous layers and χ_a be the volume fraction of the crystalline phase. Therefore, the total shear in the inclusion is given by;

$$\dot{\epsilon}_I = \chi_c \dot{\epsilon}_c + \chi_a \dot{\epsilon}_a \tag{2.16}$$

2.2 Polyethylene Crystal Unit Cell

The unit cell is the smallest entity in a crystal that contains all the information that is needed to construct a complete crystal in crystallographic terms. Unit cells consist of parallelepipeds such as cuboids and rhombohedrons, containing a small number of atoms. The lattice parameters describes defines the unit cell. These are the angles and the lengths $(\boldsymbol{\alpha}, \boldsymbol{\beta}, \boldsymbol{\gamma})$ and $(\boldsymbol{a}, \boldsymbol{b}, \boldsymbol{c})$**,** respectively as illustrated in **Figure 2.9**. The positions the atoms occupy inside a unit cell can be depicted by a set of atomic positions $(\boldsymbol{x_i}, \boldsymbol{y_j}, \boldsymbol{z_i})$ measured from a selected lattice point. A complete crystal can be constructed from a unit cell by translating it repeatedly along each of its axes a distance equal to the length of that axis. The result of this process is shown in **Figure 2.10**. The unit cell of most non polymeric compounds contains an integral number of complete molecules. In contrast, polymeric unit cells contain short segments from one or more molecular chains by convection, the **c** axis of a polymeric unit cell is designated as being parallel with the chain axis of its molecular segments **(Peacock, 2000)**.

In general, the structure of most polymers are relatively complex as compared to polyethylene which exhibits three types of unit cells, - hexagonal, orthorhombic and monoclinic (or triclinic). The most common unit cell is orthorhombic, for all practical purposes, it may be considered as the only one present in commercial samples **(Peacock, 2000)**.

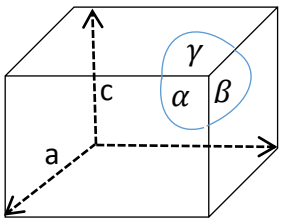

Figure 2.9 Generic Unit cell.

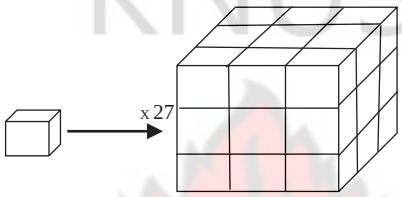

Figure 2.10 Crystal matrix built up by translating a unit cell.

2.2.1 Orthorhombic Unit Cell

The orthorhombic unit cell is cuboid, the angles made by the adjoining faces are all 90° whiles each of its axes has a different length. An orthorhombic unit cell comprises of parts of four surrounding chain segments and one complete chain segments of ethylene unit, for a total of two chains per unit cell. This is variously illustrated in **Figure 2.11**. The dimensions of the, *a*, *b* and *c* axes of an unperturbed polyethylene unit cell are reported to be 7.417 Å, 4.945 Å, and 2.547 Å, respectively **(Peacock, 2000; Li et al., 2001)**. These values were measured for high density polyethylene at room temperature. The density of a unit cell with these dimensions is 1.00 g/cm^3. This value is widely accepted and is commonly used in the calculation of the degree of crystallinity from sample density **(Peacock, 2000; Askeland & Phulé, 2003)**.

The dimensions of the orthorhombic unit cell are not constant. Linear low density polyethylene and low density polyethylene polyethylene have larger *a* and *b* axis dimensions than high density polyethylene, while the length of the ***c*** axis remains essentially constant **(Peacock, 2000; Gedde & Alessandro, 2004)**. **Watanabe et al** in **2009** studied the surface melting and lamina rearrangements of PE. Infrared spectroscopy together with 2-D spectral correlation spectroscopy are employed to study the structural disordering process as heat is applied. There is structural rearrangement of the orthorhombic crystals in all PEs with the exception of low-crystalline LLDPE. The heating process caused conformational defects to the side chains of PEs loaded with the orthorhombic crystals rather than in low-crystalline LLDPE. Small-angle x-ray is used to observe temperature dependence in the thickening of lamella layers of LLDPE. The temperature ranges where surface melting and lamellar thickening occurs are observed. Lamella rearrangement formed new orthorhombic crystals which dominates over the structural defects in LLDPE while other PE specimens show the contrary **(Watanabe et al., 2009)**. Thermodynamic calculations support the hypothesis that branches larger than a methyl group cannot be accommodated by the crystal lattice without its disruption. However, it is clear that the extent of expansion of the unit cell is link with comonomer content of the sample. A possible explanation of the unit cell expansion involves the concentration of short-chain branches in the interfacial regions due to their exclusion from crystallites. The high concentration of branches causes overcrowding of the interface, resulting in the underlying crystallite expanding slightly to relieve the steric interference.

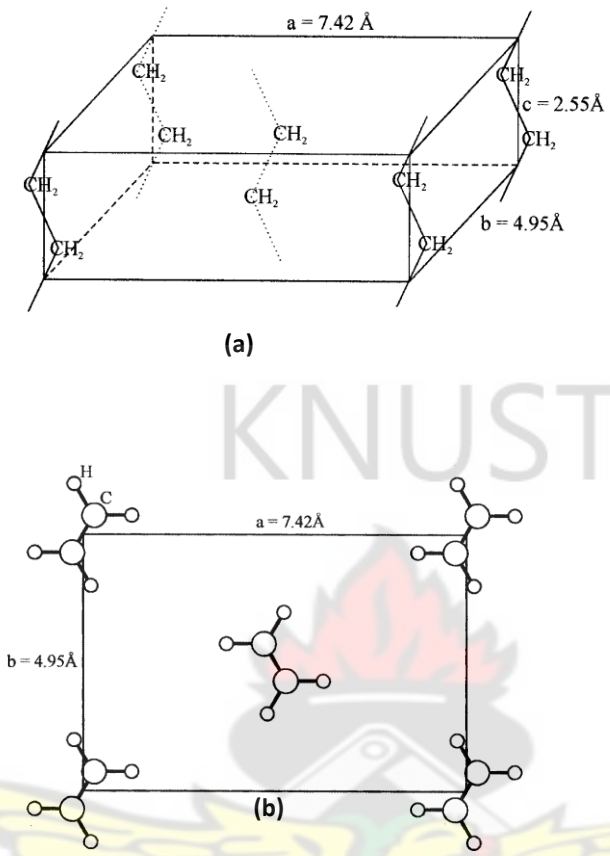

Figure 2.11 Polyethylene orthorhombic crystal habit. (a) Orthogonal view; (b) view along the *c* axis (Peacock, 2000).

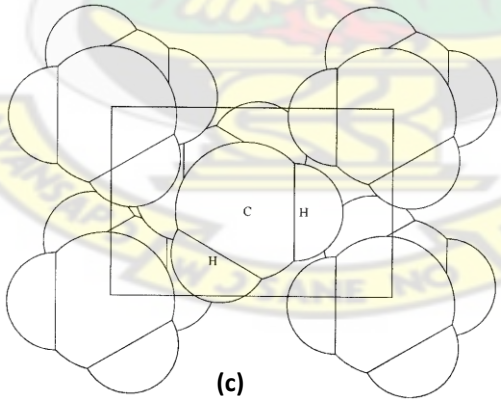

Figure 2.11 continues (c) space-filling representation viewed along the *c* axis (Peacock, 2000).

2.2.2 Monoclinic Unit Cell

The metastable phase of monoclinic crystal form of PEs (sometimes called the triclinic form) are formed under conditions of elongation due to tension or compression as first described by Teare and Holmes **(Teare & Holmes, 1957)**. It has also been identified by **Pollack et al** in **1962** that further crystallization which takes place upon cooling the samples from 131 °C to room temperature give rise to a portion of the second crystalline form (monoclinic) which differs little in volume and enthalpy from the orthorhombic phase. Wide angle x-ray diffraction or magnetic angle NMR spectroscopy is usually used to identify this phase. The monoclinic phase evolves in ^{13}C NMR resonance at 33.6 ppm, 1.4 ppm down field from the orthorhombic resonance at 33.6 ppm, and to three strong reflections between 19° and 26° 2θ (Cu$K_{\propto}$ radiation) that is at 4.56, 3.84 and 3.55 Å compared with 4.13, 3.72 and 2.98 Å for the three strongest of the orthorhombic form. Most of the time, only the reflection at 19.5° is observed, due to the overlap of the other monoclinic reflection with the second orthorhombic phase, when both techniques are used on the same sample. **(Russell et al., 1997)**. The configuration and dimensions of the monoclinic unit cell can be seen in **Figure 2.12**.

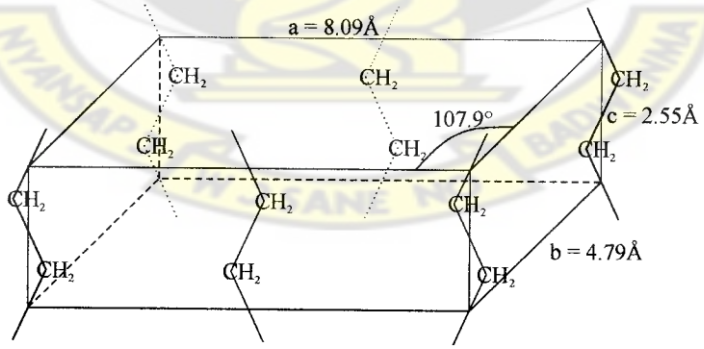

Figure 2.12 Polyethylene monoclinic unit cell (Peacock, 2000).

2.2.3 Hexagonal Unit Cell

The hexagonal crystal form of PE is developed by a laboratory curiosity during crystallization at very high pressures **(Peacock, 2000)**. The hexagonal phase can also be referred to as the " rotator'' phase, because respective chain stems are rotated at random phase with respect to their corresponding neighbours. The hexagonal unit cell's dimensions and configurations can be seen in **Figure 2.13**.

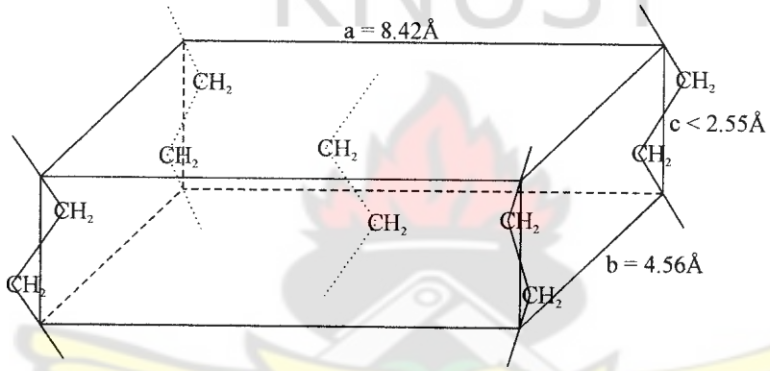

Figure 2.13 Polyethylene hexagonal unit cell (Peacock, 2000).

2.3 Properties of Polyethylene

PPE has outstanding features such as regular chain structure, good mechanical properties, biocompatibility and excellent chemical resistance, very low water absorption together with low vapour permeability. And the ease at which it can processed makes all of its grades an attractive choice for a variety of biomedical and industrial application **(Chrissafis et al., 2009; Sui et al., 2009; Mourad et al., 2009)**. Its low melting point, Young's modulus, environmental stress cracking resistance, yield stress, poor compatibility, creep resistance and environmental stress cracking resistance with several additives restricts its use for certain applications **(Henderson, 1993; Sharif et al., 2008)**.

PE is a wax-like thermoplastic which softens at about 80 – 130 ℃ **(Brydson, 1999)** with molecular repeat structure of – CH_2CH_2 – **(Feldman, 1996)**. Different grades of PE have markedly different thermal and mechanical properties. Available measured density of the grades ranges from 0.91 to 0.97 g/cm^3 **(Carraher Jr, 2013)**. The density of a particular grade is governed by the morphology of the backbone - long linear chain with very few side branches can assume a much more dimensionally compact, regular and crystalline structure. The commercially available grades are: very-low-density PE (VLDPE), low-density PE (LDPE), linear low density PE (LLDPE), high-density PE (HDPE) and ultra-high molecular weight PE (UHWMPE) **(Nwabunma and Thein, 2008)**. **Figure 2.14** gives figurative difference in chain configuration which governs the degree of crystallization which along with molecular weights determine mechanical properties **(Peacock, 2000)**.

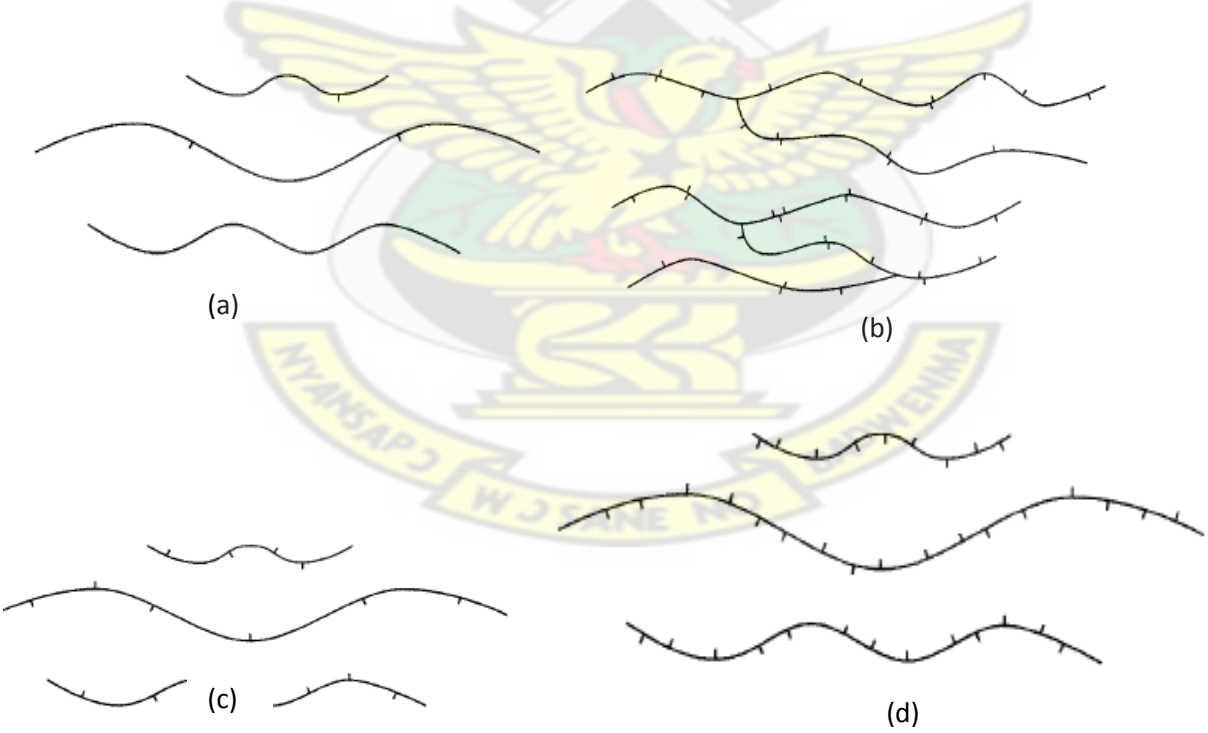

Figure 2.14 Schematic representation of the different grades of polyethylene (a) High-density PE (b) Low-density PE (c) Linear-low-density PE (d) Very-low-density PE (Peacock, 2000).

2.3.1 Physical and Mechanical Properties of Low-Density Polyethylene (LDPE)

LDPE is lightweight and formable PE that has high impact resistance and excellent electrical properties **(Vasile and Pascu, 2005)**. The lower density of LDPE relative to HDPE as in **Table 2.1** is caused by the fact that the molecules of LDPE have many more relatively long branches off the main molecular chain (see **Figure 2.14** (a) and (b)).This prevents the molecules from packing as closely together as they do in HDPE **(Vasile and Pascu, 2005)**. The long-side chain branching LDPE molecules also produces a more amorphous polymer having a lower melting point and a higher clarity. This has the disadvantage of poor properties with regard to tensile strength, stiffness, puncture and the anti-tear resistance and elongation, while retaining the excellent low temperature toughness **(Vasile and Pascu, 2005)**.

2.3.2 Physical and Mechanical Properties of Linear-Low-Density Polyethylene (LLDPE)

This product revolutionized the plastics industry with its enhanced tensile strength for the same density (0.910 to 0.940 g/cm^3) (**Serranti and Bonifazi, 2010**) compared to LDPE (see **Table 2.1**). As the name implies, it is a long linear chain without long side chains or branches. The short chains which are present disrupt the polymer chain uniformity enough to prevent crystal formation and hence prevent the polymer from achieving high densities. Developments of LLDPE over the past decade have enabled production economies compared to LDPE due to its lower polymerization pressures and temperatures. A typical LDPE process requires 35,000 lb/in^2 (241 MPa) which is reduced to 300 lb/in^2 (2.07 MPa) in the case of LLDPE and reaction temperatures as low as 100°C rather than 200 or 300°C are used. LLDPE is produced with

ethylene and side branches of α-olifins such as; 1-butene and most commonly, with 1-hexene or 1-octene comonomer **(Vasile and Pascu, 2005; Ravve, 2012)**.

2.3.3 Physical and Mechanical Properties of Very-Low-Density Polyethylene (VLDPE)

VLDPE is very similar to LLDPE and is principally used in film applications **(Peacock, 2000)**' **(Appendini and Hotchkiss, 2002)**. VLDPE grades vary in density from 0.880 to 0.912 g/cm^3 (**Feldman, 1996**). Its properties are marked by high elongation, good environmental stress cracking resistance, excellent low-temperature properties and it competes most frequently as an alternative to plasticised poly vinyl chloride (PVC) or ethylene vinyl acetate (EVA) **(Peacock, 2000)** (see **Table 2.1** and compare properties) . The inherent flexibility in the backbone of VLDPE circumvents plasticizer stability problems which can plague PVC, and it avoids odor and stability problems which are often associated with moulding EVAs. Lusting et al **(Lustig et al., 1989)** conducted research on heat–shrinkage films for packaging frozen foods, and concluded that the biaxial stretched monolayer film made from VLDPE has physical properties which are more highly desirable for use as heat–shrinkage bags than those from EVA resins **(Lustig et al., 1989)**.

Table 2.1: Comparison of Principal Properties Polyethylene (Peacock, 2000)

Property	HDPE	LDPE	LLDPE	VLDPE	EVA
Density (g/cm^3)	0.94-0.97	0.91-0.94	0.90-0.94	0.86-0.90	0.92-0.94
Degree of crystallinity (% from density)	62-82	42-62	34-62	4-34	-
Degree of crystallinity (% from calorimetry)	55-77	30-54	22-55	0-22	10-50
Flexural modulus (psi @ 73^oF)	145,000-225000	35,000-48,000	40,000-160000	<40,000	10,000-40,000
Tensile modulus (psi)	155,000-200000	25,000-50,000	38,000-130000	<38,000	7,000-29,000
Tensile yield stress (psi)	2,600-4,500	1,300-2,800	1,100-2,800	<1,100	5,000-2,400
Tensile strength at break (psi)	3,200-4,500	1,200-4,500	1,900-6,500	2,500-5,000	2,200-4,000
Tensile elongation at break (%)	10-1,500	100-650	100-950	100-600	200-750
Shore hardness Type D	66-73	44-50	55-70	25-55	27-38
Izod impact strength (ft-lb/in. of notch)	0.4-4.0	No break	0.35- No break	No break	No break
Melting Temperature (^oC)	125-132	98-115	100-125	60-100	103-110
Heat distortion temperature (^oC @ 66 psi)	80-90	40-44	55-80	-	-
Heat of fusion (cal/g)	38-53	21-37	15-43	0-15	7-35
Thermal expansivity (10^{-6} in/in/^oC)	60-110	100-220	70-150	150-270	160-200

2.3.4 Physical and Mechanical Properties of High-Density Polyethylene (HDPE)

The most common method of processing HDPE is blow molding, where resin is turned into bottles (especially for milk and juice), housewares, toys, pails, drums, and automotive gas tanks.

It is also commonly injection-molded into housewares, toys, food containers, garbage pails, milk crates, and cases. The high-density (0.94 - 0.97 g/cm^3) of HDPE is mostly linear and much more crystalline than LLDPE **(Ravve, 2012)**. The density of granules increases by the process of compression moulding due to rearrangement and extra packing of the polymer chains as a result of the imposed pressure. Molecular weight is governed primarily through temperature control, with elevated temperatures resulting in reduced molecular weights. **Khonadkar et al**., (**2003)** studied molecular weight loss of HDPE using thermal gravimetery analysis (TGA) and reported that HDPE does not show any major weight loss up to 450 ˚C, beyond which a sharp weight loss is observed. The catalyst support and chemistry also play an important factor in controlling molecular weight and molecular weight distribution **(Harper, 2002)**. HDPE is ductile and under tension at room temperature usually yields with necking and drawing followed by strain hardening effect and finally ruptures at relatively long elongation **(Khonakdar et al., 2003)**.

2.3.5 Mechanical Properties of Ultra-High Molecular Weight Polyethylene (UHMWPE)

UHMWPE is identical to HDPE, but rather than having a molecular weight of 50,000 g/mol, it typically has a molecular weight of between 3 x 10^6 and 6 x 10^6 g/mol. **Nakamae and Nishino** in **1989** measured "theoretical" elastic modulus, which was determined by observation of strain-dependent X-ray diffraction in the polymer chain direction for various polymers. This theoretical elastic modulus value was associated with the ultimate polymer modulus. The PE grades show tensile moduli far below predictions for their crystalline lattice in the chain direction. Only UHMWPE shows moduli close to the theoretical values **(Kotek, 2008)**. High molecular weight imparts outstanding abrasion resistance, high elastic modulus, even at cryogenic temperatures,

and excellent stress cracking resistance, but does not generally allow the material to be processed conventionally **(Harper, 2002)**. The polymer chains are so entangled due to their considerable length that the conventionally considered melt point doesn't exist practically, as it is too close to the degradation temperature, although an injection-molding grade is marketed by Hoechst. Hence, UHMWPE is often processed as a fine powder that can be ram extruded or compression moulded. Its properties are taken advantage of in uses which include liners for chemical processing equipment, lubrication coatings in railcar applications to protect metal surfaces, recreational equipment such as ski bases, and medical devices. A product has been developed by Honeywell (formally Allied fibre) in 2008 which involves gel spinning UHMWPE into light weight; very strong fibers of stiffness 124 GPa which compete with Kevlar in applications for protective clothing **(Kotek, 2008; Harper, 2002)**.

2. 4 Structure and Mechanical Properties of Starch

Figure 2.15 shows the amylose and the amylopectin structure of starch. The amylose has linear α-D (1, 4') – glucan structure and amylopectin has the same glucan structure but branches at α-1, 6'-linked. Starch possess of more hydroxyl compounds; two secondary hydroxyl groups occurring at C-2 and C-3 positions and one primary hydroxyl group at C-6 when it is not linked. The presence of the hydroxyl compounds in starch makes it hydrophilic and has the potential to react with alcohols. This means that starch undergoes oxidation and reduction reaction resulting in hydrogen bonding and participation in ethers and ester formation. The morphology and the internal arrangements of the chains are affected by water molecules. The glass transition temperature, Tg is also altered and thus changing the mechanical properties and the shape. In processing of thermoplastic starch using injection moulding, the glass transition temperature

normally ranges from 60 to 80°C with weight fraction of water between 0.12 to 0.14. This thermoplastic starch polymer is used to introduce degradation into most of the hydrophobic polymers.

Starch are process from some tubers (potatoes, cassava), cereals and grains (wheat, rice and corn) **(Karim, Norziah and Seow, 2000)**. The source of the starch determines their amylose and amylopectin content. The proportions ranges from about 10–20% amylose to 80–90% amylopectin **(Lu, Xiao and Xu, 2009)**.

Amylose =

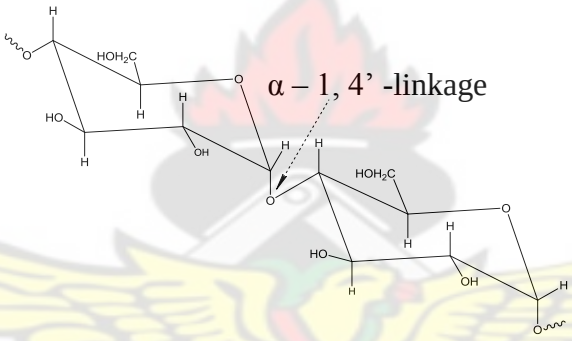

Amylopectin =

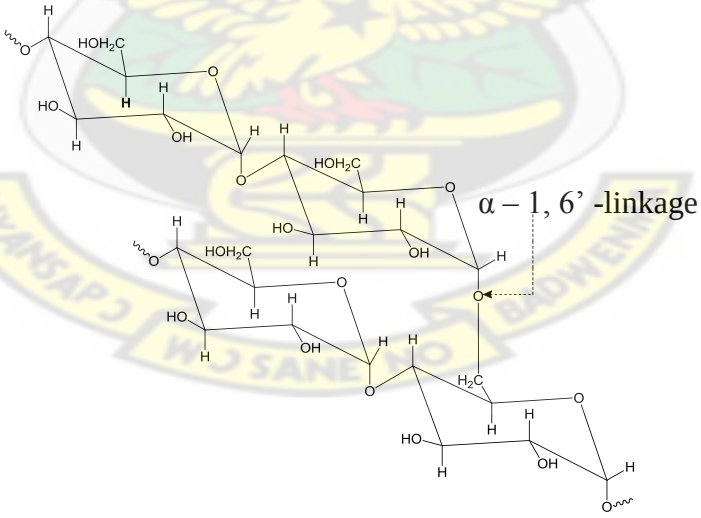

Figure 2.15 Molecular structure of starch (Lu et al., 2009).

Lower retrogradation, lear gel and high viscosity are some rheological and physical properties of starch. These properties are needed in production of some peculiar products. Roots

and tubers starch possess these properties as compared to the cereals and grain starch but the cereals and grains for example corn starch are commercially used than the root and tubers **(Bertolini Andréa, 2010)**. The reason is basically of availability. Amylose and amylopectin ratio determines the physical properties of starch **(Fredriksson et al., 1998)**. The influence of amylose and amylopectin ratio on properties of extruded starch plastic sheets has been studied by **Van Soest.** (**1996)** and he concluded on high values of stiffness and strength of the sheets with high amylose content than the sheets with high amylopectin content. The reason is attributed to the soluble nature of amylose in water and thus forming a helical structure.

The crystalline part of the semi-crystalline starch is the amylopectin region whiles the amorphous part is the amylose section. Starch crystallinity is between 20-45% where amylopectin lamellae are made up of double helices and alien in a thin domain. **Figure 2.16** shows different forms of starch crystal patterns characterized using x-ray diffraction. V-, A-, B- or C-type are formed due to the source of starch, degree branching, molecular mass, amylose and amylopectin ratio and branching length affects starch crystal structure **(Van Soest and Vliegenthart, 1997)**. Co-crystallization could also arise from amylose producing different crystalline lamellae with single-helical structure. This forms complexes with fatty acids or lipid with different packing density and water content.

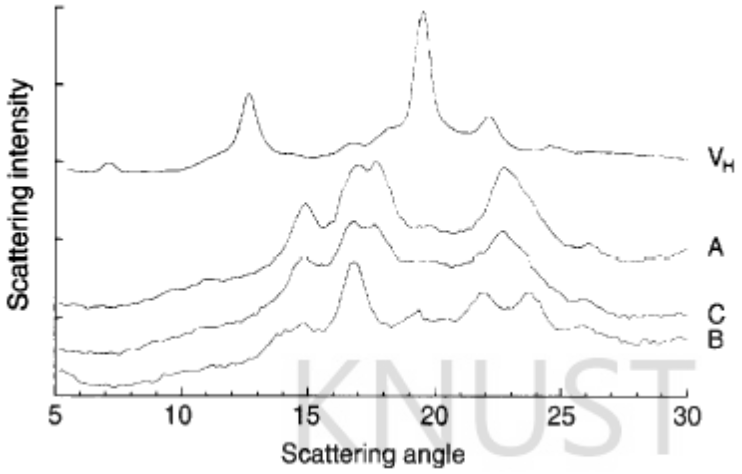

Figure 2.16 X-ray diffraction pattern of maize, potato and pea starch, crystallized amylose. The peak positions are characteristics of A-, B- or C-, VH-type crystallinity, respectively (Van Soest & Vliegenthart, 1997).

The mechanical properties of starch reduces once there is not a good cohesion between the amylose which is the amorphous phase and the amylopectin crystalline phase. This is prevented when there is a total disruption of the starch granular. The residual crystallinity in the residual granules will be avoided and pave way for the creation of amylose network resulting in a high strength and stiffness material. Physical crosslinking by hydrogen bonding will be effective with better entanglement. The elongation and flexibility increase since amylopectin has high molecular mass and high branching structures **(Van Soest and Vliegenthart, 1997)**.

2. 5 Structure and Mechanical Properties of Hydroxyapatite

The inorganic portion of the bone is very much alike to hydroxyapatite. It promotes the growth of cells and also saves as an interfacing material between the bone and an implant during orthopaedic, dental and maxillofacial applications **(Gergely et al., 2009)**. **Figure 2.17 (a)** shows

the hexagonal rhombic structure of the apatite mineral [Ca_{10} $(PO_4)_6(OH)_2$]. The unit cell dimensions are, a = 9.432 Å and c = 6.881 Å. **Figure 2.17** (b) shows the basal plane visualized down c-axis. There is an association of 6 Ca^+ with OH^- in the unit cell permitting a strong binding. The OH^- are occupying the corners plane and they are at equal distance of 3.44 Å onward the columns perpendicular and parallel to the basal plane and the c-axis, respectively **(Bronzino, 2000)**. Hydroxyapatite has a Ca/ P ratio of 10/6 and density of 3.219 g/cm^3. The OH^- groups is usually replaced with Cl^-, CO_3^{2-} and F^- for high chemical stability, as in the case of F^- which is symmetric in shape as compared to OH^- with asymmetric shape. The high chemical stability is what makes fluorine in drinking water resist dental caries **(Bronzino, 2000)**.

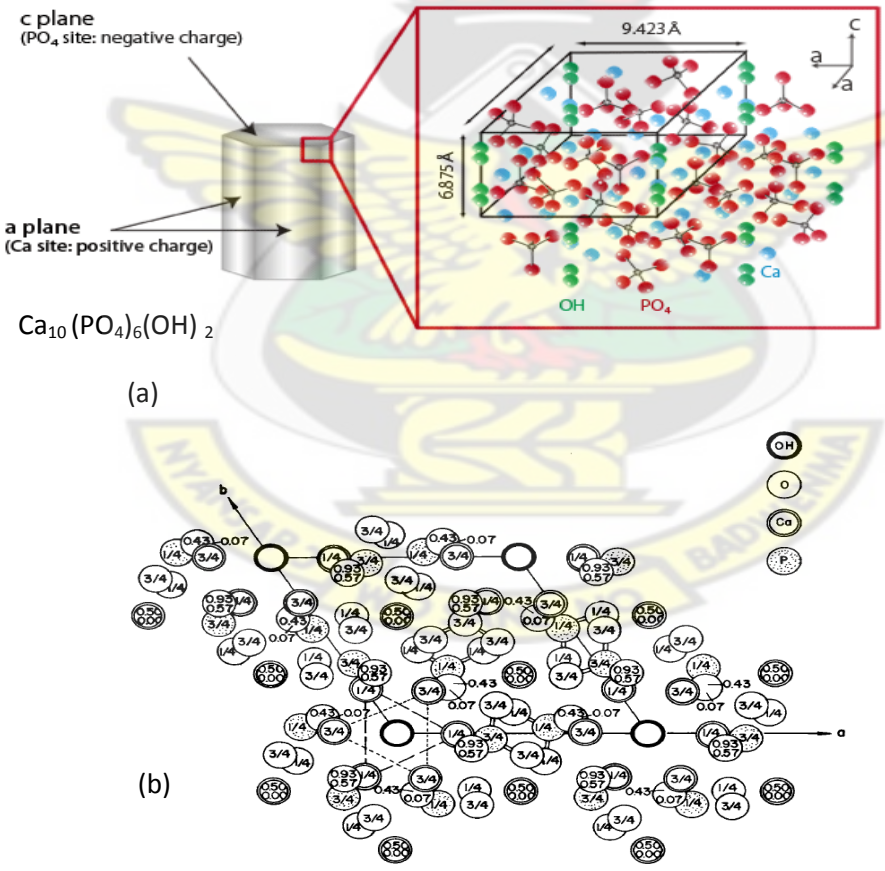

Figure 2.17 Structure of hydroxyapatite (a) hexagonal rhombic prism (b) projected down the c-axis on to the basal plane (Bronzino, 2000).

The bioactive action of hydroxyapatite are affected by dislocations and their density. The bone apposition on bioactive materials could be altered by dislocations. Crystal growth of biological apatites in *in vivo* during dissolution is influenced by dislocations **(Zamiri and De, 2011)** during plastic deformation through slip. Anisotropic plastic deformation of hydroxyapatite crystal at high temperatures has been observed using microscale compression tests along different crystallographic directions. **(Nakano et al., 2001)**. This is because hydroxyapatite crystal deform through crystallographic slip with {1010} <0001> type slip systems. The hydroxyapatite single crystal is brittle and this develops cracks because of micro indentation. But deformations along the [0001] and [1010] crystallographic directions exhibit anisotropic deformation behavior due to nano indentation of hydroxyapatite single crystal. The hydroxyapatite single crystal shows high ductility and fracture toughness along the [1010] crystallographic direction with a lower hardness and yield stress. This confirms that the hydroxyapatite crystal's mechanical properties depends on the crystal size. This implies that the mechanical properties are not sensitive to defects at nanoscale **(Zamiri and De, 2011)**.

2.6 Polymer Blends

Polymer melts and blends rheological properties have been reviewed **(Sadiku-Aboola et al., 2011)**. These properties have brought a lot of developments in the polymer industry and the polymer industry expanding at very fast rates, because the polymer morphology and structure are affected by the melts flow and thus produced advanced high performance materials. There is phase behaviour during melts and that brings the morphological evolutions. The knowledge on how to control the phase behaviour also results in the development of products of high quality.

The phase behaviour could produce blends that are homogeneous or heterogeneous. Homogeneous phase means the individual polymers are miscible, the melts produced a single phase and heterogeneous phase means that the individual polymer are immiscible, the melts produce multiphase blends. Mixture of homopolymers, copolymers, and terpolymers is what constitute polymer blends. Crystalline polymers and amorphous polymers could also be blended and this is influenced by the thermodynamics of the melts.

The aim of blending polymers is to produce specific materials for specific application. This method reduces the cost of production of a new polymeric material. The cost involved in conducting advance research to develop new polymer monomers for industrial use is reduced if the current polymers could be combined into new materials of suitable properties. It combines the superior properties of the two polymers and hence enhanced the performance of the product. This is because new advanced polymer structures could be evolved and such structures can not be achieved by the design polymer monomer composition. The world has seen vast materials ever since polymer blending is envisaged because multi-phase polymers satisfy various demands in commercial market once the phase adhesion is controlled. **(Imre and Pukánszky, 2013).** The polymer blending technique response quickly to meet the world speedily demand of materials for the industries than the design of a new polymer monomer. Designing a new polymer monomer for industrial use takes a lot of time in research and development. The issue with the polymer blends is that once the multi-phase polymer interface bonding and the morphology are not controlled the material suddenly fails **(Sadiku-Agboola et al., 2011)**.

Morphology rules multi-phase polymer physical properties like toughness, weather resistance, transparency and flowability. This outcome has led a lot of material scientist to exploit various physical and chemical techniques to control the morphology of these multi-phase

blends. Multi-phase polymer morphology has been modified using reactive polymers. It reduces the surface tension and creates a better interaction between the polymer phases thus altering the morphology. A lot of present industries uses reactive polymers for multi-phase polymer morphological modification. The method of using reactive polymers for morphological evolutions is termed as reactive compatibilization **(Imre and Pukánszky, 2013; Araki et al., 1998)**. **Gleiter** (**2000)** described how nanostructured morphology occurs in polymer blends. According to his paper spatially homogeneous solid solutions formation do not exist in polymer blends. They are separated on length scales starting from a few nanometers to several micrometers. Nanostructure morphologies forms in blends composed of one crystalline component and one amorphous components include: (i) the spherulites of the crystalline component grow in a matrix made up of mainly the amorphous polymer (ii) The interlamellar regions of the spherulites of the crystalline polymer could be fused with the amorphous component. (iii) domains of dimensions larger than the interlamellar spacing are formed when the spherulites of the crystalline polymer is fused with the amorphous component. Four common morphologies are formed with the blends of two crystalline components are: (i) amorphous matrix shows a dispersion of the two crystalline components. (ii) Stacked crystals are formed in a simple mode whiles the other one component crystallizes in a spherulitic morphology. (iii) spherulitic structure exist separately in both components. (iv) mixed spherulites made of lamellae of both polymers are formed at the same time.

There is very large class of polymeric materials since polymerization produces several polymer chains. This paves way for several combination of polymers to produce blends. Different blends could be formed for academic and industrial purposes. Phase behaviour is the main parameter that differentiates them. Miscibility against phase-separation is what one

produces. The blend property profile; mechanical properties, intermediate between the unblended constituents and determines whether a blend is miscible or phase-separated. **Table 2.2** shows a list of various polymer blend. Engineering polymer blends, eastomer blends, engineering polymer blends, impact modified polymer blends are some examples of polymer alloy compositions.

Table 2.2: Classes of polymer blends

1.	Impact modified polymer blends
2.	Engineering polymer blends
3.	Crystalline-crystalline polymer blends
4.	Emulsion blends
5.	Crystalline-amorphous polymer blends
6.	Thermosetting polymer blends
7.	Impact modified polymer blends
8.	Molecular composites
9.	Reactive compatibilized blends
10.	Liquid-crystalline polymer blends
11.	Elastomers blends
12.	Interpenetrating polymer networks
13.	Polyelectrolyte complexes
14.	Recycled polymer
15.	Water soluble polymer blends
16.	Core-shell polymer system
17.	Polymer blend composites
18.	Black copolymer-homopolymers blends
19.	Polyolefin blends
20.	Biodegradable polymer blends

2. 6.1 Miscible Polymer Blends

Polymer combination produces miscible polymer blends and its behaviour is same as systems with single phase. They are less expensive, convenient way of studying and perfecting of polymer combinations. Combination of individual pure components determine their properties. Molecular weight, chemical structure, composition and intermolecular interactions are the factors that affect their properties. Even though miscible blend polymers are of great practical and scientific interest, it cannot come to the conclusion that miscibility always favours the achievement of the right properties.

2. 6. 2 Immiscible Polymer Blends

Several phase morphologies are evolved when blending immiscible polymers in the liquid state. This is because of the flow history, blend ratio and the nature of the components. Different flow fields influenced immiscible polymers to behave same as different materials, the rheological factors affect phase morphology. Immiscible polymers are mostly binary polymers. To a great extent, their behaviour are determined by the state of the interface existing between their components. The interface interaction between the melts components is basically denoted by a quantity k, which is the interfacial tension. This is excess free energy emerging from unstable molecular forces of the melt components. Mostly immicible polymers blends have poor interfacial adhesion and thus producing low mechanical properties. This requires interface manipulations to raise the property integrity. The classical way to improve on the adhesion of the blend is by the application of a compatibilizer. Interfacial tension is reduced because it is

miscible in both components. **Elias et al. (2007)** have used rigid silica nanoparticles as a compatibilizer.

2. 6. 3 Compatibilization

Immiscible polymer blends interface could be modified by compatibilization. The interfacial tension is reduced permitting adequate interactions between the blend phases. Compatibilization also stabilises the morphology of the blends, forming polymer alloys. Physical techniques like retardation, quenching, co-crystallization and cross-linking are used to disperse compatiblising molecules. Chemical compatibilization is also another means of modifying the blends interface but here the morphology of the blends greatly depends on the compatiblizer but not on the extent of mechanical pressure.

2.7 Biodegradable Polymers

Biopolymers have been revamped through polymer blending. Tailor - made biopolymers are easily fabricated using blending techniques. This advent has resulted in production of biopolymers with controlled degradation giving vast interest. A lot of journals have reported on their diverse applications. Biopolymers are polymers that are disintegrated through chain secession with the aid of microorganisms or enzymes. They can be produced as bio-based or biodegradable and in most applications both types are combined **(Imre and Pukánszky, 2013)**. Modern plastics industry has now advanced in producing biopolymers with renewable polymers rather than fossil feedstocks. The renewable polymers are usually obtained from nature and are classified as natural polymers. They mostly occur as macromolecules such as starch, silk,

cellulose, lignin and hemicelluloses. Renewable resources monomers gives other classes of polymers consisting of natural-based and bio-based synthetic polymers. Some of the polymers in this classification are Poly(lactic acid) (PLA), polyethylene (PE), poly(ethylene terephtalate) (PET) and polyamide (PA). PE and PA are bio-based traditional polymers. Bacterial polyesters is produced by bacterial fermentation in the industry and is regarded as both natural and natural-based polymer **(Imre and Pukánszky, 2013)**.

Another form of biopolymer classification is based on the source and the synthesis of the polymer. There are four classes of this type: (a) Agro-polymers obtained from agro-resources which constituted polymer biomass. Examples of polymers in this category are polysaccharides which are extracted from cassava, maize, potatoes and wheat. Straws, wood, gums, pectins, chitin/chitosan form ligno-cellulosic products. Casein, gelatin/collagen, whey from animals and plant's zein, soya and gluten forms protein and lipids (b) the next category is polymers from microbial activities. Poly(hydroxybutyrate) (PHB) and poly(hydroxybutyrate cohydroxyvalerate) (PHBv) are hydroxyalkanoates (PHA) polymers produced (c) chemically synthesized polymers from monomers derived from agro-resources forms the third category. Example is PLA (d) Polymers derived from fossil resources through chemical synthesis. Examples are polyesteramides (PEA), polycaprolactones (PCL), aromatic co-polyesters (e.g., PBAT) and aliphatic co-polyesters (e.g., PBSA) **(Vieira et al., 2011)**.

All polymers degrade to some degree as time progresses due to environmental influence. For this reason, polymer degradation should be well defined to describe this characteristic. The environmental influence can decrease the molecular weight of polymers through chain scission of the polymer backbone and with time the degradation comes to completion. This could be a preferred definition for degradable polymers but in biodegradable polymers to the contrary,

human, animal, fungi and other cell activities evoked the chain scission. This is an enzymatic action which is also initiated by physicochemical phenomena. Biodegradation occurs in two ways. Fragmentation of the polymers into lower molecular masses is the first to occur. Here oligomers breakdown into final monomers by either abiotic or biotic reactions. Abiotic reaction is through hydrolysis, photodegradation oxidation whilst biotic means are through microorganisms. Bioassimilation of the fragmented polymer is the second step and this is caused by micro-organism's mineralization **(Vroman & Tighzert, 2009)** (see **Figure 2.18**). The degradation process erodes the polymer surface or the bulk polymer. Mostly polymers of high hydrophobicity or small pore size undergo surface erosion. It becomes difficult for large amount of water to penetrate the polymer and as such decreasing the external dimensions.

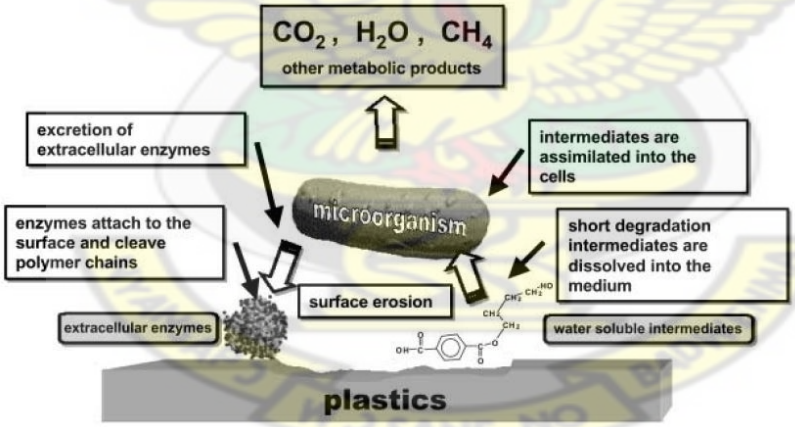

Figure 2.18 General mechanism of plastic biodegradation (Müller, 2005).

2.7.1 Starch Enhancement of Polyethylene Biodegradation

Starch is a highly hydrophilic macromolecule. The dry native starch is directly mixed with polyethylene as a biodegradable additive in the preparation of biodegradable polyethylene films **(Leja and Lewandowicz, 2010)**. The microbial breakdown of polyethylene is actually not possible because of its high molecular weight. Biodegradation has a link with molecular weight of polymers. The high molecular weight polymers degrade at a faster rate than the low molecular weight polymers. One of the easy ways to initiate biodegradation of the higher molecular weight polymers is to create a medium for more oxygen passage for microorganisms to consume. Starch is found to permit this role in PE **(Rutkowska et al., 2002)**. Microorganisms assimilate these abiotic intermediates in the PE, thus complicating the degradation products found in the environment. The amount of oxygen in the environment determines how many microbes that will populate the sample. Moisture content and environmental temperature is also sensitive to degradation **(Ramis et al., 2004)**. Biodegradation of polyethylene is expected to be similar to that of paraffins, and it has been well documented. The alkane chains oxides to a carboxylic acid and latter subjected to β-oxidation. Fatty acids and paraffin's in man and animals also undergoes similar β-oxidation **(Arkatkar et al., 2009)**. Carbonyl groups are formed due to the oxidation of the polymer chains. This first abiotic step follows by microbial assimilation which decreases the carbonyl groups. Two carbon fragments, acetyl-CoA are removed as a result of the carboxylic acids produced reacting with coenzyme A (CoA). The final degradation products produce carbon dioxide and water as the carbon fragments metabolize in citric acid cycle **(Gilan, Hadar, and Sivan, 2004)**. PE/cellulose blend of 5% to 15% of cellulose did not give any meaningful increase in biodegradation but when the cellulose content is raised to 30% the blends started to degrade after 14 weeks under composting environment **(Arkatkar et al., 2009).** PE/starch blends

biodegradation is achieved by high starch loading but this produced blends with inferior mechanical properties, mostly with elongation at break **(Sailaja and Chanda, 2001)**. The tensile strength of thermally pretreated (for 10 days at 70 °C) polyethylene containing 6% starch by 60% while *Streptomyces species* reduced the percentage elongation of the same blend from 46.5% to 28.5% **(Arkatkar et al., 2009)**. Addition of poly (ethylene-co-acrylic acid) as a compatibilizer has improved the mechanical properties of the blend. The processability of the LDPE and LLDPE blend with starch has been improved by the treatment of starch with glycerol and thus reduced degradation of starch but at higher loadings of plasticized starch the blends show poor mechanical properties. The mechanical properties of PE has been improved by the introduction of maleic anhydride-grafted copolymers compatiblizer.

2.7.2 Biodegradable Polymer Materials and Implants

Väänänen, P **(Väänänen, 2009)** reviewed in his PhD thesis, the biodegradation of polymer materials and implants. According to his thesis polyglycolide acid (PGA) was the first biodegradable material used for orthopaedic fixation since it has enough strength retention for fractures. PGA is a hydrophilic polymer that degrades too fast. The degradation comes to completion within 6-12 months with the absorption time starting from the fourth week. The rapid degradation of the material causes a high amount of released degradation debris from the implant. **(Vasenius et al., 1990)**. Adverse tissue reactions are evoked when the amount of debris released is more than the clearance capacity of the surrounding tissues. Hence for lager volume application such as orthopaedic implants PGA is not recommended.

Polylactic acid (PLA) based poly (L-lactic acid) (PLLA) has become the preferred widely used polymer for orthopaedic implant fixations since it has much slower degradation rate than

PGA. **Kontakis et al. (2007)** did a review article and reported that PLLA is proven to be nontoxic and gradually degraded, and the use of PLLA plates and screws to fix mandibular fractures in dogs has been presented by **Kulkarni et al** in **1971**. During the same year 1971 another study also published the results of PLLA sutures in mandibular fractures, reporting no serious tissue reactions. Notwithstanding, PLLA implants takes as long as ten years to totally degrade, the complete absorption time is > 5 years **(Waris et al., 2004)**.

Co-polymerization of PGA and PLLA has been utilized to curb the slow degradation of PLLA and the fast degradation of PGA. A number of innovations in material science, such as the self-reinforcement technique is presented by Tormala et al **(Tormala et al., 1988)**. The introduction of co-polymers has led to implants with better biodegradation and mechanical properties. Copolymerization combines more than one type of polymer, L-lactic acid and PGA (PLGA), L-lactic acid and D-lactic acid (PLDLA) are examples of copolymers. The copolymer introduced disrupts the lamellar chains of the L-lactic acid causing more amorphous phase to be evolved. The polymer crystallinity then decreases thus permitting a faster completion of degradation by hydrolysis. **Väänänen (2009)** reported in his PhD literature review that, the copolymerization reduced the degradation time of PLLA to 2-4 years. This novel improvement is adequate for biomedical implant applications. Blending PLA with some materials component to control degradation and mechanical properties to suit an application has also been explioted. Trimethylene carbonate (TMC) for example is used for rubber toughening. Currently commercial approved clinical biodegradable implant fixations such as rods, pins, plates and screws are mostly PLA based **(Väänänen, 2009)**.

These fixation devices serve no purpose after they have guided the hard tissue to remodel. This is a paramount concern that needs to be considered when designing biodegradable implants.

The need for second surgery for fixation device removal is eliminated. Additional importance to the use of biodegradable fixation devices is that the likely risks associated with metallic implants; imaging or radiotherapy interference, stress-protection weakening of the bone and corrosion, will be averted. However, besides all these advantages of the use of biodegradable devices there is still an issue of biocompatibility of the materials selected for fabricating these devices. The type of materials resorted to has great influence on the biocompatibility. For large-scale clinical implementation, an adequate biocompatibility and tolerable mechanical strength retention properties is a *sine qua non* **(Böstman and Pihlajamäki, 2000)**. **Table 2.3** shows a list of the mechanical properties of clinical implant materials. The biodegradable implant materials showed far less values as compared to the metallic implant materials; stainless steel (SS) or titanium (Ti). This is in line with the fact that the mechanical properties of implants made out of degradable materials are mostly weaker than the traditional metallic fixation devices **(Väänänen, 2009)**. Moreover, biodegradable implants change over their mechanical properties with time period during bone remodeling as compared to the metallic implants. It is therefore insufficient to compare only the initial property value of the biodegradable implants materials to that of metallic implant materials. Manufacturing processes such as possible self-reinforcing, processing temperature and sterilization methods also influenced the mechanical properties of both types of implants **(Väänänen, 2009)**. This provides a possibility of producing implants with unique required properties. This means processing a material with a different manufacturing technique can produce a product with specific properties **(Väänänen, 2009).** Therefore unambiguous conclusion about comparing the properties of biodegradable implant materials with other products made out of the same raw material is detrimental if the precise processing methods and conditions are not provided.

Table 2.3: Material properties of some clinically used implants and cortical bone (Väänänen, 2009)

Material	T_g (°C)	T_m (°C)	Modulus (GPa)	Strength (MPa)	Elongation (%)	*In vivo* loss times	
						Strength (weeks)	Mass (months)
PGA	35-40	225-230	4.0-7.0	75-142	15-20	3-6	6-12
PLLA	56-65	170-178	2.7-5.1	40-140	5-10	12-26	> 24 (up to 10 years)
PLDLA	55-60	Amorphous	1.9	42-51	3-10	12-16	12-36
SS (316L)	–	1375-1400	200	550-965	20-50	–	–
Ti	–	1650-1700	100	620	18	–	–
Cortical bone	–	–	3.3-17.0	51-193	1	–	–

2.8 Method of Assessment for Biodegradability of Biopolymers

A reproducible and controlled biodegradation test involves the use of systems where only extracellular enzymes known to depolymerize a particular group of polymers are used **(Müller, 2005)**. In the clinical situation, aging media are usually used for i*n vitro* degradation tests to determine the functional behaviour of polymers. There is usually several results observed when *in vivo* and *in vitro* tests are conducted on the same material, considering the complexity of the body fluids **(Azevedo and Reis, 2005)**. For example, linear copolymerization involving lactide and ethylphosphate and poly(lactide-co-glycolide) degradation rates are comparatively faster *in-vivo* with respect to *in-vitro* **(Chaubal et al., 2003; Tracy et al., 1999)**.

Phosphate buffer solution (PBS) is mostly used for incubating materials for degradation studies. Consequently, the only observable degradation is normal hydrolysis is expected. According to **Hooper et al. (1998)**, the appropriate incubation buffers for an accurate *in-vivo* degradation simulation of tyrosine-derived polymers is simulated body fluid (SBF) and PBS. Some non-buffered solutions such as isotonic saline solution and water have also been used in several degradation studies, but the body fluids' buffer capacity of the above test had been

ignored. Again, a lot of the degradation tests do not consider the replacement of the degradation buffers **(Azevedo and Reis, 2005)**.

One other factor of importance is the mass: volume ratio. Different mass-volume ratios have different effects on the degradation kinetics of the biomaterial. In order to make an appropriate choice of the incubation media, mass: volume ratio, the degradation test should factor in, the time the material will be in contact with the tissues of the body, and the locale where the material would be implanted. For example, inaccessibility to enough quantities of body fluids, could destroy the capacity of the body fluids to ensure local buffering and cause undesired effects to the surrounding tissue, when release of acidic degradation by-products in anatomical regions. However, insight into some aspects of the degradation process of certain biomaterials can be predicted due to the possible presence of enzymes and other reactive species in the *in vivo* environment, when degradation solution such as water, serum, enzyme buffer, ionic and simulated body fluids are used **(Azevedo and Reis, 2005)**.

The application of static or vibrational conditions during the degradation tests is subject of controversy. The level of agitation may cause the biomaterial kinetics of degradation to change, this could speed up the release of degradation products from the surface or bulk of the material into the solution. Agitation enhances the interaction between the insoluble substrate (biomaterials) and soluble free enzyme, increasing adsorption in the case of enzyme-mediated degradation. Since body fluids move slowly in both soft and hard tissues it is highly recommended to perform degradation tests under slow agitation (two rotations per minutes) or static conditions to imitate the physiological conditions. However, the use of other agitation conditions during *ex vivo* growth of tissues has been well documented **(Azevedo and Reis, 2005)**.

It is recommended to use approved guided methods for characterizing the degradation properties of biomaterials since the diverse nature of conditions of the various degradation studies does not make room for direct comparison. ISO standards provides guidelines and general requirement to test and assess the degradation of biomaterials. This is appropriate way of identifying and quantifying degradation products of polymers. Due to the varied applications of biomaterials, the standards recommend that testing should be carried out in an environment that closely mimics the environment under which it is going to be used, and the conditions should reflect the purposed function **(Azevedo and Reis, 2005).**

Degradation alters polymer properties which can be monitored by using many analytical techniques. In the initial stages of degradation, the most significant activity is the gradual diffusion of water into the polymer matrix (increase in water uptake), with little changes in the sample mass, the molecular weight and polymer tensile strength. The significant changes are increased in surface roughening and surface free energy and in the long run, the chemical changes due to hydrolysis. The next stage of degradation process involves a decrease in the polymer molecular weight, which results from scissioning of the chains and diffusion of larger molecular weight fragments into the solution. Consequently, there is an increase in weight loss and porosity of the polymer matrix as well as a decrease in tensile strength. The collapse of the polymer matrix and a significant decrease in molecular weight characterizes the stages of advanced polymer degradation. All of these results in decrease in mechanical properties because there is loss of crystallinity in the polymer matrix. Various methods used for monitoring degradation and analyzing degradation products are summarized in **Figure 2.19**. The main techniques can be put into two; bulk analysis and surface analysis. Bulk analysis determines weight loss, molecular weight, mechanical properties and temperature transitions suitable in

monitoring the later stages of degradation whiles surface analysis uses infrared and UV spectroscopy, contact angle measurements and x-ray photoelectron spectroscopy to monitor the first stage changes occurring during degradation. Therefore an appropriate way to select a technique is based on the degradation stage as well as the properties of the biomaterials under study.

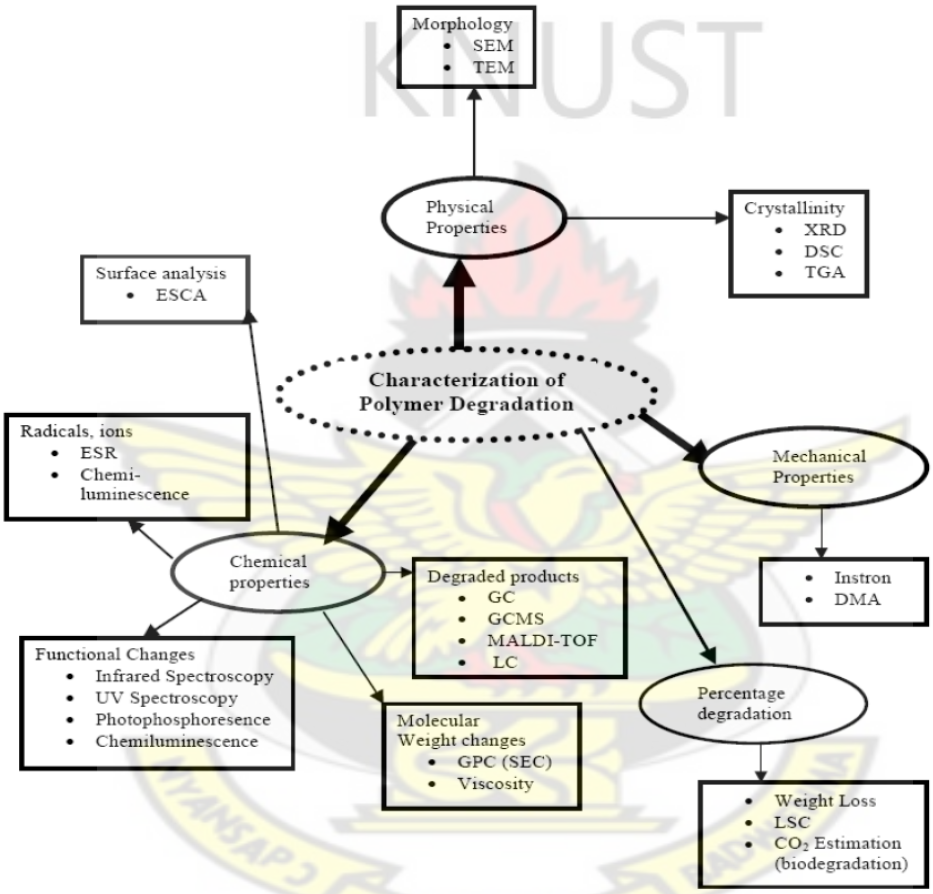

Figure 2.19 Degradation analytical techniques (Pandey et al., 2005).

2.9 Water Absorption

The mechanical properties, dimensional stability and degradation of polymeric implants are affected by water uptake. The functional properties and biocompatibility are compromised due to

defects caused by water infiltration. Water exposure and uptake may decrease the life-span of an implant due to hydrolysis and microcrack formation **(Correlo et al., 2005)**. The absorption of polymeric materials includes the effect of the; amount of absorbed moisture/water, water temperature, time of immersion and interaction of all these parameters **(Papanicolaou, Kosmidou and Vatalis, 2006)**. This reduction in mechanical performance must be accommodated for during product design in order to ensure long term structure survival. In order to determine the long-term moisture effects on composite components, representative parts are commonly tested after having been exposed to designed moisture conditioning environment **(Rolla, 2012)**.

In practical situation, the percentage of water/moisture absorbed in the implants is calculated by mass difference between the samples immersed in water and the dry samples using the equation:

$$\Delta M(t) = \frac{m_w - m_d}{m_d} \times 100\%\,, \tag{2.17}$$

where $\Delta M(t)$ is the water uptake by the material, m_w, m_d are the mass of the specimen before and after immersion in water, respectively.

The diffusion coefficient of a material determines how much water is been taken by the material. Water-soluble additives and growth factors that aid in tissue repair are supplied due to water penetrating rapidly into the polymer matrixed **(Correlo et al., 2005)**. It is assumed that the process follows Fick's second law of diffusion. For an axisymmetric diffusion, three-dimensional (3D) Fick's equation is given by

$$\frac{\partial M}{\partial t} = D\left(\frac{\partial^2 M}{\partial x^2} + \frac{\partial^2 M}{\partial y^2} + \frac{\partial^2 M}{\partial z^2}\right), \quad (2.18)$$

where ***M*** is the instantaneous moisture content at a specified time, **t** along the x-axis and **D** is the diffusion coefficient. For one-dimensional Fickian diffusion:

$$\frac{\partial M}{\partial t} = D_x\left(\frac{\partial^2 M}{\partial x^2}\right) \quad (2.19)$$

The moisture distribution and the weight of moisture inside the material is initially zero and the polymer is placed in an infinite bath of the solvent, the solution to equation (2.9) is given by Crank **(Crank, 1975)**

$$MR = \frac{M-M_i}{M_e-M_i} = 1 - \left(\frac{8}{\pi^2}\right)\sum_{m=0}^{\infty}\frac{1}{(2m+1)^2} exp\left(-\frac{\pi^2(2m+1)^2}{L^2}Dt\right), \quad (2.20)$$

MR is moisture ratio; M_i and M_e are the initial and equilibrium moisture content in the material, respectively.

Adherence to Fickian behaviour is determined by testing the conformity to the initial kinetics to $\sqrt{t}$ scaling. At small times, when MR is small (<0.60), Equation (2.20) can be approximated to

$$MR = \frac{4}{L}\sqrt{\frac{D_x t}{\pi}}, \quad (2.21)$$

A plot of **MR** against $\sqrt{t}$ yields a straight line in the initial stages but reaches asymptotically maximum moisture content. When a solvent infiltrates a polymer, insufficient movement of the polymer chains totally does not homogenized the infiltration environment. Hydrophobic and hydrophilic polymers both undergo such a diffusion with different diffusional mobility.

The diffusion coefficient, D is determined from the slope, K of the linear portion of equation (2.21)

$$D_x = \pi \left(\frac{KL}{4}\right)^2, \tag{2.22}$$

Since the time required for analyzing samples in above method takes more days, different models have been developed to describe the moisture absorption of materials. A more advanced microstructural finite-based element model is desirable **(Rolla, 2012)**. This helps to select potential samples from a list of samples, to speed up the experiment and also cut down cost of running an experiment. Pore-scale flow which is a pore-network model based on the Stoke's, Darcy or Brinkman equation is capable of stimulating multi-component reactive and adsorptive transport under saturated and variably saturated flow conditions. At the fundamental microscale the Stoke's equations apply and provide a complete description of the entire flow field. However, as a result of the complex and often only statistically known geometry of the solid surfaces in the medium, solution of the Stoke's equations is generally very difficult. On the macroscopic level, Darcy's law, first established empirically but more recently derived formally by performing appropriate volume averages of the Stoke's equations, is applicable. The qualitative difference between these two descriptions of the flow motivated Brinkman to suggest a general equation that interpolates between the Stoke's equation and Darcy's laws **(Durlofsky and Brady, 1987)**. The Brinkman equation is given by:

$$\mu\nabla^2 u - \nabla p - \mu\alpha^2 u = 0,\ \nabla . u = 0, \tag{2.23}$$

where $\boldsymbol{\mu}$ is the Newtonian fluid viscosity, $\boldsymbol{\alpha}$ is the permeability $\boldsymbol{u}$ and $\boldsymbol{p}$ are the average velocity and pressure, like the Stokes equation but unlike Darcy's law, second order in velocity. This is

significant since it allows for the solution of flow around a particle or flow caused by motion of a particle with no-slip boundary conditions on the surface.

The creeping flow (Stoke's flow) has been used to solve the flow in the crevice of a porous medium **(Keller et al., 2004)**. The model geometry is produced using electron microscope images and pore-scale model with COMSOL Multiphysics 4.0 sheds new light on the movement of large particulates and colloids moving through variable-pore geometries in the subsurface. Numerical model of the Brinkman equation predicting the existence of solution to Brinkmann system governing fluid flow in porous media has also been described and the results have increased credibility when compared to real life situations **(Kobera, 2008)**.

2.9.1 The Residual property module (RPM)

The residual behaviour of materials after deformation has been described using RPM; developed by the Composite Materials Group, University of Patras. This provides a mathematical depiction of how polymers lose mechanical properties (i.e. mechanical degradation) when they absorb water. The model has already been predicting accurately the residual properties of materials independence of the cause of deformation and of the type of material is at consideration. The RPM model gives well predictions of the mechanical properties for deformations caused by water absorption at temperatures below Tg.

The model assumes that the mechanical degradation of a material absorbing water has an exponential decay form:

$$\frac{P_r}{P_o} = 1 - e^{-u} \qquad (2.24)$$

where $\boldsymbol{P_r}$ represents the value of the mechanical property lost at any time of the absorption process, $\boldsymbol{P_o}$ is the original value of the property before the immersion of the specimen, and **u** is a function of the amount of water absorbed by the material at that time. **Equation 2.24** is the same in calculus as

$$\boldsymbol{s = y + \frac{1}{s}\frac{dy}{dx}} \tag{2.25}$$

where $\boldsymbol{y = \frac{P_r}{P_0}}$

and $\boldsymbol{x = \frac{\Delta m}{m_0} = M}$

where **M** is water absorption rate and **m** is the mass. Separating variables and integrating **equation 2.25** gives:

$$\boldsymbol{sx + c = -\ln(s - y)}$$

$\boldsymbol{e^{c-sx} = s - y}$, let $\boldsymbol{k = e^c}$ then

$$\boldsymbol{y = s - ke^{-sx}} \tag{2.26}$$

Initially when a sample has not absorbed water, $\boldsymbol{y(0) = 1}$ then $\boldsymbol{k = s - 1}$, this implies that

$$\boldsymbol{y = s + (1 - s)e^{-sx}} \tag{2.27}$$

The boundary conditions are fulfilled since,

$$\boldsymbol{M \to \infty \Longrightarrow \frac{P_r}{P_0} \to s}$$

and

$$M \to 0 \Longrightarrow \frac{P_r}{P_0} \to 1$$

To apply this model, the three tests that are needed are mechanical test to determine P_∞ and P_0, and one additional test to measure the time variation of the water uptake in the material. Once the time variation of the water uptake, M (t) is known, then the residual property variation versus time of immersion is obtained **(Papanicolaou et al., 2006)**.

Chapter three

Materials and Methods

3.1 Materials

Linear low-density polyethylene, melt flow index of 2.16 g/10 min at 190 °C, provided by SEEKTEC Honam Petrochemical Corp (Seoul, Korea) was used. Cassava starch (*Manihot esculenta crantz*) of 17% amylose content was purchased from the Ghanaian local market. Hydroxyapatite was extracted from cortical bovine bone at Department of Ceramics, KNUST, Kumasi.

3.2 Blend Preparation

The bovine bone was cleaned, soaked in 10% sodium hypochlorite for 24 h, rinsed in water and boiled in 5% sodium hydroxide for 3 h. It was then incubated in 5% sodium hypochlorite for 6 h, washed and soaked in 10% hydrogen peroxide for 24 h. The material was subsequently sintered at $1100\ ℃$, pulverised and then sieved to particle size $\leq 60\ \mu m$ **(Rodrigues et al., 2003)**.

LLDPE/starch/hydroxyapatite blends were obtained by measuring different quantities of LLDPE, starch and hydroxyapatite in a volumetric flask. The measured powders were blended in a Kenwood blender for 4 min. The powders were then transferred into the hopper of a plastic injection moulding machine (designed and manufactured by JB Engineering, Chippenham Ltd) shown in **Figure 3.0**. The experimental moulding temperature was 170 °C and the setting time was 4 min. The samples in **Table 3.0** were prepared. LLDPE and LLDPE / starch (40 wt. %) blend were used as controls.

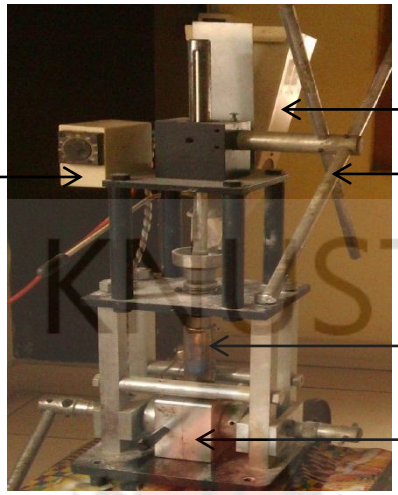

Figure 3.0 Plastic injection moulding machine.

Table 3.0: Composition of samples

SAMPLE CODES	LLDPE (% w/v)	STARCH (% w/v)	HA (% by parts)
SP	100	--	--
SS	60	40	--
SH	60	40	1.0
SI	60	40	1.5
SJ	60	40	2.0
SK	60	40	2.5
SL	60	40	3.0

3.2.1 Specimen Mould Design

Sample moulds were designed in the Mechanical Engineering Laboratory, KNUST based on ASTM D 638 (BS EN ISO 527-1) standard. ASTM D 638 and ISO 527-1 are technically equivalent. This specification is used to determine tensile properties of plastics and plastic composites with thickness up to 14 mm. **Figure 3.1** shows a schematic of the ISO 527-1 specimen type 1B and **Figure 3.2** shows samples formed.

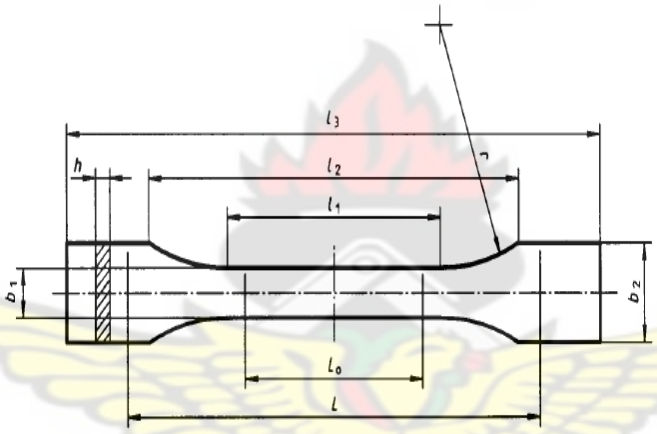

Figure 3.1 Schematic diagram of ISO 527-1 specimen type 1B; l3 - overall length (60 mm), l2 – Distance between broad parallel-sided portion (40 mm), r - radius (5 mm), l1 – length of narrow parallel-sided portion, b1- 5mm and b2 – 15 mm.

Figure 3.2 Picture of some of the samples formed using ISO - 527-1 specimen type 1B. Inscriptions on samples are sample codes.

3.3 Determination of Tensile Properties

Tensile modulus in dry state was measured on the samples in **Figure 3.2** using Titan's tensile testing machine at Ghana Standards Authority, Ghana. Samples were gripped at a distance of 40 mm and pretension load intervals of 2.00 N were applied. The cross head speed was 5 mm / min. five measurements were conducted for each sample. The samples were elongated, measuring the load carried by the sample and the extension. The load-deflection was translated to stress-strain curves and tensile properties (tensile strength, modulus and elongation) were calculated. **Figure 3.3** shows a sample after deformation.

Figure 3. 3 Picture of sample gripped by the jaws of a Titan tensile tester after deformation.

3.4 Characterization Techniques

X-ray diffraction (XRD) and scanning electron microscopy (SEM) were used to characterize samples. Specimens were cut at the middle cross-section using the diamond wheel cutter shown in **Figure 3.4** and the (new) surfaces were used for studies. Specimens were placed on stubs and imaged at magnification of x920 in all cases using a ZEISS EVO-500 SEM operating at an extra

high tension voltage (EHT) of 10.00 KV. The crystallinity and the structure of the specimens were determined using a PANalytical Empyrean X-ray diffractometer, equipped with Cu K_α X-ray radiation. The diffraction patterns were recorded over 2θ angles ranging from 5° to 90° in replicates of five.

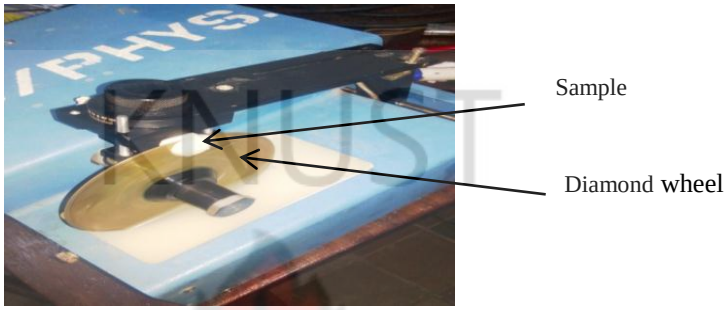

Figure 3.4 Picture of Diamond wheel cutter undergoing cutting of specimen.

The crystallinity of the samples was calculated using HighScore (Plus) 4.0 (powder diffraction analysis software developed by PANalytical). The percentage crystallinity ($\%Xtal$) in a sample is defined by the intensity ratio of the diffraction peaks, $I_{net.}$ and the sum of all measured intensity, $I_{tot.}$

$$\%Xtal = 100 \times \frac{\sum I_{net.}}{(\sum I_{tot.} - \sum I_{const.bgr.})} \quad (3.1)$$

$\sum I_{const.bgr.}$ is the sum of the constant background intensity which may arise from imperfections of the sample, X-ray optics of the instrument, sample fluorescence and scatter. $\sum I_{const.bgr.}$ was determined (separated from the crystalline peaks or $I_{net.}$ from an amorphous hump). This constant background value was entered in the scan parameter of HighScorePlus and the crystallinity automatically determined. The peak positions and corresponding intensity were

matched to ICDD reference patterns containing d-I (d- values and relative intensity) information's and the crystal phases and the unit cell determined.

3.4.1 Line profile Analysis

Line profile analysis is the extraction of microstrain and crystallite size information from a close examination of the profile width (FWHM) and shape. This was done in HighScorePlus on a range of peaks from 5° to 90°. The crystallite size was automatically calculated using the default instrumental broadening values **GAUSS $B_{instr.}$** and **LORENTZ $B_{instr.}$** stored in the peak list after FWHM variations have been deconvoluted to GAUSS and LORENTZ contributions. The results were then shown in the peak list as Williamson-Hall plot (**equation 3.6**). It relies on the principle that the approximate formulae for crystallite size broadening, β_L and microstrain broadening, β_e vary differently with respect to Bragg angle, θ:

$$\boldsymbol{\beta_L = \frac{K\lambda}{L\cos\theta}} \tag{3.2}$$

$$\boldsymbol{\beta_e = \varepsilon \tan\theta} \tag{3.3}$$

$\boldsymbol{\beta_L}$ and $\boldsymbol{\beta_e}$ varies as $\frac{\mathbf{1}}{\cos\theta}$ and $\tan\theta$, respectively. If both contributions are present then their combined effect should be determined by convolution. The convolution is given by

$$\boldsymbol{\beta = \beta_\varepsilon + \beta_L = \varepsilon \tan\theta + \frac{K\lambda}{L\cos\theta}} \tag{3.4}$$

$$\boldsymbol{\beta\cos\theta = \varepsilon \tan\theta\cos\theta + \frac{K\lambda}{L}} \tag{3.5}$$

$$\boldsymbol{\beta\cos\theta = \varepsilon \sin\theta + \frac{K\lambda}{L}} \tag{3.6}$$

Comparing **equation 3.6** to equation of a straight line; $\boldsymbol{y = mx + c}$ then $\boldsymbol{y = \beta \cos \theta}$, $\boldsymbol{x = \sin \theta}$, $\boldsymbol{m = \varepsilon}$ and $\boldsymbol{c = \frac{K\lambda}{L}}$

$\boldsymbol{\beta \cos \theta}$ was plotted against $\boldsymbol{\sin \theta}$ and the microstrain component obtained from the slope ($\boldsymbol{\varepsilon}$). The crystallite size component was determined from the $\boldsymbol{\beta \cos \theta}$ intercept ($\frac{\boldsymbol{K\lambda}}{\boldsymbol{L}}$), where $\boldsymbol{\lambda}$ is the wavelength of the used X-ray radiation, $\boldsymbol{\beta}$ is the peak width of the diffraction peak profile at full width at half maximum (FWHM) of the peak at maximum intensity, $\boldsymbol{\theta_{(hkl)}}$ is the peak diffraction angle that satisfies the Bragg law for the (h k l) plane and $\boldsymbol{L}$ is the average crystallite size. $\boldsymbol{K}$ is a constant relating to crystallite shape, normally taken as 0.9.

3.5 Pore-Scale Flow Model

The pore-scale flow in COMSOL Multiphysics using incompressible and stationary Brinkman equation, with Stokes-Brinkman assumption was used to model the flow in interstices of the samples microstructure. The assumption used was:

$$0 = -\nabla p + \nabla . \frac{\mu}{\varepsilon_p}(\nabla u + \nabla u^{\mathrm{T}}) - \frac{\mu}{\kappa} u, \nabla . u = 0 \qquad (3.7)$$

where $\boldsymbol{p}$ is the pressure, **u** is the Darcy's velocity field, $\boldsymbol{\mu}$ is the dynamic viscosity of the fluid, $\boldsymbol{\varepsilon_p}$ is the porosity and $\boldsymbol{\kappa}$ is permeability of the media. The boundaries conditions for the inlet pressure and the outlet pressure were defined. No slips were considered because the velocities are zero at the grain boundaries. The flow is symmetric about the top and bottom boundaries. The model boundary conditions are summarizes in **Table 3.1**. The porosity and the permeability were defined by the following equation:

$$\kappa(x,y) = \frac{\kappa_0}{100im1(x,y)+0.1} \tag{3.8}$$

$$\varepsilon_p = 1 - 0.99im1(x,y) \tag{3.9}$$

where im1 is the image function derived from the SEM image, which ranges from 0 to 1 as a function of position.

Table 3.1: Boundary conditions

BOUNDARY TYPE	BOUNDARY CONDITION	VALUE
Inlet	Pressure, no viscous stress	$p = p_0$
Outlet	Pressure, no viscous stress	$p = 0$
Grain walls	Wall	no slip
Symmetry sides	Symmetry	-

p_0 is specified pressure drop. Table 7 collects the relevant model data.

Table 3.2: Model data

QUANTITY	VALUE	DESCRIPTION
$\boldsymbol{\rho_0}$	1000 kg/m^3	Fluid density
$\boldsymbol{\mu_0}$	0.001 kg/(m.s)	Fluid dynamic viscosity
$\boldsymbol{p_0}$	0.715 Pa	Pressure drop

3.6 Water Absorption

Water absorption studies were carried out on sample S, sample I and sample J according to ASTM D570. Twenty replicates of each sample were used and statistical studies were done using regression analysis where Pearson product – moment coefficient (Peason's r) and adjusted R-square (Adj. R-square) determined. The choice of these three samples from the seven samples was based on the results from the pole-scale flow model in **section 3.6**. The specimen were confined in a desiccator for 24 h after subjected to a temperature of 50 ℃ in an oven for 24 h to take out any moisture in the sample. They were then weighed using Cole-Parmer digital balance to record the mass of the sample before immersion in water, m_w. The samples with known masses were totally immersed in a container and the mass after immersion, m_d recorded after every 10 days for 120 days. Water absorbed in percentages were determined using equation (2.17) and the moisture ratio, MR versus square root of time, $\sqrt{t}$ of immersion was plotted. The diffusion coefficient was determined from the slope using equation (2.21) and equation (2.22), respectively.

3.7 Enzymatic Degradation Tests

Enzymatic test was carried out on sample S, sample I and sample J. The samples were placed in phosphate buffer saline (PBS) containing α- amylase [1, 4-α-D-glucan- hydro-lase]; activity of 480 u/ml. Orbital shaker incubator was used to shake the samples in the saline at a temperature of 37 ℃ and revolution of 100 rev/min. The samples were taken out every 10 days up to 60 days. Samples were washed thoroughly before conditioning in an oven at 50 ℃ for 24 h and subjected to tensile testing to determine the percentage loss in tensile strength. Each sample was tested in five replicate.

Chapter 4

Experimental Results

4.1 X-ray Diffraction Results

XRD patterns of the samples listed in **Table 3.0** are shown in **Figure 4.0** and Figure **4.1**. Unmoulded LLDPE has two major peaks at 2θ = 21.5° and 23.8° which reflect the orthorhombic unit cell but when processed the moulded LLDPE major peaks appeared at $2\theta = 21.4°$ and 23.7° with a minor peak at $2\theta = 19.9°$ (see SP in **Figure 4.0** (a)) which shows presence of monoclinic phase (see **Appendix A** for details).

Cassava starch exhibits a semi-crystalline structure, the crystalline region is assigned to the well-ordered structure of amylopectin molecules inside the granule with typical crystallinity peaks of A- type, C-type or a mixture pattern with three major peaks at $\mathbf{2\theta \sim 15.1°, 17.1°}$ and $\mathbf{23.6°}$. Incorporation of cassava starch (see **Appendix B** for XRD patterns of starch) into LLDPE shifted the 2Theta position from 19.9° to 19.5° (SS in **Figure 4.0** (a)) and Pawley profile fitting of SS shows a peak at $\boldsymbol{2\theta}$ = 23.5° (**Figure 4.0** (b)).

Introduction of 1.0% by parts hydroxyapatite of crystallite size of 38.4 nm (see **Appendix C** for crystal information) into the composite further shifted the $\boldsymbol{2\theta}$ peak position of 19.5° to 19.1° (see SH in **Figure 4.0** (a)). Addition of 1.5% and 2.0% by parts of hydroxyapatite into the composite shifted the 19.1° $\boldsymbol{2\theta}$ peak position to the right; 19.2° and 19.4°, respectively (**Figure 4.1** (SI) and (SJ)). Addition of 2.5% and 3.0% of hydroxyapatite shifted the peak back to lower angles. The peak positions with their corresponding crystal structures and percentage crystallinity of the diffraction patterns of **Figure 4.0** and **Figure 4.1** are shown in **Table 4.0.** The

crystallite size and microstrain (lattice strain) in **Table 4.0** were determined from Williamson-Hall plot in HighScore Plus**.** The peak intensities of all the blends were lower than pure LLDPE.

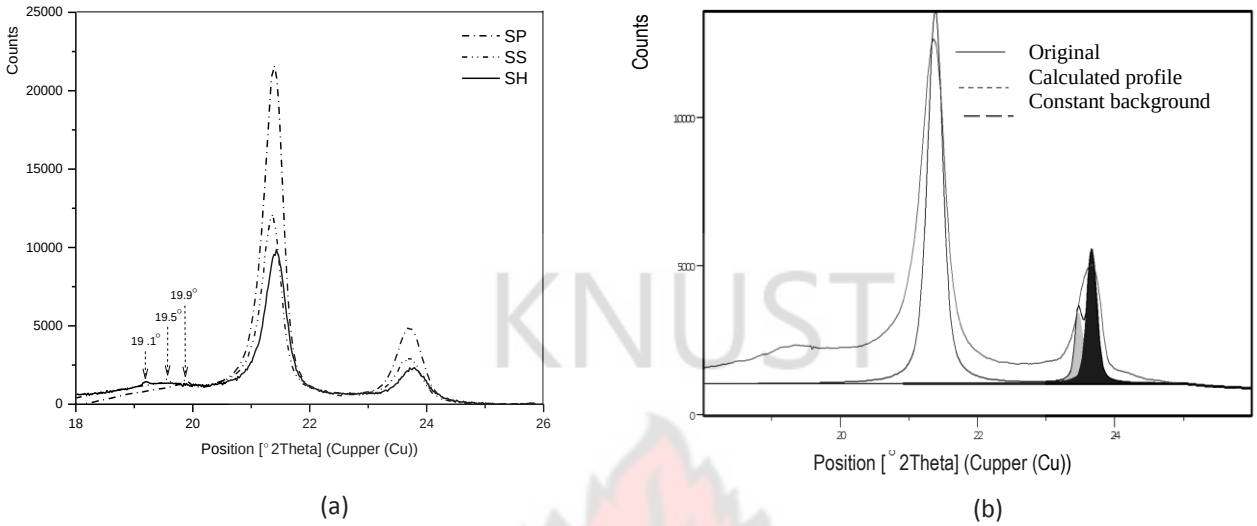

Figure 4.0 XRD patterns of (a) SP: moulded LLDPE, SS: LLDPE/starch (60/40 w/v) blend and SH: SS filled with 1.0 % by part of hydroxyapatite (b) Pawley profile fitting for XRD patterns of SS. The

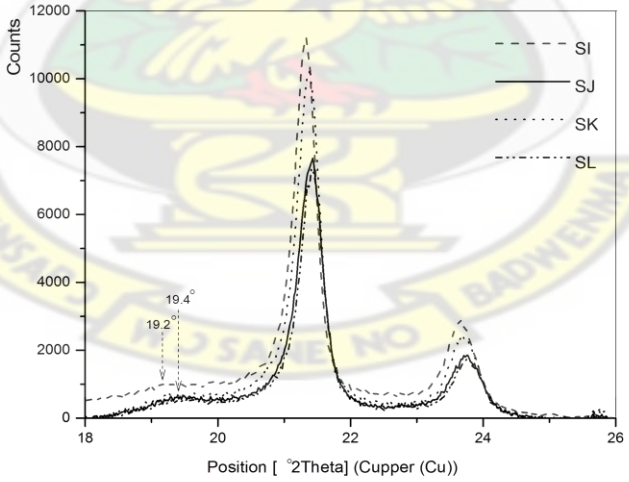

Figure 4.1 XRD patterns of LLDPE/starch blend filled with w/v % by parts of hydroxyapatite particles, SI: 1.5, SJ: 2.0, SK: 2.5, SL: 3.

Table 4.0: Diffraction data (peak positions for identified crystal structures) for LLDPE and LLDPE/starch hydroxyapatite composite Sample

Sample codes	Monoc	Ortho	Mono	Ortho	Crystallinity (%)	Crystallite size (nm)	Microstrain
SP	19.9	21.3	-	23.6	56.98	38	0.053
SS	19.5	21.4	23.5	23.8	42.88	44	0.033
SH	19.2	21.5	23.7	23.8	38.96	55	0.024
SI	19.2	21.3	-	23.6	44.02	40	0.043
SJ	19.4	21.4	-	23.7	52.13	37	0.044
SK	19.2	21.4	-	23.7	52.29	45	0.013
SL	19.3	21.4	23.8	23.9	52.29	46	0.004

4.2 Scanning Electron Microscopy (SEM) Results

The morphology of the composites under scanning electron microscopy was studied in order to determine the surface texture aggregation reinforcing phase. **Figure 4.2** compares the surface topology of the moulded LLDPE and that of LLDPE/starch blend. **Figure 4.2** (a) shows the surface of the moulded pure LLDPE. It could be seen in **Figure 4.2** (b) that addition of 40% hydrophilic starch into LLDPE produced a differential swelling of the surface.

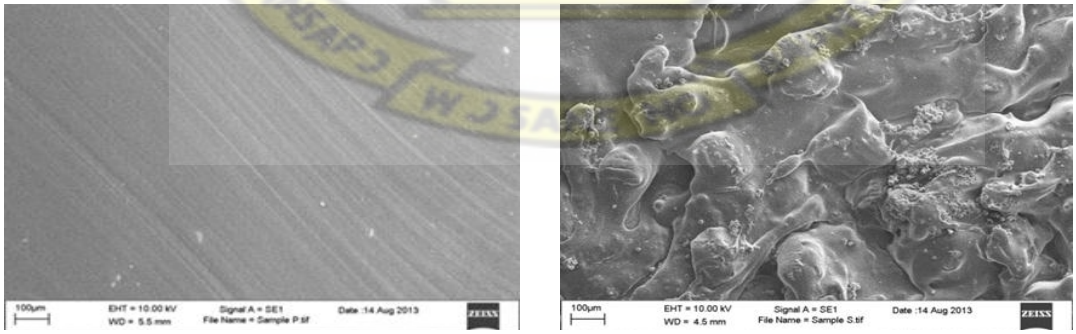

Figure 4.2 SEM micrographs of (a) pure LLDPE and (b) LLDPE/starch composite containing (60%) LLDPE and (40%) starch.

Addition of 1.0% by parts of hydroxyapatite to the composite reduces the surface swelling (See **Figure 4.3** (a)). Increasing the mineral content from 1.0% to 1.5% and to 2.0% by parts caused depressions on the surface which resulted in a spongy topology (**Figure 4.3** (b) and (c)). Further increase of mineral content from 2.0% to 2.5% showed wider depressions in the surface and this resulted in creating dents with perforations and microcracks at the surface (**Figure 4.3** (d)). Finally increase in hydroxyapatite content from 2.5% to 3.0% resulted in multiphase structure which is indication of immiscibility (see **Figure 4.3** (e)).

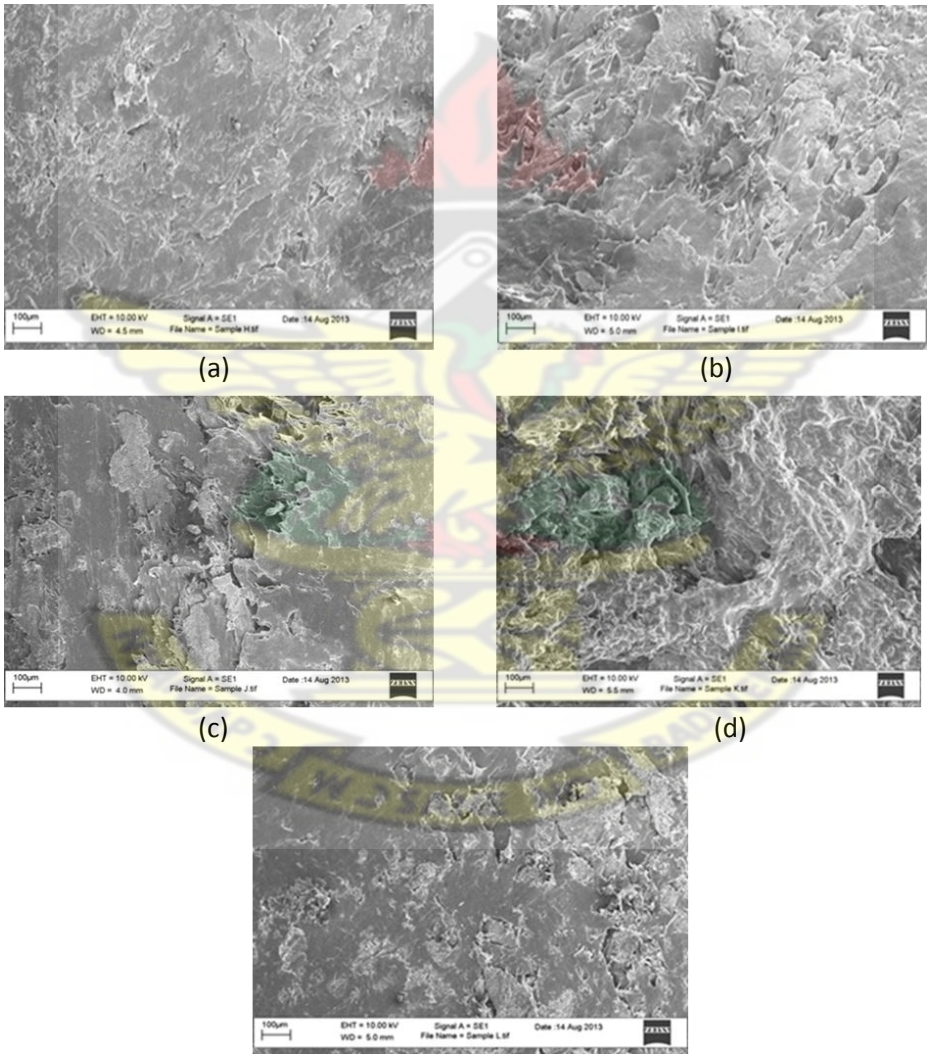

Figure 4.3 SEM micrographs of LLDPE/starch blend filled with (a) 1.0% (b) 1.5% (c) 2.0% (d) 2.5% and (e) 3.0% of hydroxyapatite.

4.3 Tensile Properties

The tensile strength, tensile modulus and the elongation at break of the LLDPE, LLDPE/starch blend and blends filled with hydroxyapatite are shown in **Figure 4.4** and **Figure 4.5** (see **Appendix D** for the load - extension graphs). The tensile strength and the elongation of LLDPE are highest. The Tensile modulus of the LLDPE/starch blend is highest and almost twice the modulus of LLDPE alone. Addition of hydroxyapatite into LLDPE/starch blend improves tensile strength and modulus of the blend. Introduction of the hydroxyapatite into the blend showed a Gaussian distribution and the ANOVA showed Prob>F values of the blends and blends filled with hydroxyapatite greater than the F values, indicating significant change in the means of the tensile strength and modulus. The percentage elongation has an inverse relation with the tensile modulus. Increasing modulus decreases elongation. **Table 4.0** shows the F- statistics for the tensile properties.

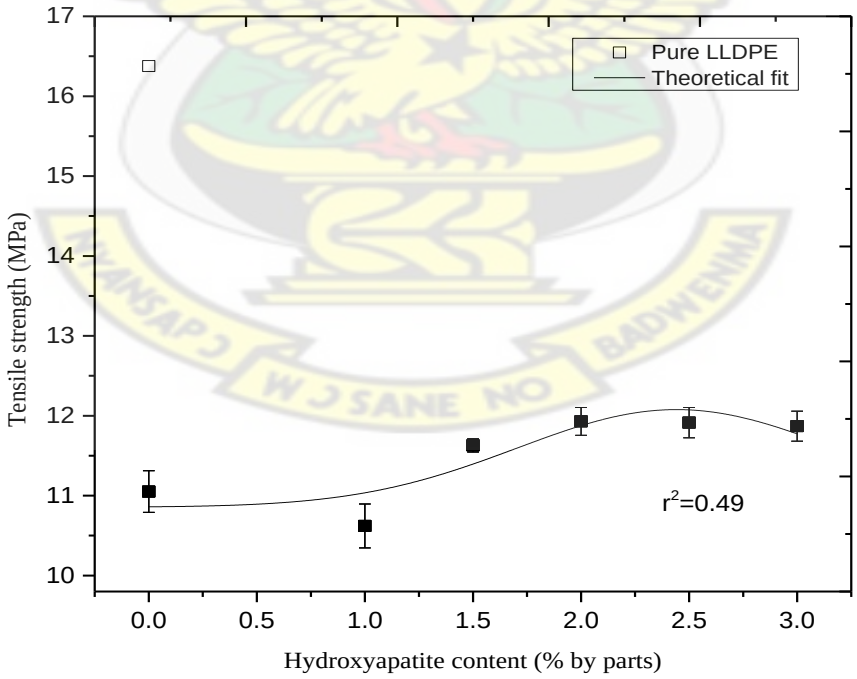

Figure 4.4 Variation of tensile strength with hydroxyapatite content. Error bars are standard errors.

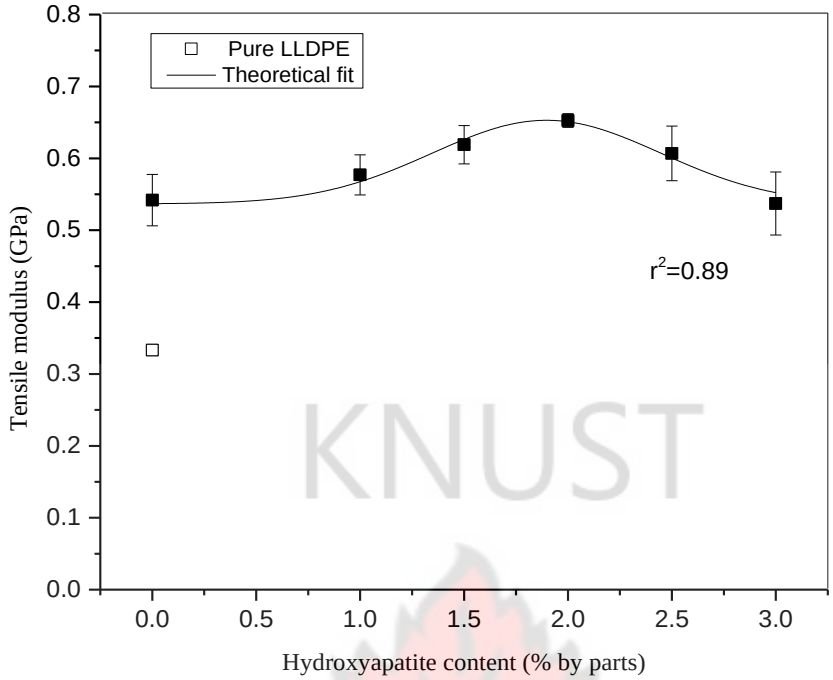

Figure 4.5 Tensile modulus versus hydroxyapatite content of LLPDE/starch blend filled with hydroxyapatite. Error bars are standard errors.

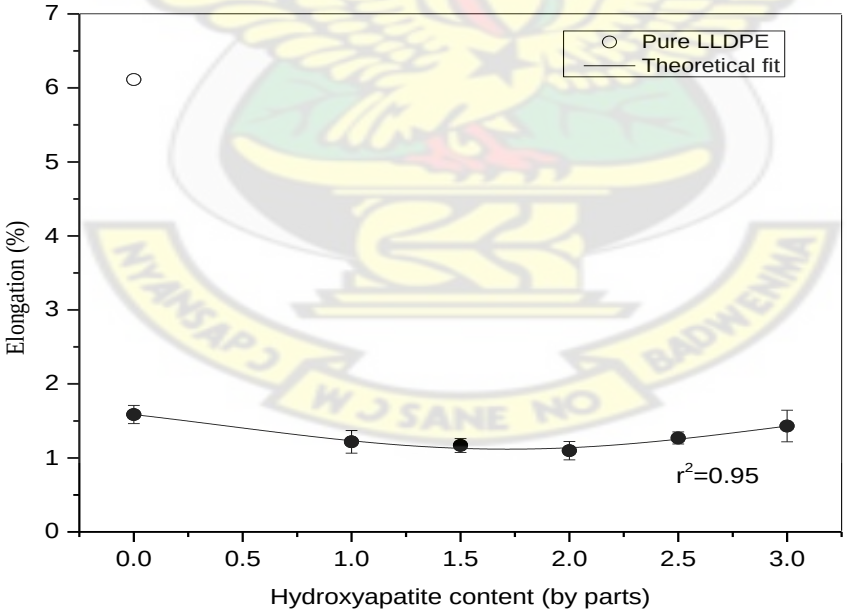

Figure 4.6 Elongation at break versus hydroxyapatite content of LLPDE/starch blend filled with hydroxyapatite. Error bars are standard errors.

Table 4.1: F-statistics for tensile strength, modulus and elongation

		DF	Sum of Squares	Mean Square	F Value	Prob>F
Tensile strength						
C	Regression	4	795.00319	198.7508	1321.13412	7.56448E-4
	Residual	2	0.30088	0.15044		
	Uncorrected	6	795.30407			
	Corrected	5	1.48169			
Tensile modulus						
E	Regression	4	2.09167	0.52292	2372.35909	4.21373E-4
	Residual	2	4.40842E-4	2.20421E-4		
	Uncorrected	6	2.09211			
	Corrected	5	0.01032			
Elongation						
B	Regression	4	10.22272	2.55568	1455.74755	6.86539E-4
	Residual	2	0.00351	0.00176		
	Uncorrected	6	10.22623			
	Corrected	5	0.1646			

4.4 Pore-Scale Flow

Figure 4.7 presents simulation result of velocity flow of water through the sample surfaces. The results were generated from COMSOL Multiphysics 4.3 using the Brinkman equation. The velocity field is high and uniform with pure LLDPE (sample SP) see **Figure 4.7** (a) but the blends have varying velocity fields. High velocity fields are indicated by thick arrows and low velocity fields with thin arrows. The regions with the thin arrows are where the water permeability and pressure are high.

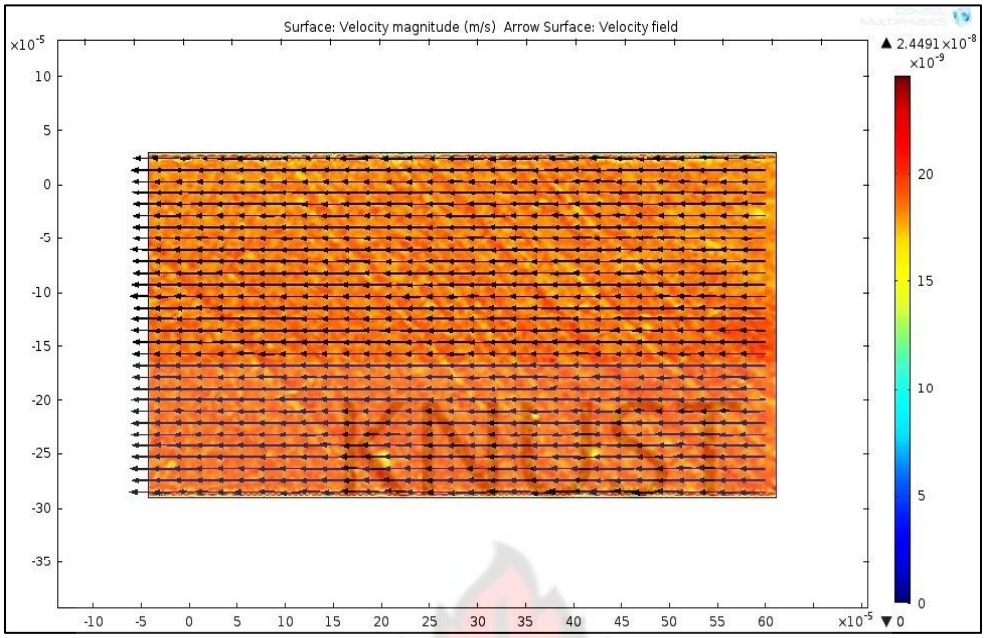

(a)

Figure 4.7 Surface and arrow plots of the velocity field calculated by the Brinkman Equations interface. The regions with thin arrows indicate low velocity (colour blue being the lowest) and regions with thick arrows indicate high velocity (a) SP: pure LLDPE.

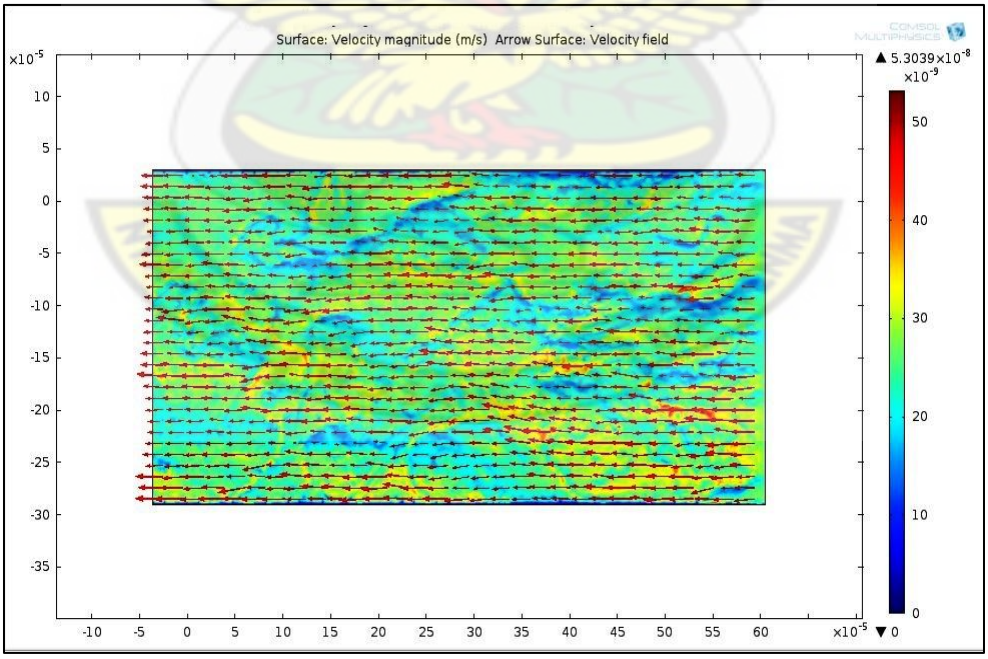

(b)

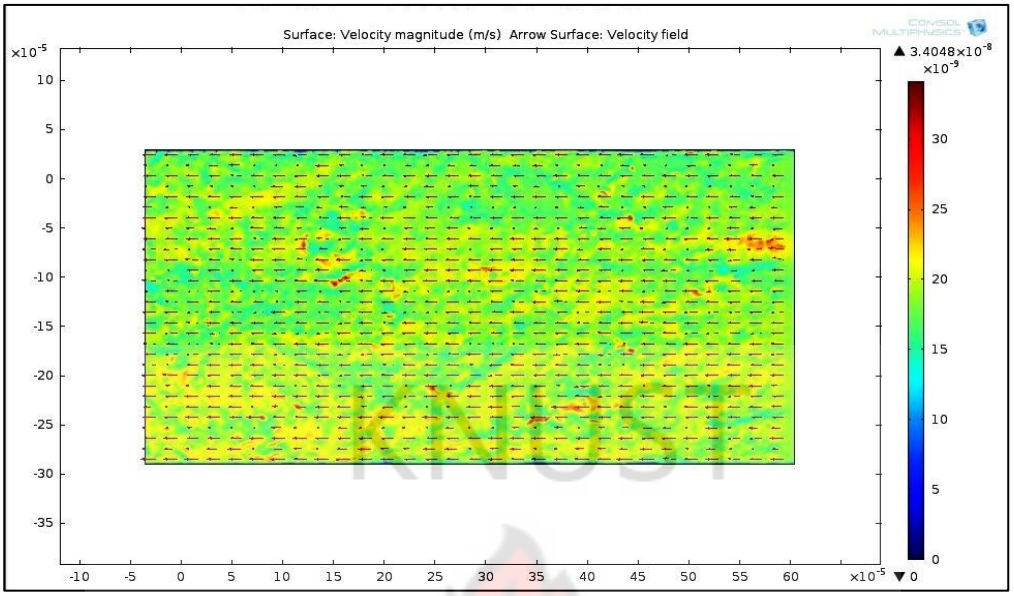

(c)

Figure 4.7 Continues (b) SS: LLDPE/starch (60/40 w/v) (c) SH: LLDPE/starch blend filled with 1.0% by parts hydroxyapatite.

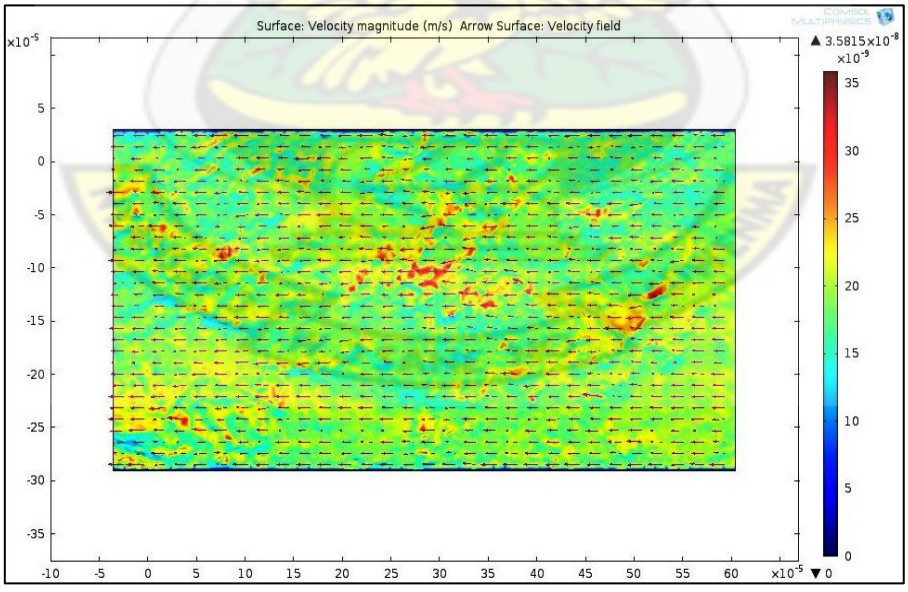

(d)

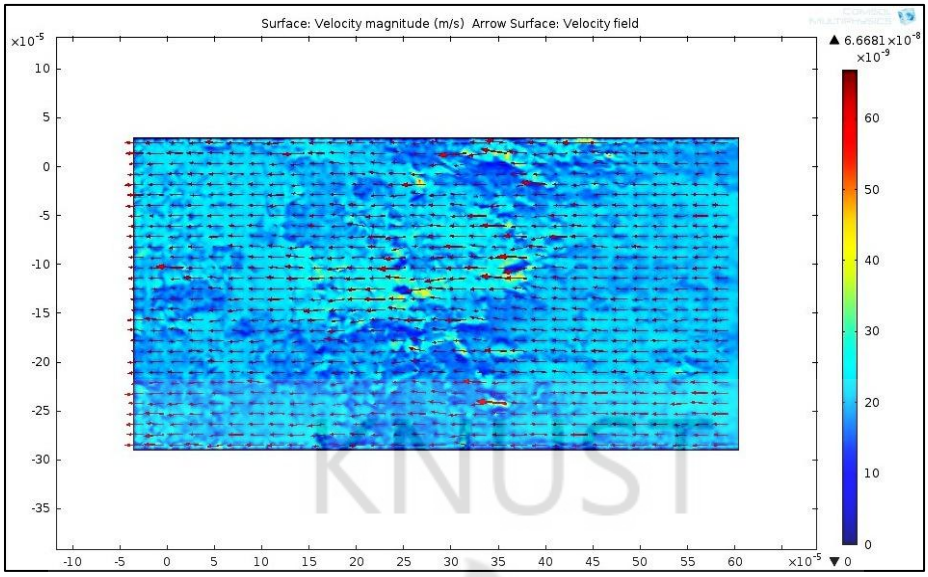

(e)

Figure 4.7 Continues (d) SI: LLDPE/starch blend filled with 1.5% by parts hydroxyapatite (e) SJ: LLDPE/starch blend filled with 2.0% by parts hydroxyapatite.

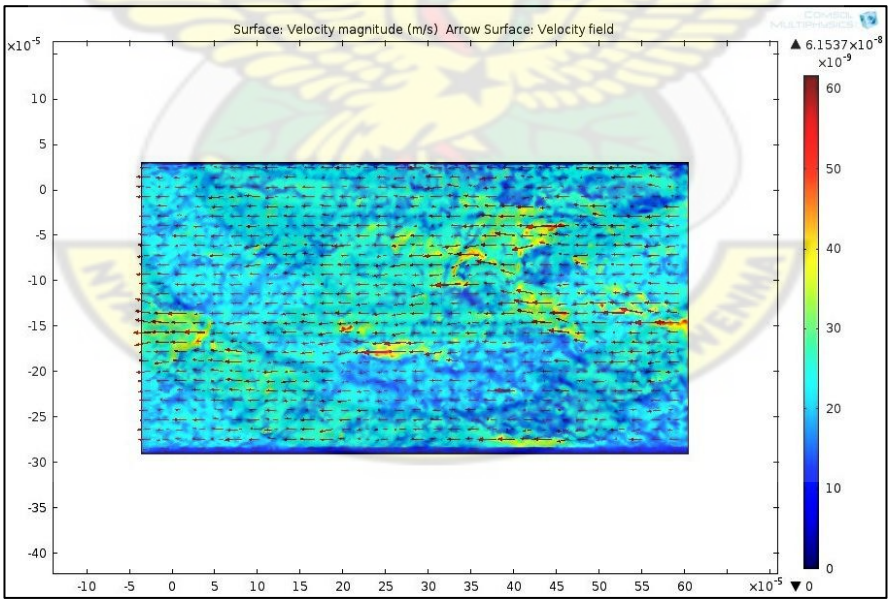

(f)

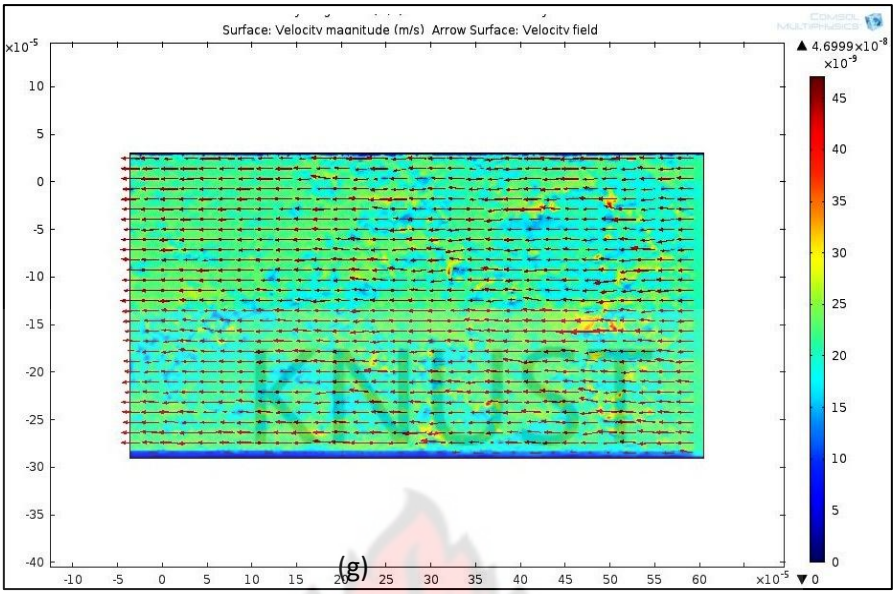

Figure 4.7 Continues (f) SK: LLDPE/starch blend filled with 2.5% by parts hydroxyapatite (g) SL: LLDPE/starch blend filled with 3.0% by parts hydroxyapatite.

4.5 Water Absorption

Figure 4.8 shows the variation in water uptake of samples with time of immersion. Water uptake increased with immersion time up to 30 days but the rate of uptake is higher in LLDPE/starch blend than in LLDPE/starch blend filled with hydroxyapatite (see diffusion coefficient for SS, SI and SJ in **Table 4.2**). Sample SI decreased more slowly with time than Sample SJ. **Appendix E** shows statistics for **Figure 4.8.**

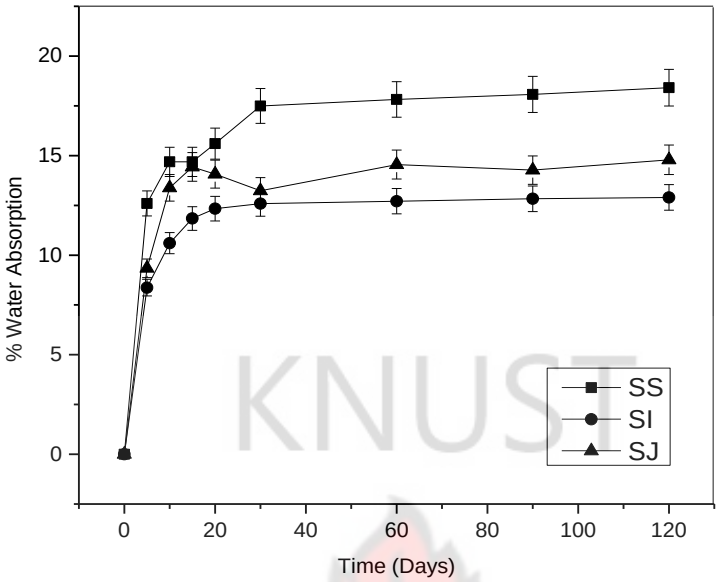

Figure 4.8 Variation of water uptake of LLDPE/starch blend (SS) and LLDPE/starch blend filled with 1.5% by parts hydroxyapatite (SI) and LLDPE/starch blend filled with 2.0% by parts hydroxyapatite (SJ) with time of immersion

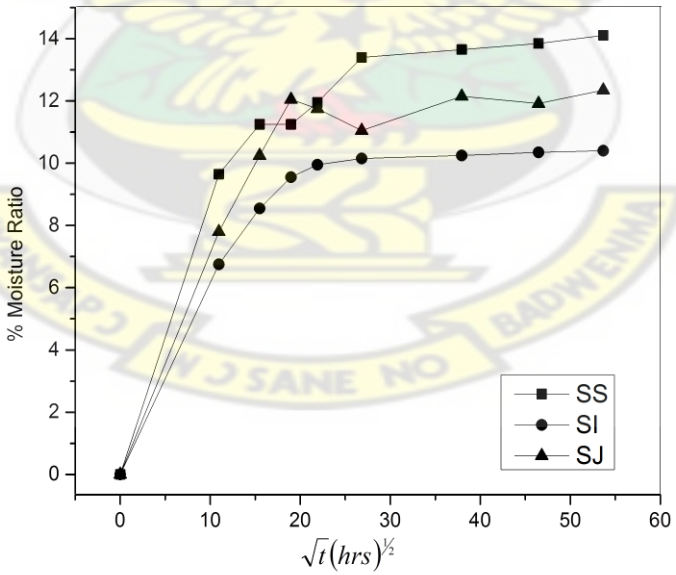

Figure 4.9 Moisture ratio versus square root of time in hours of LLDPE/starch blend (SS) and LLDPE/starch blend filled with 1.5% by parts hydroxyapatite (SI) and LLDPE/starch blend filled with 2.0% by parts hydroxyapatite (SJ). The slopes of the initial straight portion of the curves were used to calculate the diffusion coefficient of individual samples.

Table 4.2: Water uptake parameters of blends

Sample codes	Saturation water uptake (M_∞)	Initial slope of plot (K)	Diffusion coefficient, $D*10^{-4}(m^2/s)$
SS	0.1410	0.0088	1.91
SI	0.1040	0.0062	1.74
SJ	0.1235	0.0075	1.81

4.6 Enzymatic Degradation inferred from tensile properties

Figure 4.10 and **Figure 4.11** show the residual tensile strength and the percentage loss in tensile strength with time for LLDPE/starch blend (SS) and LLDPE/starch blend filled with hydroxyapatite (SI and SJ) after 60 days of immersion in α-amylase solution. The reduction in tensile strength decreased with time for all the samples and follows the residual property model (RMP). Sample SS showed 32.73% reduction of its tensile strength in 60 days whiles SI and SJ lost 10.41 and 19.71, respectively (see **Figure 4.11**). F- Statistics for the fitting is presented in **Table 4.3.** The Prob>F for the entire samples is less than F values**;** this indicates a significant strength loss.

The residual property model for the tensile modulus and percentage loss in tensile modulus are shown in **Figure 4.12** and in **Figure 4.13**, respectively. The residual property model for LLDPE/starch blend (SS) shows a polynomial fit. The correlation for LLDPE/starch blend filled with hydroxyapatite was significant (see SI and SJ in **Table 4.3**).

The mechanical degradation behaviour for elongation did not follow the residual property model. The results showed gain in elongation. **Figure 4.14** presents percentage gain in elongation with immersion time. The polynomial fitting for LLDPE/starch blend and blends

filled with 1.5% hydroxyapatite (SI) showed a good correlation and the ANOVA showed all F vales greater than Prob> F indicating significance. Blend with 2.0% hydroxyapatite showed high Prob> F value than the F value (See **Table 4.5**).

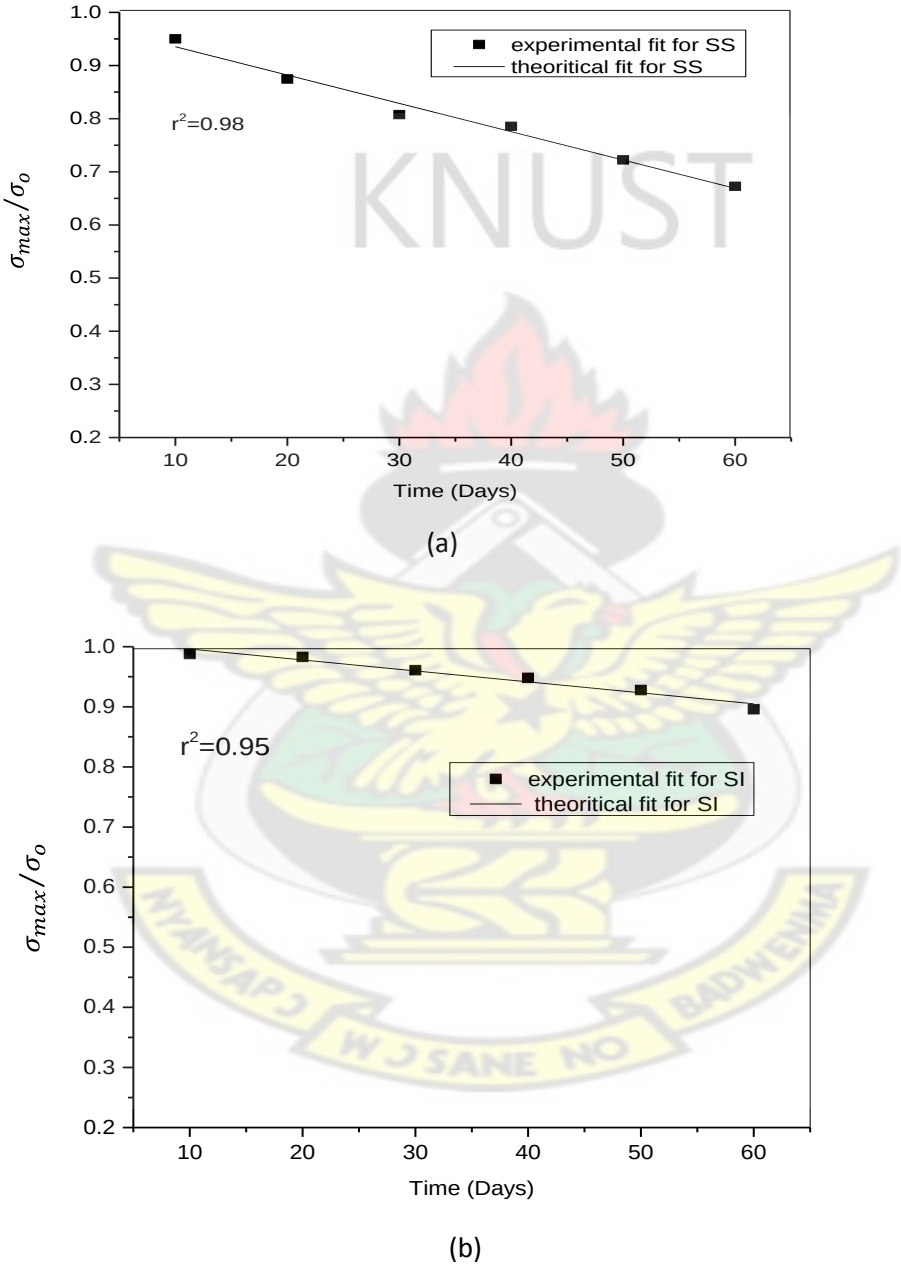

Figure 4.10 Residual property module for tensile strength (a) SS: LLDPE/starch blend (b) SI: LLDPE/starch blend filled with 1.5% by parts hydroxyapatite.

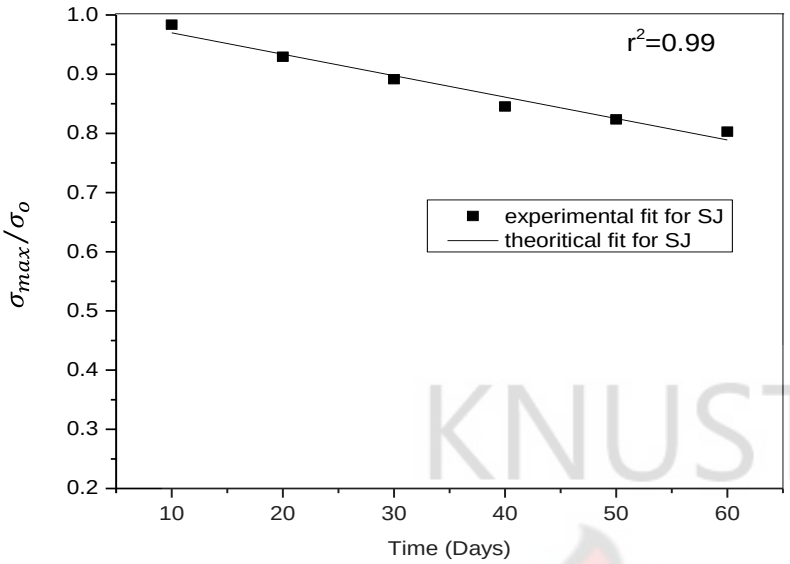

(c)

Figure 4.10 Continues (c) SI: LLDPE/starch blend filled with 2.0% by parts hydroxyapatite.

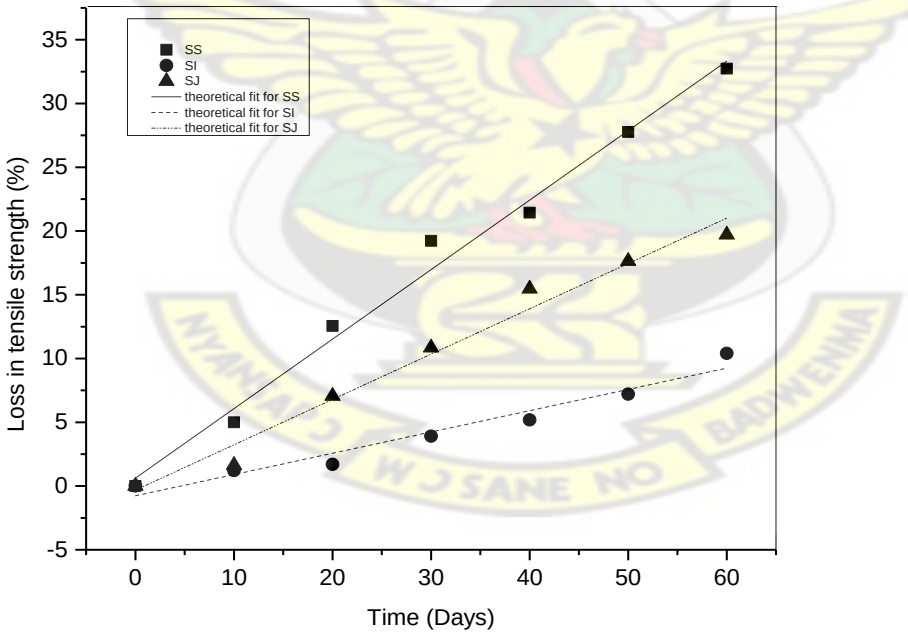

Figure 4.11 Percentage reduction in tensile strength starch/PE blend and starch/PE blend filled with hydroxyapatite (SI: 1.5% parts, SJ: 1.5% parts) with time of immersion.

Table 4.3: F-statistics for percentage reduction in tensile strength

		DF	Sum of Squares	Mean Square	F Value	Prob>F
SS	Model	1	831.9424	831.9424	460.90448	4.06662E-6
	Error	5	9.025110	1.805020		
	Total	6	840.9675			
SI	Model	1	77.94811	77.94811	109.45958	1.37585E-4
	Error	5	3.560590	0.712120		
	Total	6	81.50870			
SJ	Model	1	353.83670	353.8367	247.73871	1.88243E-5
	Error	5	7.1413300	1.428270		
	Total	6	360.97803			

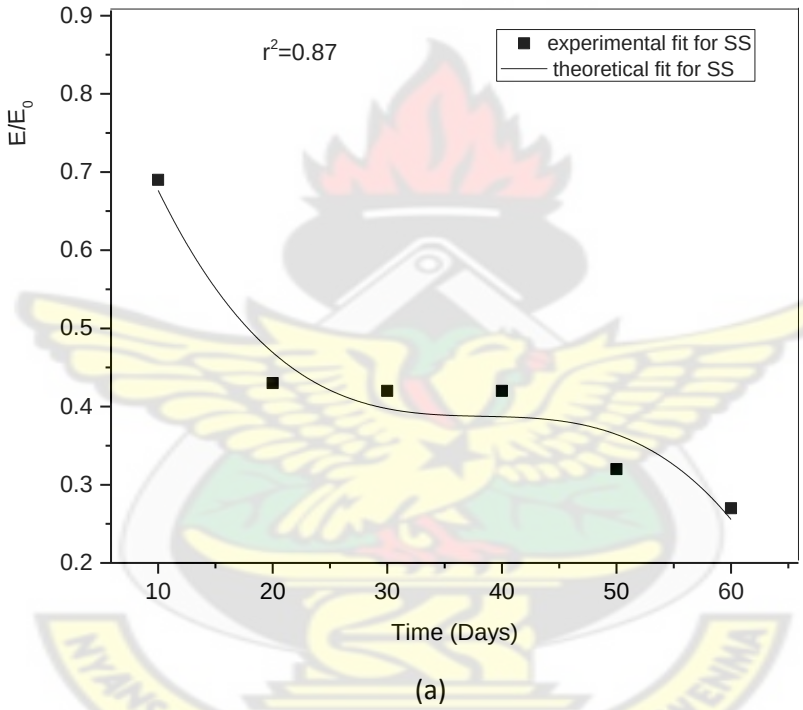

(a)

Figure 4.12 Residual property module for Young's modulus (a) SS: LLDPE/starch blend (b) SI: LLDPE/starch blend filled with 1.5% by parts hydroxyapatite.

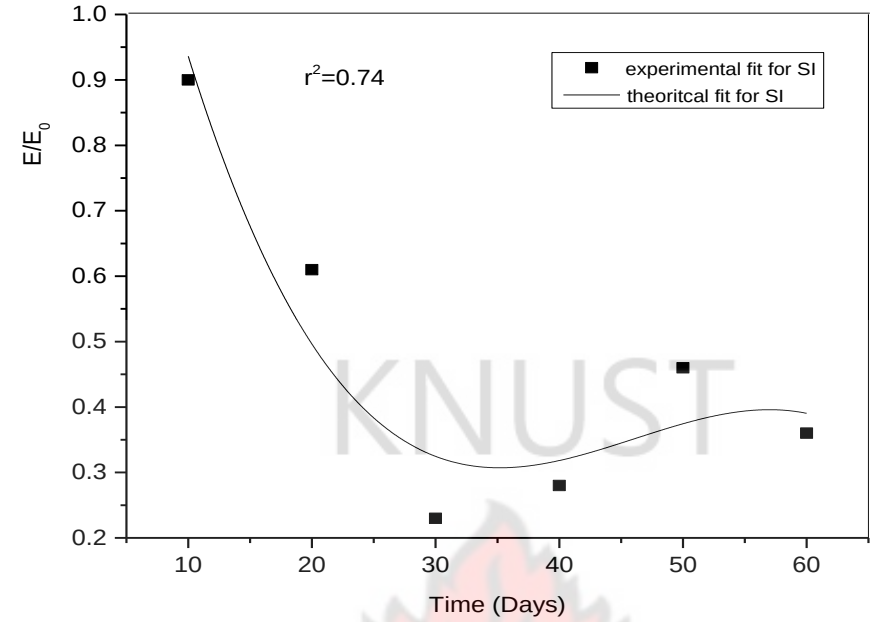

(b)

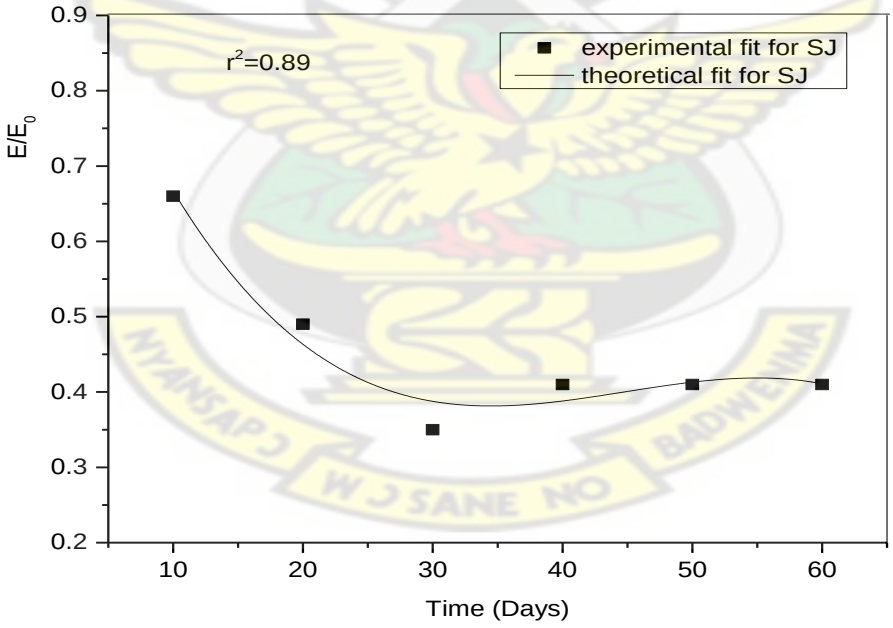

(c)

Figure 4.12 Continues (c) SJ: LLDPE/starch blend filled with 2.0% by parts hydroxyapatite.

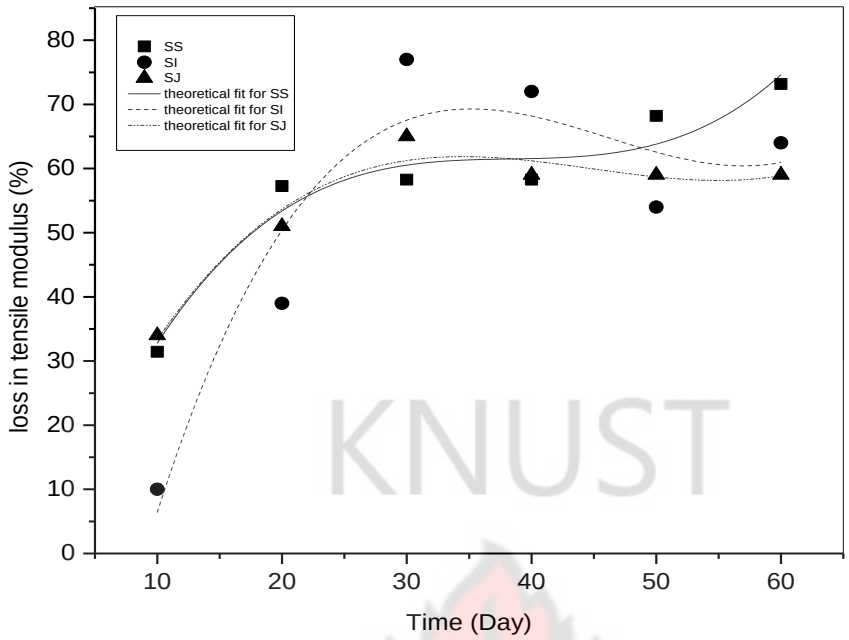

Figure 4.13 Percentage reduction in tensile modulus of starch/PE blend (SS) and starch/PE blends filled with hydroxyapatite (SI: 1.5% parts, SJ: 2.0% parts) with time of immersion.

Table 4.4: F-statistics for percentage reduction in tensile modulus

		DF	Sum of Squares	Mean Square	F Value	Prob>F
SS	Model	3	985.90859	328.6362	12.10487	0.07727
	Error	2	54.29816	27.14908		
	Total	5	1040.20676			
SI	Model	3	2774.43651	924.81217	5.62372	0.15468
	Error	2	328.89683	164.44841		
	Total	5	3103.33333			
SJ	Model	3	576.85714	192.28571	14.43432	0.06548
	Error	2	26.64286	13.32143		
	Total	5	603.5			

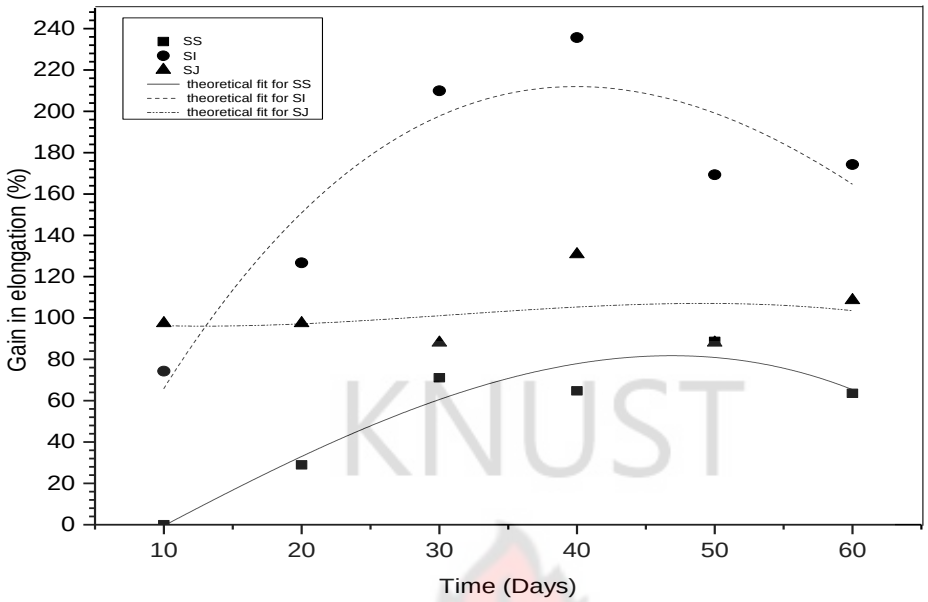

Figure 4.14 Percentage gain in elongation modulus of LLDPE/starch blend (SS) and LLDPE/starch blends filled with hydroxyapatite (SI: 1.5% parts, SJ: 1.5% parts) with time of immersion.

Table 4.5: F-statistics for percentage gain in elongation

		DF	Sum of Squares	Mean Square	F Value	Prob>F
SS	Model	3	4873.39447	1624.46482	8.9320	0.10235
	Error	2	363.74013	181.87007		
	Total	5	5237.13461			
SI	Model	3	14467.80039	4822.60013	4.11895	0.20150
	Error	2	2341.66274	1170.83137		
	Total	5	16809.46312			
SJ	Model	3	95.09431	31.69810	0.05254	0.98026
	Error	2	1206.68084	603.34042		
	Total	5	1301.77515			

4.7 Enzymatic Degradation inferred from Optical images

Figure 4.15 shows optical images of the sample surface after 60 days of immersion in distilled water and in PBS solution containing α-amylase. The optical micrographs of the surface show the presence of pores and agglomerates. The pores are larger in Sample SS (width < 518 µm) followed by Sample SJ (width < 300 µm) and Sample SI (width < 175 µm) (see **Figure 4.15** (a), (c) and (b), respectively).

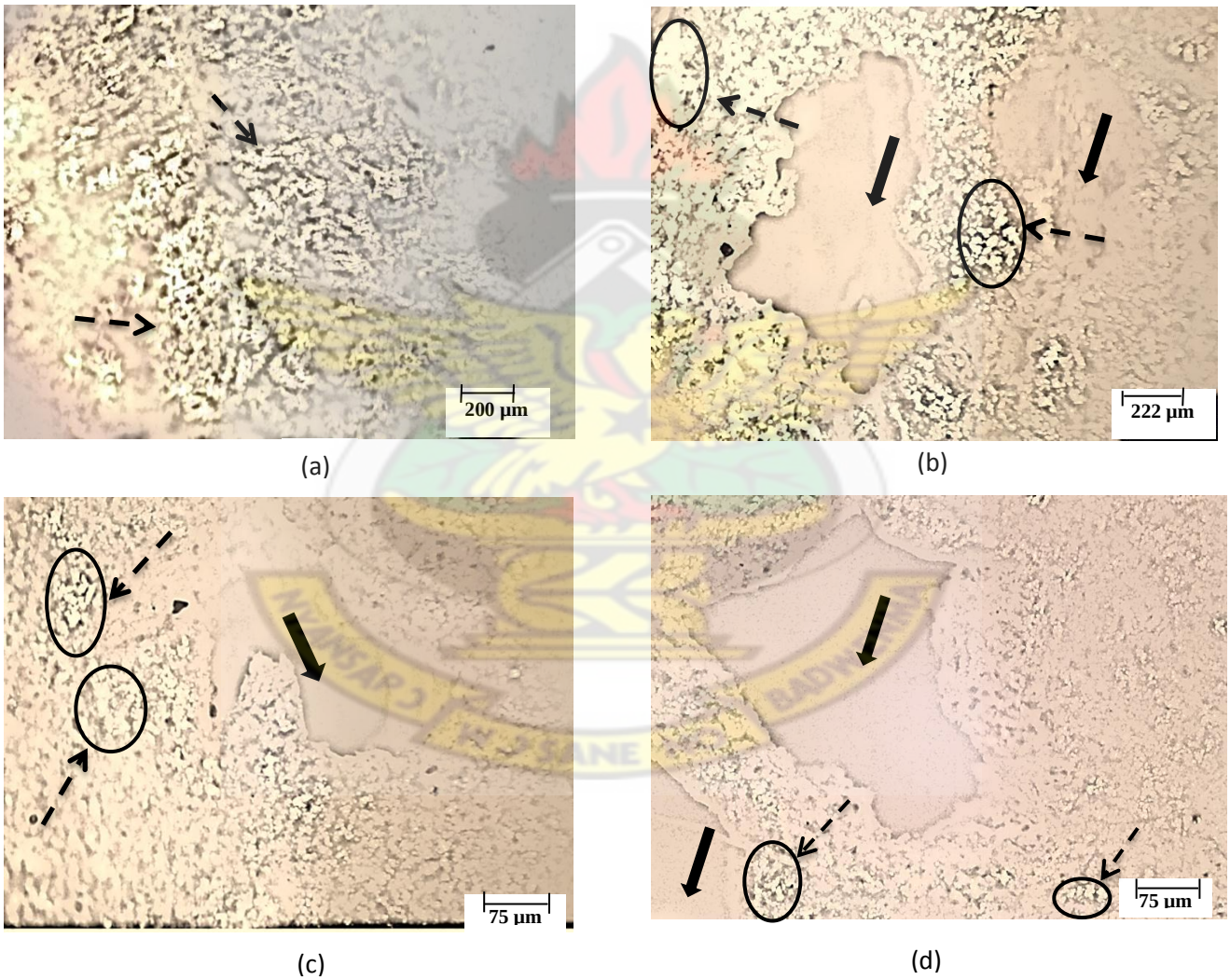

Figure 4.15 Optical images of the surface of the LLDPE/starch blend and LLDPE/starch blends filled with hydroxyapatite in distilled water and in PBS solution containing α-amylase for 60 days (a) SS in distilled water (b) SS α-amylase solution (c) SI α-amylase solution (d) SJ α-amylase solution. Dark arrows indicate pores and dash arrows for agglomerates. All the samples have magnification of x100.

Chapter five

Discussion

5.1 Tensile Properties Linked to Structure and Morphology

The tensile strength, tensile modulus and elongation at break of the moulded LLDPE, LLDPE/starch blend and LLDPE/starch blend filled with hydroxyapatite shown in **Table 3.0** depended on percentage crystallinity, 2Theta peak transposition and morphology.

The tensile strength of the moulded LLDPE is high, compared to the blended samples. Tensile strength of a material is greatly affected when a material undergoes small or large scale plastic deformation. The crystallinity and lattice planes of the material are altered, thus returning high tensile strength values. The blending of starch and LLDPE reduced crystallinity and introduced more amorphous phases into the LLDPE (see crystallinity (%) in **Table 4.0**). This occurred because starch has a semi - crystalline structure with high amorphous phase content; due to the presence of amylose **(Van Soest and Vliegenthart, 1997)**. The reduction of percentage crystallinity resulted in the reduction of tensile strength of LLDPE. Introduction of hydroxyapatite into the LLDPE/starch blend showed increase in crytallinity (see **Table 4.0**) and improved tensile strength (**Figure 4.4**). The improvement was statistically significant. Varying hydroxyapatite content in the blend increased the tensile strength to a point after which the strength stabilized. Incorporation of hydroxyapatite did not give strength values comparable to that of the LLDPE probably due to the fact that inclusion could not cause large enough lattice deformation. Interlamellar slip/rotation was evidently not achieved. The XRD results in **Table 4.0** confirm that the inclusion could not produce any significant lattice deformation (microstrain). Russel et al., (1997) reported that large strain deformation leading to high tensile strength could be achieved by applying excessive trauma (tension or compressive) to PE.

The 2θ peak transposition of the XRD patterns has been noticed to affect the tensile modulus of the blends. Introduction of starch into LLDPE stretched the LLDPE lattice and the 2θ peak positions were translocated. This result might be due to starch flowing through the amorphous phase of LLDPE resulting in interlamellar separation as reviewed in **chapter two**. The crystallite size of LLDPE/starch blend in **Table 4.0** shows peak broadening different from that of LLDPE and this confirms the existence of interlamellar separation caused by starch incorporation into LLDPE. The interlamellar separation caused the peak transpositions and resulted in evolvement of the second monoclinic phase of LLDPE (see **Figure 4.0** (b)). The evolvement could be likely responsible for the higher modulus of LLDPE/starch blend. The interlamellar separation of the amorphous tie chains in blends could also be explained using the SEM micrograph in **Figure 4.2** (b). The swelling shown in the micrograph results from high surface tension existing between the intermediate phase of LLDPE/starch blend and was due to non-covalent bonding between the starch molecules and attributed to the presence of the hydroxyl group of starch **(Hoover, 2001)**. Amylose has inherently absorbed water molecules which are liberated under high temperature and pressure and this was observed during processing.

Even though the introduction of small amounts of hydroxyapatite in the blend did not produce large lattice deformation, its role might be to improve the intermediate phase of the blend through hydrogen bonding as illustrated in **Appendix F**. Addition of 1.0% by parts of hydroxyapatite reduces surface tension. Percentage crystallinity declined and tensile strength decreased. This retrogression is suspected to be due to hydroxyapatite elongating amorphous tie chains of the blend (see SH in **Figure 4.0** (a) for pattern stretching), in effect enhancing tensile modulus. The SEM micrograph in **Figure 4.3** (a) shows the disappearance of the surface

swelling **(**see **Figure 4.2** (b)**)** and that confirms a reduction of the surface tension of the blend. Reduction of interfacial surface tension is characteristic of a compatibilizer.

The surface tension depends on the intermediate layer thickness as described in **equation 2.6**. Addition of 1.5% and 2.0% by parts content of hydroxyapatite showed improved interactions at the blend surface. The spongy morphology in **Figure 4.3** (b) and (c), respectively is believed to be as a result of interactions between the hydroxyl groups of hydroxyapatite and the hydroxyl groups of LLDPE/starch. The blends were miscible and gave relatively high tensile strength and tensile modulus. The blends containing 2.5% and 3.0% by parts hydroxyapatite did not show much improvement in tensile strength. Rather, there was a decline in modulus for samples with 2.0% by parts hydroxyapatite. The XRD results in **Table 4.0** show that as hydroxyapatite content is increased, crystallinity of the blend also increased. The high crystallinity is suspected to have decreased the intermediate phase volume fraction and thus increased the surface tension. This reason is in line with the explanation from **Alamo et al., (1994).** The high surface tension resulted in wider depressions in the surface thus creating dents with perforations and microcracks at the surface (see SEM micrograph in **Figure 4.3** (d)). The SEM micrographs of the blend showed immiscibility.

Percentage elongation at break of moulded LLDPE is highest. Incorporation of starch into LLDPE reduced the elongation at break. Elongation is highly sensitive to the interface state of the blends. The elongation at break which decreased with the starch content could be attributed to the phenomenon that the starch granule containing hydroxyl groups on its surface is highly hydrophilic, whereas LLDPE is nonpolar. This reason is similar to the explanation for the behaviour of sago starch mixed-LDPE (**Hoque et al., 2013**), at higher starch contents, filler-filler interaction becomes more pronounced than filler-matrix interaction which reduces the effective cross-sectional area of the polymer sample caused by the presence of starch particles. The

applied stress is not transferred accordingly from the polymer matrix to the rigid starch particles, and hence the effective stress experienced by the matrix is essentially higher LDPE (**Hoque et al., 2013**).

5.2 Enzymatic Degradation Linked to Water Absorption

The rapid moisture uptake in LLDPE/starch blends is mainly due to the hydrophilic nature of starch and resulted in surface agglomeration as shown in **Figure 4.18**. The surface agglomeration was due to hydrolysis (see **Figure 4.15** (a)). The starch being hydrophilic in nature retains moisture and provided higher oxygen permeability for enzymatic attack **(Rutkowska et al., 2002)**. This created pores for water to diffuse through the blends, contributing to degradation. The diffusion is faster at the surface than the interior (see SS in **Figure 4.8**) so the mechanism of degradation could be surface erosion as confirmed with the optical images of the degraded blends in **Figure 4.15**. Sample SS recorded faster rate of absorption (see SS in **Table 4.2** for diffusion coefficient) in the first few days of immersion time resulting in the formation of a lager pores of width $\leq \mathbf{518}\ \boldsymbol{\mu m}$. This observation of moisture uptake of LLDPE/cassava-starch blends is in line with moisture uptake of sago-starch-filled LLDPE blends reported in literature **(Danjaji et al., 2002)**.

Moisture uptake of blends filled with hydroxyapatite declined and it is believed that the hydroxyapatite particles control the hydrophilicity through hydrogen bonding. Introduction of 1.5 % by parts of hydroxyapatite (Sample SI) provides enough hydroxyl groups to bond with the hydrogen groups of starch in the blend reducing the rate of water absorption (**Figure 4.8**) and thus showed a smaller pore width $\leq \mathbf{175}\ \boldsymbol{\mu m}$ in the same immersion period of 60 days, indicating a reduction of degradation rate.

The incorporation of 2.0% by parts of hydroxyapatite in to the blend led to introduction of more hydroxyl groups. The hydroxyl groups interacted with hydrogen from starch and after saturation the remaining hydroxyl groups of hydroxyapatite begin to introduce hydrophillicity into the blend again. The remaining hydroxyl groups of hydroxyapatite introduce high hydrophilicity into the blend and raise the water absorption again (see SJ in **Figure 4.8**) and the maximum surface pore diameter increases from $\mathbf{175}\ \boldsymbol{\mu m}$ to $\mathbf{300}\ \boldsymbol{\mu m}$. The water absorption curve shows a monotonic behaviour. The rate of water diffusivity through Sample SJ rises during the initial days of immersion and then decreases, and increases again. As the hydroxyapatite content is increased in the blend, more hydroxyl group is been introduced. It was observed that the blends containing 2.0% by parts hydroxyapatite tried to achieve buoyancy during immersion and released bubbles. This suggests that introduction of 2.0% by parts hydroxyapatite into the blend created more pores than blends filled with 1.5% by parts of hydroxyapatite. Air fills the pores and during immersion in water, hydroxyl groups of hydroxyapatite pull water molecules and then release bubbles. The blend releases air and absorbs water. The absorption might have a linear relation with how much air the blend releases. This could be the reason for the monotonic absorption behaviour of Sample SJ.

5.3 Enzymatic Degradation Linked to Residual Property Model and Tensile Properties

Figure 4.10 and **Figure 4.11** show residual property module in tensile strength and percentage loss in tensile strength of samples, respectively after 60 days of immersion in α-amylase solution. All the samples reduced in strength but LLDPE/starch blend (Sample SS) showed a greater reduction in tensile strength than LLDPE/starch filled with 2.0% (Sample

SI) by parts of hydroxyapatite. The trends correspond with the slope of the residual property model determined from regression analysis. The slope is highest in Sample SS followed by Sample SJ and then Sample SI. This trend is in agreement with observations of higher mechanical degradation in Sample SS followed by Sample SJ and then Sample SI. The result has a direct proportional relation to the water uptake of the blends. LLDPE/starch blends lost **32.73%** of it tensile strength after 60 days, LLDPE/starch filled with 2.0% lost **19.71%** and LLDPE/starch filled with 1.5% lost **10.41%** of it tensile strength after 60 days (see SS, SJ and SI in **Figure 4.11**). The strength lost is due to surface erosion as confirmed with optical micrographs shown in **Figure 4.15** (a), (b) and (c). LLDPE/starch blend micrographs show large holes at the surface, followed by starch/LLDPE filled with 2.0% hydroxyapatite and then starch/LLDPE filled with 1.5%. The surface agglomeration might come from interactions of starch granules and hydroxyapatite crystallite suggesting that degradation was not due to enzyme attack alone but hydrolysis by water or other constituents in solution (see **Figure 4.15** (a)).

The result from the residual property model for tensile modulus of the blends was statistically significant based on the polynomial fitting and this was due to flexibility introduced into the blends. The modulus lost does not vary with immersion time linearly. It would therefore be difficult to predict degradation of blends based on modulus.

The gain in percentage elongation of LLDPE/starch blend (SS) and LLDPE/starch blend filled with 2.0% (SJ) and 1.5% (SI) by part hydroxyapatite confirm introduction of ductility. The gain in percentage elongation for blends filled with 2.0% hydroxyapatite was not significant as indicated by the polynomial fitting (see **SJ** in **figure 4.14**). The sample gains about 100% of its initial elongation in 10 days and did not show any deviation in 60 days**.** Sample SS gained 0% of its initial elongation in 10 days and about 50% in 60 days and show a correlation and a deviation on polynomial fitting. Sample SI gained about 75% of its initial elongation at 10 days and 175%

in 60 days. It can be observed that the higher the diffusion coefficient the lower the gain in percentage absorption. The α-amylase in PBS solution hydrolyse the 1, 4 linkage of the starch and attaches hydroxyl groups to C1 position and another to C6 position of the ring forming two glucose molecules. The two glucose linked to each other through extended hydrogen bonding as illustrated in **Appendix G.** The addition of 1.5% by parts of hydroxyapatite into the blend increases the extended hydrogen bonding and linked the chain linearly. The new structure now resembles that of cellulose, accounting for the lowest strength lost and a high elongation at break of sample SI. Doping the blend with 2.0% by part of hydroxyapatite introduces more hydroxyl groups to decrease the extended hydrogen bonding between the glucose molecules and thus increases hydrophilicity and the strength lost while decreasing elongation at break. The gain in elongation is an improvement in ductility of the blend which will be an advantage in application for bone fixation since the blends can withstand high strain failure under plastic deformation. Ductile materials have a moderate ultimate stress which is preferable for structural implant purposes as compared to brittle materials with high ultimate stress and high modulus.

5.4 Assessment of Applicability of Blend to Fracture Fixation

Fracture fixation application uses biomaterials that can help revived the structural integrity of the bone when injured. The achievement of this objective depends mainly on an interplay of material properties. The obvious clinical requirement is that the mechanical properties of the material should be appropriate in order to be used in fixing fracture and sustain reduction (**Smith, 1985**).

The stress- strain curve has been used to determine the mechanical properties of the specimen for fracture fixation. Tensile modulus, tensile strength and percentage elongation were obtained. These mechanical properties are important as they determine the behaviour of a

material when carrying load. The gain of 175% of initial elongation at 60 days for the blend filled with 1.5% by parts of hydroxyapatite (SI) and low tensile modulus lesser than that of the cortical bone (see **Table 2.3**) makes it suitable candidate for fracture fixation application. The low modulus will prevent stress-shielding and the high elongation indicates ductility which checks sudden impacts that might results in fracture. Sample SJ has high tensile strength and high modulus than Sample SI but did not show any significant change in its initial elongation. Sample SJ for example will return a low breaking strain whiles Sample SI will have a larger ultimate strain.

Another important consideration is that the degradation process of the implant must not significantly weakens the mechanical strength of the implant and should not control the release of by products that might elicit deleterious immune response. Blend filled with 1.5% by parts of hydroxyapatite lost 10.41% of its tensile strength after 60 days and comparing poly (lactic acid) (PLA) and poly (glycolic) acid (PGA) which are the current ideal standards for biodegradable implants. The blend has potential to be used as implant since it strength lost is in intermediate of PGA which completely lost its strength between 30 – 60 days and PLA which take about ten years to lose its final strength.

Chapter six

Conclusion and Recommendation(s)

6.1 Conclusion

LLDPE/starch composites have been synthesised by injection moulding. The composite showed higher tensile modulus than the moulded LLDPE alone but compromise in tensile strength. The high modulus was attributed to the structure evolvement of the monoclinic phase of LLDPE due to starch flow in the amorphous phase of LLDPE. In order to improve on the tensile properties of the blend for bone fixation application, hydroxyapatite was introduced as a compatiblizer to enhance the intermediate phase and control the blend degradation through hydroxyl groups interactions. The results obtained show that the structure, morphology and tensile properties of the composites are dependent on the amount of hydroxyapatite introduced into the blends.

Introduction of 1.0% by parts of hydroxyapatite does not affect the crystallinity but is rather suspected to elongate amorphous phase tie chain of the LLDPE and then enhance the tensile modulus. Further increase of hydroxyapatite to 1.5% and 2.0% by parts increases the crystallinity, and results in improvement in the tensile properties. The results obtained show that the tensile properties and degradation of the blends are dependent on the amount of hydroxyapatite introduced into the blend. The introduction of 1.5% by parts of hydroxyapatite into the blend provided the required intermediate thickness to mediate the blend thereby improving tensile properties. The presences of 1.5% by parts of hydroxyapatite in the blend served to slow the degradation of the blends and showed a lower strength lost and a higher gain in percentage elongation at break and this has been explained to be due to amylase-hydrolysis

changing the starch structure to linearly linked glucose chains. The gain in elongation at break suggests that the material may be a promising candidate for bone fixation application since the blend ductility has been modified.

.

6.2 Recommendations

Work done so far in this research work has demonstrated that 1.5% by parts of hydroxyapatite into LLDPE/starch (40 w/v) blends slow the biodegradation and improves the blend ductility, with moderate ultimate strength for bone fixation application. The presence of hydroxyapatite has been explained to enhance the intermediate phase of the blend. Further studies could be done using thermal analytical techniques, like differential scanning calorimetry (DSC) to study the blend thermodynamic properties after which static and cyclic biomechanical test methods could be developed for the purpose of investigating the fixation properties of the biodegradable bone fixation plate-screw constructs and performing *in vivo* studies with animals.

References

Alamo, R., London, J., Mandelkern, L., Stehling, F. and Wignall, G. (1994). Phase behavior of blends of linear and branched polyethylenes in the molten and solid states by small-angle neutron scattering. Macromolecules, 27(2), pp. 411–417.

Alberta Araújo, M., Cunha, A. M. and M. (2004). Enzymatic degradation of starch-based thermoplastic compounds used in protheses: identification of the degradation products in solution. Biomaterials, 25(13), pp. 2687–2693.

Appendini, P. and Hotchkiss, J. H. (2002). Review of antimicrobial food packaging. Innovative Food Science & Emerging Technologies, 3(2), pp. 113–126.

Araki, T., Mitsuhiro, S. and Tran-Cong, Q. (1998). Structure and properties of multiphase polymeric materials (eds, Vol. 46). CRC Press.

Arkatkar, A., Arutchelvi, J., Sudhakar, M., Bhaduri, S., Uppara, P. and Doble, M. (2009). Approaches to enhance the biodegradation of polyolefins. The Open Environmental Engineering Journal, 2, pp. 68–80.

Arutchelvi, J., Sudhakar, M., Arkatkar, A., Doble, M., Bhaduri, S. and Uppara, P. V. (2008). Biodegradation of polyethylene and polypropylene. Indian Journal of Biotechnology, 7(1), p. 9.

Askeland, D. R. and Phulé, P. P. (2003). The science and engineering of materials.

Avérous, L. (2004). Biodegradable multiphase systems based on plasticized starch: a review. Journal of Macromolecular Science, Part C: Polymer Reviews, 44(3), pp. 231–274.

Azevedo, H. S. and Reis, R. L. (2005). Understanding the enzymatic degradation of biodegradable polymers and strategies to control their degradation rate. In Biodegradable systems in tissue engineering and regenerative medicine. Boca Raton, FL: CRC Press, pp. 177–201.

Babu, R. and Seeram, R. (2013). Current progress on bio-based polymers and their future trends. Progress in Biomaterials, 2(8).

Bang Lee, H., Khang, G. and Ho Lee, J. (2000). Polymeric biomaterials: The biomedical engineering handbook. Second Edition. Ed. Joseph D. Bronzino, Boca Raton: CRC Press LLC.

Bertolini Andréa, C. (2010). Trends in starch applications. Starches: characterization, properties and applications.

Böstman, O. and Pihlajamäki, H. (2000). Clinical biocompatibility of biodegradable orthopaedic implants for internal fixation: a review. Biomaterials, 21(24), pp. 2615–2621.

Bowden, P. B. and Young, R. J. (1974). Deformation mechanisms in crystalline polymers. Journal of Materials Science, 9(12), pp. 2034–2051.

Bronzino, E. J. (2000). Billotte, WG "Ceramic Biomaterials." The Biomedical Engineering Handbook:Ed. Joseph D. Bronzino Boca Raton: (second). CRC Press LLC,.

Brydson, J. A. (1999). Plastics materials. Butterworth-Heinemann.

Carraher Jr, C. E. (2013). Carraher's polymer chemistry. CRC Press.

Chaubal, M. ., Su, G., Spicer, E., Dang, W., Branham, K. ., English, J. P. and Zhao, Z. (2003). In vitro and in vivo degradation studies of a novel linear copolymer of lactide and ethylphosphate. Journal of Biomaterials Science, Polymer Edition, 14(1), pp. 45–61.

Chrissafis, K., Paraskevopoulos, K., Tsiaoussis, I. and Bikiaris, D. (2009). Comparative study of the effect of different nanoparticles on the mechanical properties, permeability, and thermal degradation mechanism of HDPE. Journal of Applied Polymer Science, 114(3), pp. 1606–1618.

Clarke, B. (2008). Normal bone anatomy and physiology. Clinical Journal of the American Society of Nephrology, 3 (Supplement 3), pp. S131–S139.

Cláudia, T. K., João, C. L. and Patrícia, B. P. (2012). The quantification of crystalline phases in materials. Dr. Volodymyr Shatokha (Ed.).

Correlo, V. M., Boesel, L. F., Bhattacharya, M., Mano, J. F., Neves, N. M. and Reis, R. L. (2005). Hydroxyapatite reinforced chitosan and polyester blends for biomedical applications. Macromolecular Materials and Engineering, 290(12), pp. 1157–1165.

Crank, J. (1975). Mathematics of Diffusion (Second). Great Calendron Street Oxford OX2 6DP: Oxford University Press.

Danjaji, I., Nawang, R., Ishiaku, U., Ismail, H. and Mohd Ishak, Z. A. (2002). Degradation studies and moisture uptake of sago-starch-filled linear low-density polyethylene composites. Polymer Testing, 21(1), pp. 75–81.

Dorozhkin, S. V. (2011). Biocomposites and hybrid biomaterials based on calcium orthophosphates. Biomaterials, 1(1), pp. 3–56.

Durlofsky, L. and Brady, J. (1987). Analysis of the Brinkman equation as a model for flow in porous media. Physics of Fluids, 30(11), pp. 3329–3341.

Elias, L., Fenouillot, F., Majesté, J. C. and Cassagnau, P. (2007). Morphology and rheology of immiscible polymer blends filled with silica nanoparticles. Polymer, 48(20), pp. 6029–6040.

Fabunmi, O. O., Tabil, L. G., Chang, P. R. and Panigrahi, S. (2007). Developing biodegradable plastics from starch. American Society of Agricultural and Biological Engineers, Fargo, North Dakota, USA.

Feldman, D. (1996). Synthetic polymers: technology, properties and applications.

Fredriksson, H., Silverio, J., Andersson, R., Eliasson, A. C. and Åman, P. (1998). The influence of amylose and amylopectin characteristics on gelatinization and retrogradation properties of different starches. Carbohydrate Polymers, 35(3), pp. 119–134.

Galeski, A. (2003). Strength and toughness of crystalline polymer systems. Progress in Polymer Science, 28(12), pp. 1643–1699.

Gedde, U. W. and Alessandro, M. (2004). Polyethylene morphology.“ Long Term Properties of Polyolefins.” Springer Berlin Heidelberg, pp. 29–74.

Gergely, G., Lukács, I., Mihály, J. and Balazsi, C. (2009). Investigation of nano hydroxyapatite prepared from eggshell and seashell. Presented at the E-MRS Fall Meeting, Warsaw University, Polland.

Gilan, I., Hadar, Y. and Sivan, A. (2004). Colonisation, biofilm formation and biodegradation of polyethylene by a strain of Rhodococcus ruber. Applied Microbiology and Biotechnology, 65, pp. 97– 104.

Gleiter, H. (2000). Nanostructured materials: basic concepts and microstructure. Acta Materialia, 48(2), pp. 1–29.

Guo, S. and Ait-Kadi, A. (2002). A study on weld line morphology and mechanical strength of injection molded polystyrene/poly (methyl methacrylate) blends. Journal of Applied Polymer Science, 84(10), pp. 1856–1865.

Harper, C. A. (2002). Handbook of plastics, elastomers and composites (fourth edition). New York: McGraw-Hill.

Henderson, A. M. (1993). "Ethylene-vinyl acetate (EVA) copolymers: a general review,." IEEE Electrical Insulation Magazine, 9(1), p. 30.

Hooper, K. A., Macon, N. D. and Kohn, J. (1998). Comparative histological evaluation of new tyrosine-derived polymers and poly L-lactic acid) as a function of polymer degradation. Journal of Biomedical Materials Research, 41(3), pp. 443–454.

Hoover, R. (2001). Composition, molecular structure, and physicochemical properties of tuber and root starches: a review. Carbohydrate Polymers, 45(3), pp. 253–267.

Hoque, M. E., Ye, T. J., Yong, L. C. and Mohd Dahlan, K. (2013). Sago starch-mixed low-density polyethylene biodegradable polymer: Synthesis and characterization. *Journal of Materials, 2013*.

Ibos, L., Candau, Y. and Thomas, S. (2011). Handbook of multiphase polymer systems. Eds, Chichester: Wiley, 455.

Imre, B. and Pukánszky, B. (2013). Compatibilization in bio-based and biodegradable polymer blends. European Polymer Journal, 49(6), pp. 1215–1233.

Joshua, J. J. (2012). Adverse local tissue responses to MoM hip implants. AAOS Now. Retrieved from

http://www.aaos.org/news/aaosnow/may12/clinical1.asp

Karim, A. A., Norziah, M. H. and Seow, C. C. (2000). Methods for the study of starch retrogradation. Food Chemistry, 71(1), pp. 9 – 36.

Keller, A., Sirivithayapakorn, S. and Chrysikopoulos, C. V, C. V. (2004). Early breakthrough of colloids and bacteriophage MS2 in a water-saturated sand column. Water Resources Research, 40(8).

Khonakdar, H. A., Morshedian, J., Wagenknecht, U. and Jafari, S. (2003). An investigation of chemical crosslinking effect on properties of high-density polyethylene Polymer, 44(15), pp. 4301–4309.

Kobera, M. (2008). Brinkman equations as a model for flows in porous media. In: WDS'08 Proceedings of Contributed Papers, Part III. Prague: MATFYZPRESS, pp. 38 – 43.

Kolgjini, B., Gustaaf, S. and Paul, K. (2011). Three-phase characterization of uniaxially stretched linear low-density polyethylene. International Journal of Polymer Science.

Kontakis, G., Pagkalos, J., Tosounidis, T., Melissas, J. and Katonis, P. (2007). Bioabsorbable materials in orthopaedics. Acta Orthopaedica Belgica, 73(2), p. 159.

Kotek, R. (2008). Recent advances in polymer fibers. Polymer Reviews, 48(2), pp. 221–229.

Kurtz, S. M. (2009). UHMWPE biomaterials handbook: ultra-high molecular weight polyethylene in total joint replacement and medical devices. Academic Press.

Lee, B. J., Argon, A. S., Parks, D. M., Ahzi, S. and Bartczak, Z. (1993). Simulation of large strain plastic deformation and texture evolution in high density polyethylene. Polymer, 34(17), pp. 3555–3575.

Lee, B. J., Parks, D. M. and Ahzi, S. (1993). Micromechanical modeling of large plastic deformation and texture evolution in semi-crystalline polymers. Journal of the Mechanics and Physics of Solids, 41(10), pp. 1651–1687.

Leja, K. and Lewandowicz, G. (2010). Polymer biodegradation and biodegradable polymers—a review. Pol J Environ Stud, (19), pp. 255–66.

Lemonds, J., Asaro, R. J. and Needleman, A. (1985). A numerical study of localized deformation in bi-crystals. Mechanics of Materials, 4(3), p. 417.

Li, D., Garmestani, H., Kalidindi, S. R. and Alamo, R. (2001). Crystallographic texture evolution in high-density polyethylene during uniaxial tension. Polymer, 42(11), pp. 4903–4913.

Lohse, D. J. (2005). The influence of chemical structure on polyolefin melt rheology and miscibility. Journal of Macromolecular Science, Part C: Polymer Reviews, 45(4), pp. 289–308.

Lu, D. R., Xiao, C. M. and Xu, S. J. (2009). Starch-based completely biodegradable polymer materials. Express Polymer Letters, 3(6), pp. 366–375.

Lustig, S., Mack, N. M., Schuetz, J. M. and Vicik, S. J. (1989). Puncture resistant, heat-shrinkable films containing very low density polyethylene. U.S. Patent 4,863,769.

Marques, A. P., Reis, R. L. and Hunt, J. A. (2002). The biocompatibility of novel starch-based polymers and composites: in vitro studies. Biomaterials, 23(6), pp. 1471–1478.

Matzinos, P., Bikiaris, D., Kokkou, S. and Panayiotou, C. (2001). Processing and characterization of LDPE/starch products. Journal of Applied Polymer Science, 79(14), pp. 2548–2557.

McFaddin, D. C., Russell, K. E., Wu, G. and Heyding, R. (1993). Characterization of polyethylenes by x-ray diffraction and 13C-NMR:Temperature studies and the nature of the amorphous halo. Journal of Polymer Science Part B: Polymer Physics, 32(2), pp. 175–183.

McGlashan, S. A. and Halley, P. J. (2003). Preparation and characterisation of biodegradable starch-based nanocomposite materials. Polymer International, 52(11), pp. 1767–1773.

Men, Y., Jen, R. and Gert, S. (2003). Role of the entangled amorphous network in tensile deformation of semicrystalline polymers. Physical Review Letters, 91(9), 095502.

Mourad, A. H., Fouad, H. and Elleithy, R. (2009). Impact of some environmental conditions on the tensile, creep-recovery, relaxation, melting and crystallinity behaviour of UHMWPE-GUR 410-medical grade. Materials and Design, 30(10), pp. 4112–4119.

Müller, R. J. (2005). Biodegradability of polymers: Regulations and methods for testing. Biopolymers Online.

Nakamae, K. and Nishino, T. (1989). High modulus polymers. Polymer News, 14(6), pp. 179–181.

Nakano, T., Awazu, T. and Umakoshi, Y. (2001). Plastic deformation and operative slip system in mineral fluorapatite single. Scripta Mater, 44(44), pp. 811–815.

Nikolov, S. and Issam, D. (2000). A micro/macro constitutive model for the small-deformation behavior of polyethylene. Polymer, 41(5), pp. 1883–1891.

Nwabunma, D. and Thein, K. (2008). Polyolefin composites. John Wiley & Sons.

Pandey, J., Raghunatha Reddy, K., Pratheep Kumar, A. and Singh, R. . (2005). An overview on the degradability of polymer nanocomposites. Polymer Degradation and Stability, 88(2), pp. 234–250.

Papanicolaou, G., Kosmidou, T. and Vatalis, A. (2006). Water absorption mechanism and some anomalous effects on the mechanical and viscoelastic behavior of an epoxy system. Journal of Applied Polymer Science, 99(4), pp. 1328–1339.

Pawlak, A. and Galeski, A. (2005). Plastic deformation of crystalline polymers: The role of cavitation and crystal plasticity. Macromolecules, 38(23), pp. 9688–9697.

Peacock, A. (2000). Handbook of polyethylene: structures: properties, and applications. CRC Press.

Petermann, J. (1991). The Formation of Microstructures morphologies) in Ultra-thin Films of Semi-crystalline Polymers (Commemoration Issue Dedicated to Professor Ken-ichi Katayama On the Occasion of His Retirement). Bulletin of the Institute for Chemical Research, Kyoto University, 69(2), pp. 84–91.

Pillai, O. and Panchagnula, R. (2001). Polymers in drug delivery. Current Opinion in Chemical Biology, 5(4), pp. 447–451.

Pollack, S. S., Robinson, W. H., Chiang, R. and Flory, P. J. (1962). X-Ray Diffraction of Linear Polyethylene Crystallized at 131° C. Journal of Applied Physics, 33(1), pp. 237–238.

Ramis, X., Cadenato, A., Salla, J., Morancho, J., Valles, A., Contat, L. and Ribes, A. (2004). Thermal degradation of polypropylene/starch-based materials with enhanced biodegradability. Polymer Degradation and Stability, 86(3), pp. 483–491.

Ravve, A. (2012). Principles of polymer chemistry. Springer.

Rivero, I. E., Balsamo, V. and Müller, A. J. (2009). Microwave-assisted modification of starch for compatibilizing LLDPE/starch blends. *Carbohydrate Polymers*, *75*(2), pp. 343–350.

Rodrigues, C. V. M., Serricella, P., Linhares, A. B. R., Guerdes, R. M., Borojevic, R., Rossi, M. A. and Farina, M. (2003). Characterization of a bovine collagen–hydroxyapatite composite scaffold for bone tissue engineering. Biomaterials, 24(27), pp. 4987 – 4997.

Rolla, M. (2012). Advanced water moisture modelling on polymeric composites. In Proceedings of the 6th Annual ISC Graduate Research Symposium.

Rozman, H. D., Abdul Khalil, H. P. S., Chow, W. C., Ismail, H., Ahmad, M. N. and Kumar, R. N. (2001). The effect of anhydride modification of sago starch on the tensile and water absorption properties of sago-filled linear low-density polyethylene (LLDPE). Polymer-Plastics Technology and Engineering, 40(3), pp. 249–263.

Russell, K. E., Hunter, B. K. and Heyding, R. D. (1997). Monoclinic polyethylene revisited. Polymer, 38(6), pp. 1409–1414.

Rutkowska, M., Heimowska, A., Krasowska, K. and Janik, H. (2002). Biodegradability of polyethylene starch blends in sea water. Polish Journal of Environmental Studies, 11(3).

Sadiku-Agboola, O., Sadiku, E. R., Adegbola, A. T. and Biotidara, O. F. (2011). Rheological properties of polymers: structure and morphology of molten polymer blends. Materials Sciences and Applications, 2(1), p. 10.

Sailaja, R. R. N. and Chanda, M. (2001). Use of maleic anhydride–grafted polyethylene as compatibilizer for HDPE–tapioca starch blends: effects on mechanical properties. Journal of Applied Polymer Science, 80(6), pp. 863–872.

Sajkiewicz, P., Hashimoto, T., Saijo, K. and Gradys, A. (2005). Intermediate phase in poly(ethylene) as elucidated by the WAXS.Analysis of crystallization kinetics. Polymer, 46(2), pp. 513–521.

Sedighiamiri, A., Govaert, L. E. and Van Dommelen, J. A. W. (2011). "Micromechanical modeling of the deformation kinetics of semicrystalline polymers." Journal of Polymer Science Part B: Polymer Physics, 49(18), pp. 1297–1310.

Séguéla, R. (2007). Plasticity of semi-crystalline polymers: crystal slip versus melting-recrystallization. E-Polymers, 7(1), pp. 382–401.

Serranti, S. and Bonifazi, G. (2010). Post-consumer polyolefins (PP-PE) recognition by combined spectroscopic sensing techniques. Open Waste Management Journal, 3, pp. 35–45.

Sharif, A., Mohammadi, N. and Ghaffarian, S. R. (2008). Practical work of crack growth and environmental stress cracking resistance of semicrystalline polymers. Journal of Applied Polymer Science, 110(5), pp. 2756–2762.

Simanke, A. G., Alamo, R. G., Galland, G. B. and Mauler, R. S. (2001). Wide-angle X-ray scattering of random metalloceneethylene copolymers with different types and concentration of comonomer. Macromolecules, 34(20), pp. 6959–6971.

Siročić, A. P., Hrnjak-Murgić, Z. and Jelenčić, J. (2012). Evaluation of compatibility in SAN/EPDM blends by determination of the adhesion parameters. Journal of Adhesion Science and Technology.

Sriburi, P., Sandra, E. H. and Fiona, B. (1999). Depolymerisation of cassava starch. Carbohydrate Polymers, 38(3), pp. 211–218.

Subramanian, M. N. (2013). Plastics Additives and Testing. John Wiley & Sons.

Sui, G., Zhong, W., Ren, X., Wang, X. and Yang, X. (2009). Structure, mechanical properties and friction behavior of UHMWPE/HDPE/carbon nanofibers. Materials Chemistry and Physics, 115(1), pp. 404–412.

Teare, P. W. and Holmes, D. R. (1957). Extra reflections in the x-ray diffraction pattern of polyethylenes and polymethylenes. Journal of Polymer Science, 24(107), pp. 496–499.

Thévenon, A. and René, F. (2014). A thermomechanical modeling approach of the structural changes in semi-crystalline polymers under elongational strain. Journal of Materials Science, 49(1), pp. 433–440.

Tokiwa, Y., Calabia, B. P., Ugwu, C. U. and Aiba, S. (2009). Biodegradability of plastics. International Journal of Molecular Sciences, 10(9), pp. 3722–3742.

Tormala, P., Rokkanen, P., Laiho, J., Tamminmaki, M. and Vainionpaa, S. (1988). Material for osteosynthesis devices.

Tracy, M. A., Ward, K. L., Firouzabadian, L., Wang, Y., Dong, N., Qian, R. and Zhang, Y. (1999). Factors affecting the degradation rate of poly (lactide-co-glycolide) microspheres in vivo and in vitro. Biomaterials, 20(11), pp. 1057–1062.

VÄÄNÄNEN, P. (2009). Testing of Biodegradable Bone Fixation Implants (Doctoral dissertation). University of Kuopio. Retrieved from http://core.kmi.open.ac.uk/download/pdf/15168058.pdf

Van Soest, J. J., Hulleman, S. H. D, De Wit, D. and Vliegenthart, J. F. G. (1996). Crystallinity in starch bioplastics. Industrial Crops and Products, 5(1), pp. 11–22.

Van Soest, J. J. and Vliegenthart, J. F. (1997). Crystallinity in starch plastics: consequences for material properties. Trends in Biotechnology, 15(6), 208–213.

Vasenius, J., Vainionpaa, S., Vihtonen, K., Mäkelä, A., Rokkanen, P., Mero, M. and Törmälä, P. (1990). Comparison of in vitro hydrolysis, subcutaneous and intramedullary implantation to evaluate the strength retention of absorbable osteosynthesis implants. Biomaterials, 11(7), pp. 501–504.

Vasile, C. and Pascu, M. (2005). Practical guide to polyethylene. iSmithers Rapra Publishing.

Vieira, M. G. A., da Silva, M. A., dos Santos, L. O. and Beppu, M. M. (2011). Natural-based plasticizers and biopolymer films: A review. European Polymer Journal, 47(3), pp. 254–263.

Vroman, I. and Tighzert, L. (2009). Biodegradable polymers. Materials, 2(2), pp. 307–344.

Wahl, D. A. and Czernuszka, J. T. (2006). Collagen-hydroxyapatite composites for hard tissue repair. European Cell Mater, 11, pp. 43–56.

Waris, E., Ashammakhi, N., Kaarela, O., Raatikainen, T. and Vasenius, J. (2004). Use of bioabsorbable osteofixation devices in the hand. J Hand Surg, 29(6), pp. 590–598.

Watanabe, S., Sano, X., N., Noda, I. and Ozaki, Y. (2009). Surface melting and lamella rearrangement process in linear low density polyethylene. The Journal of Physical Chemistry B, 113(11), pp. 3385–3394.

Yang, W. and Chen, M. X. (2001). Modeling of large plastic deformation in crystalline polymers. *Journal of the Mechanics and Physics of Solids*, *49*(11), pp. 2719–2736.

Yu, L., Dean, K. and Li, L. (2006). Polymer blends and composites from renewable resources. Progress in Polymer Science, 31(6), pp. 576–602.

Zamiri, A. and De, S. (2011). Mechanical properties of hydroxyapatite single crystals from nanoindentation data. Journal of the Mechanical Behavior of Biomedical Materials, 4(2), pp. 146–152.

Zhang, Z. and Fazeli, B. (2010). Mechanical properties of SEVA / hydroxyapatite composite with to HAP different particle sizes. Int. J. Nano. Dim, 1(2), pp. 103–109.

Zhu, L. and Narh, K. A. (2004). Numerical simulation of the tensile modulus of nanoclay-filled polymer composites. Journal of Polymer Science Part B: Polymer Physics, 42(12), pp. 2391–2406.

Zhu, S., Liu, Y., Rafailovich, M. H., Sokolov, J., Gersappe, D., Winesett, D. A. and Ade, H. (1999). Confinement-induced miscibility in polymer blends. Nature, 400(6739), pp. 49–51.

Appendices

Appendix A - XRD pattern characteristics of LLDPE

Name and formula

Reference code:	00-054-1981
Compound name:	Polyethylene
Common name:	polyethene
Empirical formula:	C_2H_4
Chemical formula:	$(C_2H_4)n$

Crystallographic parameters

Crystal system:	Monoclinic
Space group:	C2/m
Space group number:	12
a (Å):	8.0850
b (Å):	2.5440
c (Å):	4.8080
Alpha (°):	90.0000
Beta (°):	108.6400
Gamma (°):	90.0000
Volume of cell (10^6 pm^3):	93.70
RIR:	-

Subfiles and quality

Subfiles:	Organic Polymer
Quality:	Low precision (O)

Comments

Creation Date:	5/9/2002
Modification Date:	1/12/2013
Analysis:	Analysis by WAXS, 23.5% monoclinic, 42.7% orthorhombic phase mixture

Footnotes for D-spacings and Intensities: 1 Orthorhombic phase

Sample Preparation: Hot-extruded or hot-rolled linear polyethylene (from Frank Maine Consulting) was placed in a diamond mortar and was struck once perpendicular to the smallest dimension or a 2x4x20 mm3 sample, reducing that dimension by 40%

Raw Data Comment: Diffraction pattern reproduced from `Dow Polymer Pattern Collection` by optical scanning

Unit Cell Data Source: Powder Diffraction.

References

Primary reference: Russell, K., Hunter, B., Heyding, R., *Polymer*, **38**, 1409, (1997)

Peak list

No.	h	k	l	d [Å]	2Theta[deg]	I [%]
1	0	0	1	4.56370	19.435	30.0
2				4.13300	21.483	100.0
3	2	0	0	3.83870	23.152	18.0
4				3.72310	23.881	35.0
5	-2	0	1	3.54640	25.090	8.0
6				2.97760	29.986	1.0
7	2	0	1	2.55800	35.051	2.0
8				2.47610	36.250	5.0
9	-1	1	1	2.21420	40.717	3.0
10	1	1	1	2.06010	43.914	2.0
11	-4	0	1	2.01110	45.042	1.0
12	4	0	0	1.91680	47.390	1.0
13				1.85650	49.029	1.0

Stick Pattern

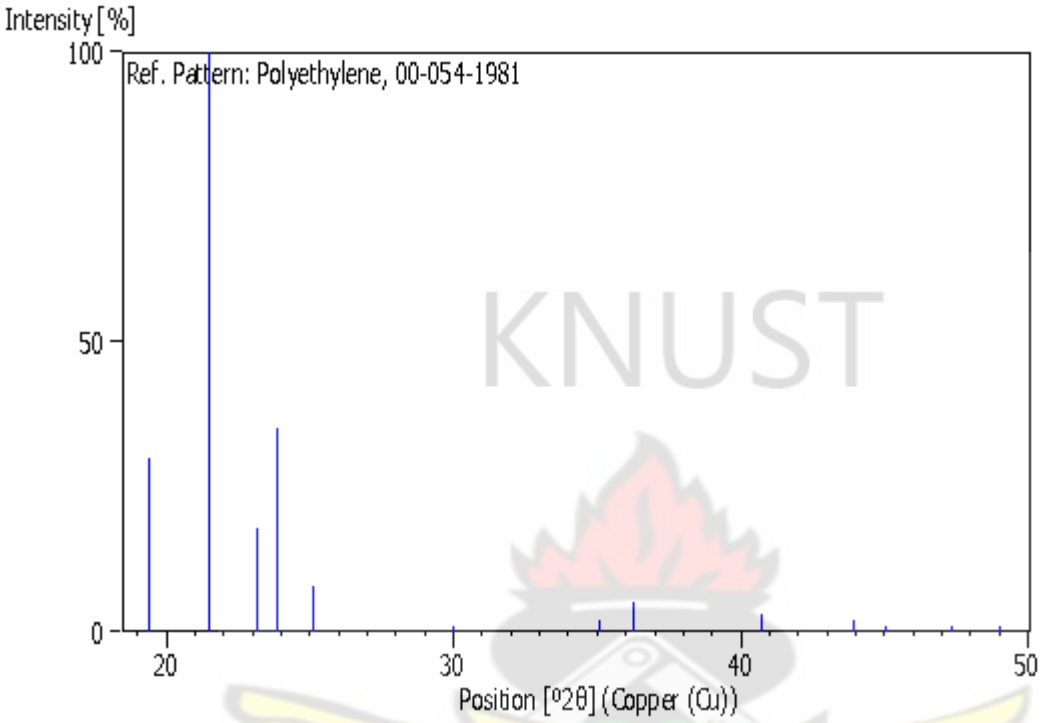

Scan

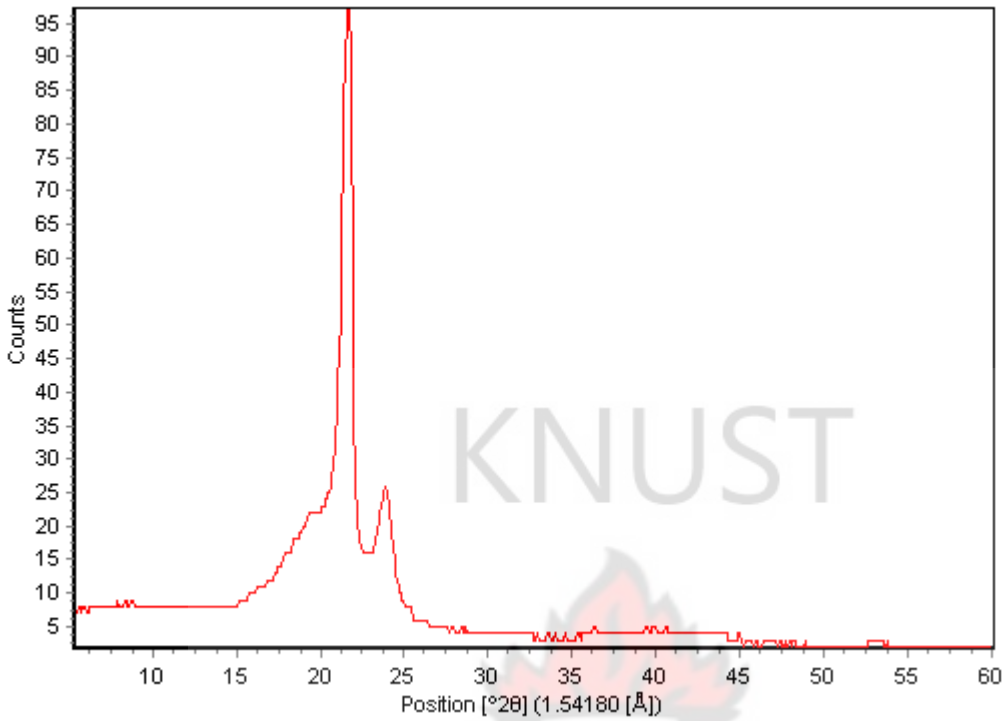
Counts
95
90
85
80
75
70
65
60
55
50
45
40
35
30
25
20
15
10
5
10
15
20
25
30
35
40
45
50
55
60
Position [°2θ] (1.54180 [Å])

Appendix B – XRD pattern characteristics of native cassava starch

Name and formula

Reference code:	00-043-1858
Compound name:	α-Amylose
Empirical formula:	$C_6H_8O_4$
Chemical formula:	($C_6H_8O_4$)n

Crystallographic parameters

Crystal system:	Orthorhombic
Space group:	I
a (Å):	10.6900
b (Å):	11.7200
c (Å):	17.7100
Alpha (°):	90.0000
Beta (°):	90.0000
Gamma (°):	90.0000
Volume of cell (10^6 pm^3):	2218.83
RIR:	-

Subfiles and quality

Subfiles:	Carbohydrates Organic Polymer
Quality:	Star (S)

Comments

Creation Date:	8/20/1992
Modification Date:	1/11/2013
Sample Preparation:	Prepared by hydrolysis of potato starch and recrystallized from water at 60 C with vapor diffusion of acetone to cause precipitation
Unit Cell:	Reference reports: monoclinic B-centered, a=21.24, b=11.72, c=10.69, =123.5. Unit Cell Data Source: Powder Diffraction.

References

Primary reference: Imberty, A., Chanzy, H., Perez, S., Buleon, A., Tran, V., *J. Mol. Biol.*, **201**, 365, (1988)

Peak list

No.	h	k	l	d [Å]	2Theta[deg]	I [%]
1	0	1	1	9.77390	9.041	7.0
2	1	0	1	9.15170	9.657	22.0
3	0	0	2	8.85530	9.981	18.0
4	1	1	0	7.89820	11.194	25.0
5	1	1	2	5.89410	15.019	69.0
6	0	2	0	5.85990	15.107	80.0
7	0	1	3	5.27210	16.803	71.0
8	1	0	3	5.16770	17.145	73.0
9	1	2	1	4.93490	17.960	100.0
10	0	2	2	4.88690	18.138	71.0
11	2	1	1	4.68960	18.908	9.0
12	2	0	2	4.57590	19.382	4.0
13	0	0	4	4.42740	20.039	11.0
14	2	2	0	3.94900	22.497	7.0
15	1	2	3	3.87590	22.927	94.0
16	1	1	4	3.86200	23.010	18.0
17	0	3	1	3.81490	23.298	14.0
18	2	1	3	3.75340	23.686	70.0
19	1	3	0	3.66930	24.237	29.0
20	2	2	2	3.60660	24.665	27.0
21	0	2	4	3.53260	25.190	7.0

Scan

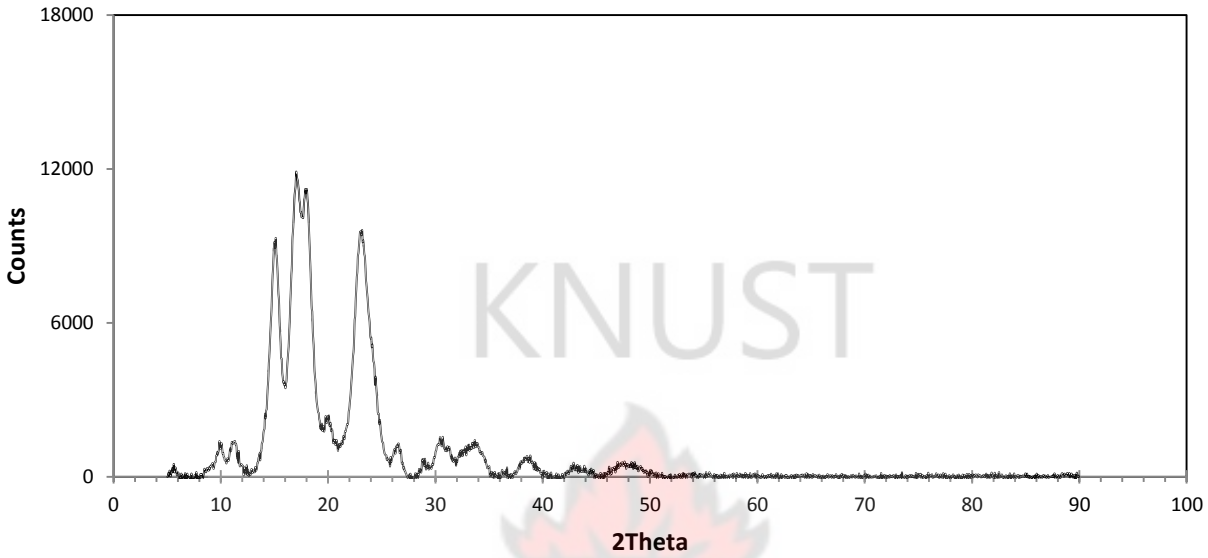

Stick Pattern

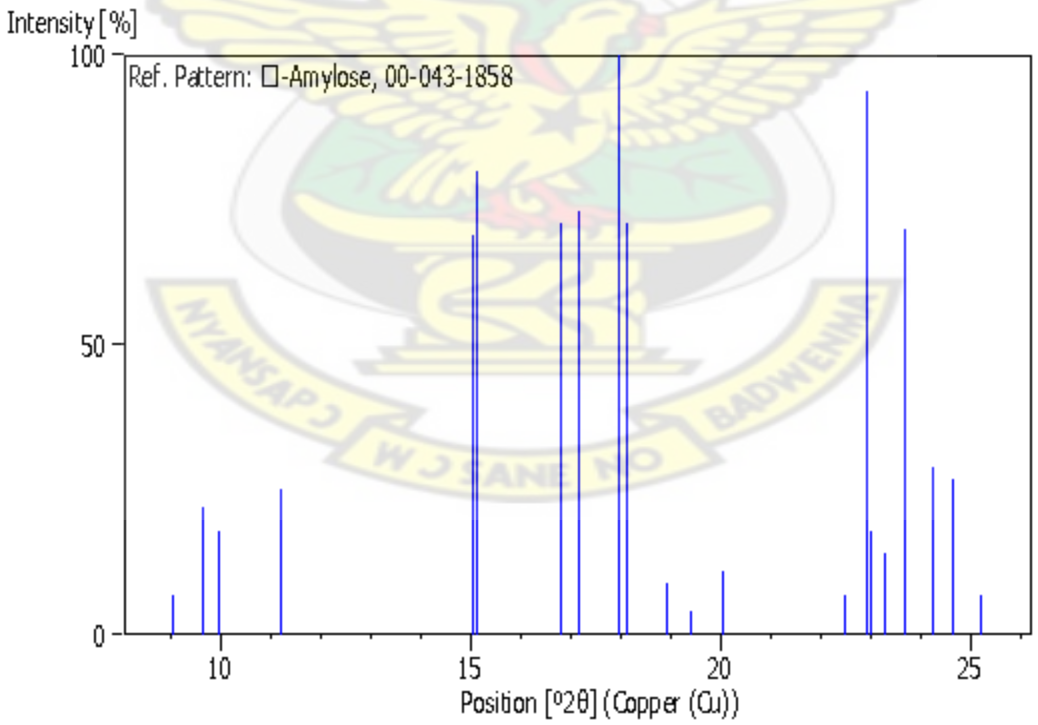

Appendix C - XRD pattern characteristics of hydroxyapatite

Name and formula

Reference code:	01-074-9780
Mineral name:	Hydroxyapatite
Compound name:	Calcium Phosphate Hydroxide
Empirical formula:	$Ca_5HO_{13}P_3$
Chemical formula:	$Ca_5 (PO_4)_3 (OH)$

Crystallographic parameters

Crystal system:	Hexagonal
Space group:	P63/m
Space group number:	176
a (Å):	9.4380
b (Å):	9.4380
c (Å):	6.8870
Alpha (°):	90.0000
Beta (°):	90.0000
Gamma (°):	120.0000
Volume of cell (10^6 pm^3):	531.28
Z:	2.00
RIR:	1.11

Status, subfiles and quality

Status:	Alternate Pattern
Subfiles:	Ceramic
	Common Phase
	Excipient
	Forensic
	ICSD Pattern
	Inorganic
	Mineral
	Pharmaceutical
Quality:	Star (S)

Comments

ANX:	A3B5X13
ICSD collection code:	154315
Creation Date:	7/26/2010
Modification Date:	1/17/2013
ANX:	A3B5X13
Analysis:	H1 Ca5 O13 P3
Formula from original source:	Ca5 (P O4)3 (O H)
ICSD Collection Code:	154315
Wyckoff Sequence:	i h4 f e(P63/M)
Unit Cell Data Source:	Powder Diffraction.

References

Primary reference:	*Calculated from ICSD using POWD-12++*
Structure:	Stork, L., Mueller, P., Dronskowski, R., Ortlepp, J.R., *Z. Kristallogr.*, **220**, 201, (2005)

Peak list

No.	h	k	l	d [Å]	2Theta[deg]	I [%]
1	1	0	0	8.17360	10.815	14.9
2	1	0	1	5.26670	16.820	3.8
3	1	1	0	4.71900	18.789	3.0
4	2	0	0	4.08680	21.729	5.3
5	1	1	1	3.89280	22.826	6.8
6	2	0	1	3.51460	25.321	2.2
7	0	0	2	3.44350	25.852	36.3
8	1	0	2	3.17340	28.096	8.4
9	2	1	0	3.08930	28.877	16.7
10	2	1	1	2.81870	31.719	100.0
11	1	1	2	2.78160	32.154	49.2
12	3	0	0	2.72450	32.846	62.6
13	2	0	2	2.63330	34.018	22.7
14	3	0	1	2.53350	35.401	3.9
15	2	2	0	2.35950	38.109	0.2
16	2	1	2	2.29950	39.143	4.8
17	1	3	0	2.26690	39.730	21.2
18	2	2	1	2.23210	40.376	1.7
19	1	0	3	2.21020	40.794	0.4
20	1	3	1	2.15330	41.922	6.1
21	3	0	2	2.13660	42.265	1.2
22	1	1	3	2.06440	43.818	5.3
23	4	0	0	2.04340	44.292	1.2

24	2	0	3	2.00150	45.270	3.7
25	4	0	1	1.95900	46.309	0.6
26	2	2	2	1.94640	46.626	28.0
27	1	3	2	1.89350	48.009	13.2
28	2	3	0	1.87510	48.511	4.3
29	2	1	3	1.84260	49.423	33.4
30	3	2	1	1.80930	50.396	16.7
31	1	4	0	1.78360	51.174	11.6
32	4	0	2	1.75730	51.996	12.4
33	3	0	3	1.75730	51.996	12.4
34	0	0	4	1.72180	53.151	14.1
35	1	0	4	1.68480	54.414	1.1
36	3	2	2	1.64680	55.777	6.2
37	5	0	0	1.63470	56.227	0.1
38	3	1	3	1.61300	57.052	4.4
39	5	0	1	1.59050	57.935	2.0
40	2	0	4	1.58670	58.087	0.3
41	4	1	2	1.58380	58.203	0.8
42	3	3	0	1.57300	58.642	1.0
43	2	4	0	1.54470	59.824	5.2
44	3	3	1	1.53350	60.306	3.7
45	2	4	1	1.50720	61.472	3.1
46	1	2	4	1.50400	61.617	4.9
47	5	0	2	1.47680	62.879	8.9
48	5	1	0	1.46800	63.300	1.6
49	3	0	4	1.45550	63.907	7.5
50	3	2	3	1.45220	64.070	6.8
51	5	1	1	1.43580	64.891	7.9
52	3	3	2	1.43080	65.145	1.6
53	1	4	3	1.40940	66.260	2.0
54	4	2	2	1.40940	66.260	2.0
55	2	2	4	1.39080	67.264	0.1
56	3	1	4	1.37110	68.362	0.3
57	6	0	0	1.36230	68.866	0.3
58	1	0	5	1.35820	69.103	0.1
59	5	1	2	1.35040	69.559	2.0
60	4	3	0	1.34370	69.957	0.3
61	6	0	1	1.33640	70.395	0.1
62	5	0	3	1.33160	70.687	0.3
63	1	1	5	1.32220	71.266	0.4
64	4	3	1	1.31880	71.478	3.9
65	5	2	0	1.30880	72.109	3.5
66	2	0	5	1.30530	72.333	0.3
67	3	3	3	1.29760	72.831	0.2
68	5	2	1	1.28580	73.608	2.3
69	2	4	3	1.28160	73.890	4.2
70	2	3	4	1.26820	74.803	1.3

71	6	0	2	1.26670	74.907	1.4
72	2	1	5	1.25800	75.515	5.0
73	3	4	2	1.25180	75.955	2.9
74	6	1	0	1.24640	76.343	2.0
75	1	4	4	1.23880	76.897	5.9
76	5	1	3	1.23680	77.044	4.5
77	3	0	5	1.22920	77.609	0.3
78	1	6	1	1.22650	77.812	0.9
79	2	5	2	1.22340	78.047	6.1
80	2	2	5	1.18950	80.719	0.3
81	5	0	4	1.18550	81.048	0.6
82	4	4	0	1.17980	81.522	1.9
83	1	3	5	1.17710	81.749	0.7
84	1	6	2	1.17200	82.181	0.7
85	6	0	3	1.17200	82.181	0.7
86	3	5	0	1.16760	82.558	0.7
87	4	4	1	1.16280	82.974	1.3
88	3	3	4	1.16130	83.105	1.2
89	4	3	3	1.15970	83.245	3.7
90	2	4	4	1.14980	84.125	4.4
91	0	0	6	1.14780	84.305	1.8
92	4	0	5	1.14210	84.824	0.1
93	1	0	6	1.13700	85.295	1.8
94	5	2	3	1.13700	85.295	1.8
95	2	6	0	1.13350	85.621	0.3
96	5	1	4	1.11710	87.189	2.7
97	4	4	2	1.11530	87.366	4.6
98	1	1	6	1.11530	87.366	4.6
99	2	3	5	1.11010	87.879	2.6
100	3	5	2	1.10580	88.310	7.4
101	1	6	3	1.09540	89.371	0.4
102	4	1	5	1.09020	89.913	0.1
103	1	7	0	1.08260	90.719	2.1
104	2	1	6	1.07660	91.367	1.1
105	6	2	2	1.07660	91.367	1.1
106	6	0	4	1.06830	92.283	0.4
107	4	3	4	1.05930	93.301	0.4
108	5	0	5	1.05330	93.994	0.5
109	4	4	3	1.04930	94.464	0.1
110	4	5	0	1.04650	94.796	0.1
111	5	2	4	1.04200	95.335	1.0
112	7	0	3	1.04080	95.480	0.7
113	3	3	5	1.03630	96.029	1.1
114	4	5	1	1.03460	96.239	1.4
115	7	1	2	1.03220	96.536	3.0
116	2	2	6	1.03220	96.536	3.0
117	3	6	0	1.02980	96.836	0.2

118	2	4	5	1.02800	97.063	0.7
119	1	3	6	1.02400	97.570	2.1
120	8	0	0	1.02170	97.865	1.0
121	6	3	1	1.01840	98.292	2.8
122	6	2	3	1.01630	98.567	0.3
123	1	6	4	1.00960	99.454	2.6
124	5	1	5	1.00450	100.143	2.2
125	4	5	2	1.00080	100.651	1.1
126	4	0	6	1.00080	100.651	1.1
127	7	2	0	0.99860	100.956	0.7
128	7	2	1	0.98820	102.429	0.6
129	3	6	2	0.98660	102.661	3.5
130	3	2	6	0.97950	103.705	4.0
131	8	0	2	0.97950	103.705	4.0
132	4	4	4	0.97320	104.654	3.0
133	3	5	4	0.96640	105.704	0.8
134	4	1	6	0.96520	105.893	0.6
135	4	3	5	0.96180	106.431	1.1

Structure

No.	Name	Elem.	X	Y	Z	Biso	sof	Wyck.
1	CA1	Ca	0.33333	0.66666	0.00070	0.5000	1.0000	4f
2	CA2	Ca	0.24260	0.99040	0.25000	0.5000	1.0000	6h
3	P1	P	0.39480	0.36570	0.25000	0.5000	1.0000	6h
4	O1	O	0.32700	0.48490	0.25000	0.5000	1.0000	6h
5	O2	O	0.57910	0.46180	0.25000	0.5000	1.0000	6h
6	O3	O	0.34170	0.25780	0.07110	0.5000	1.0000	12i
7	O4	O	0.00000	0.00000	0.18370	0.5000	0.4650	4e
8	H1	H	0.00000	0.00000	0.06080	0.5000	0.0800	4e

Stick Pattern

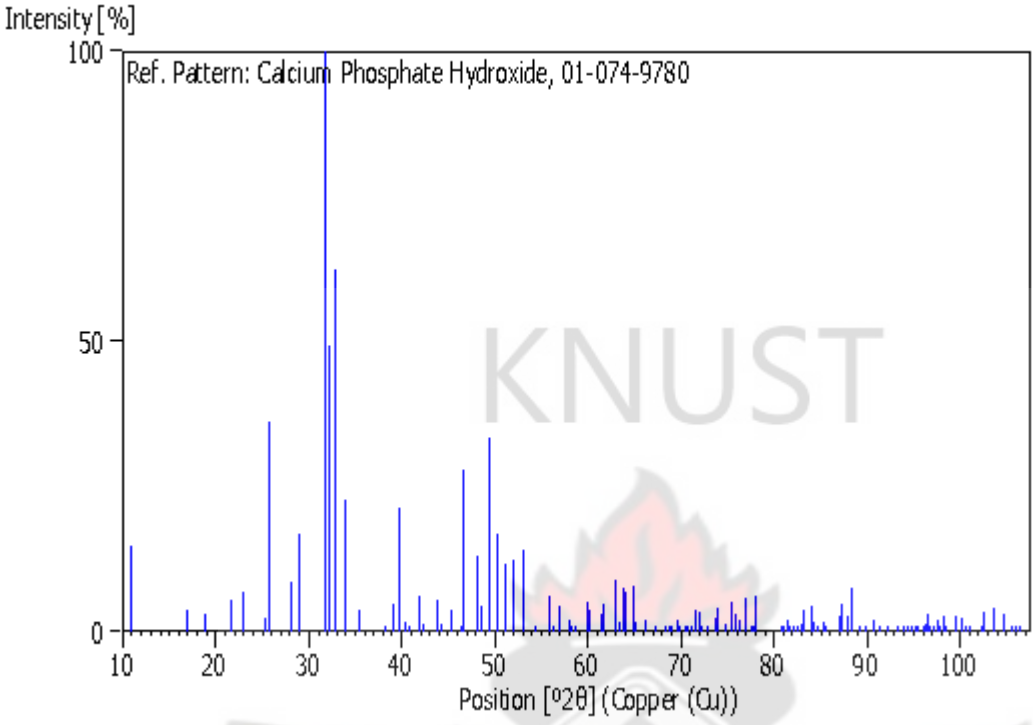

Scan

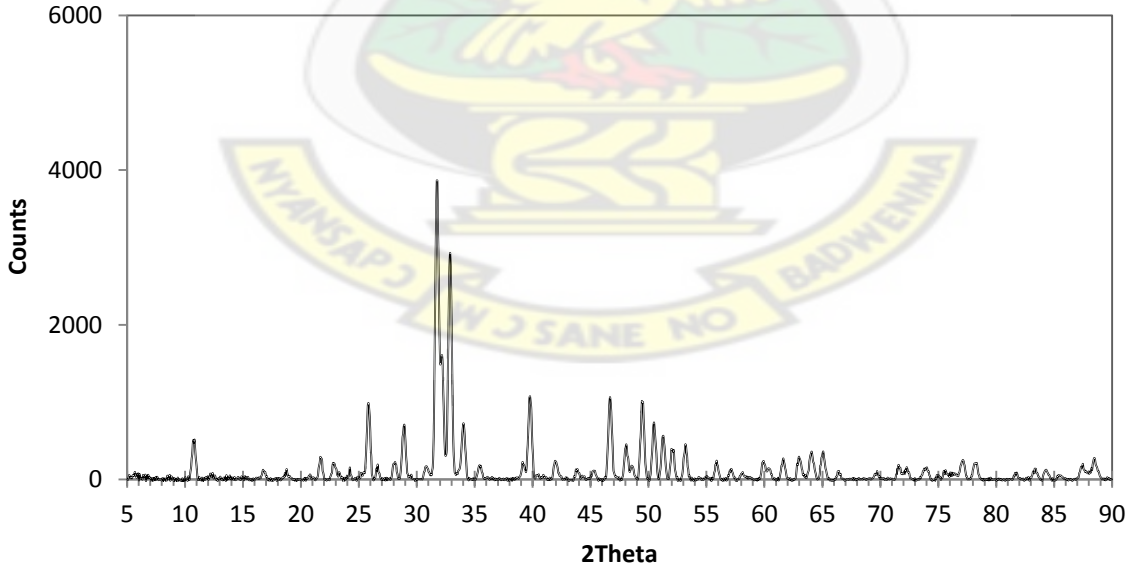

Appendix D – Force - extension curve of samples

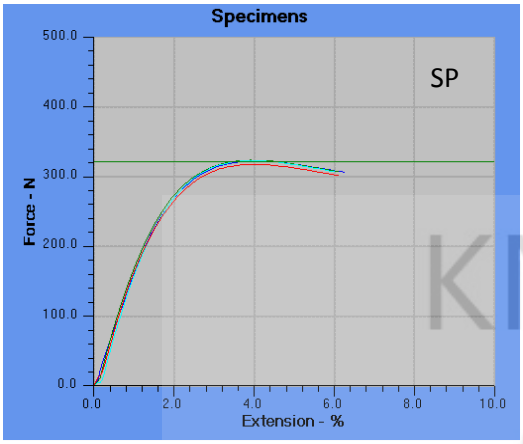

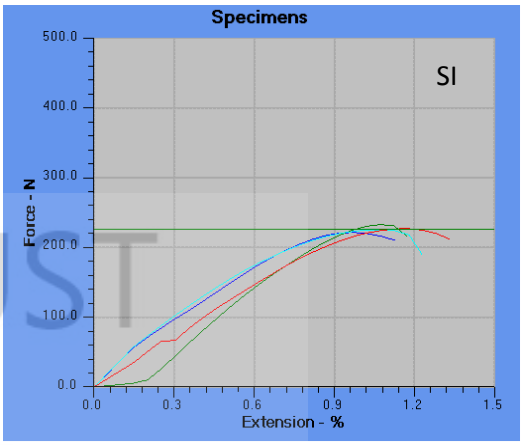

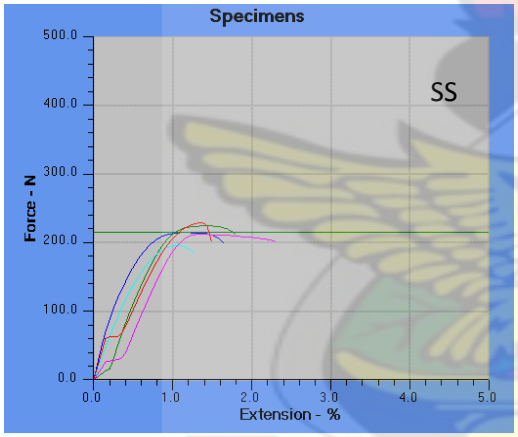

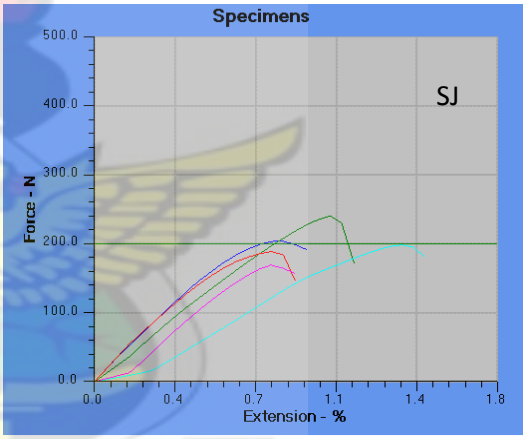

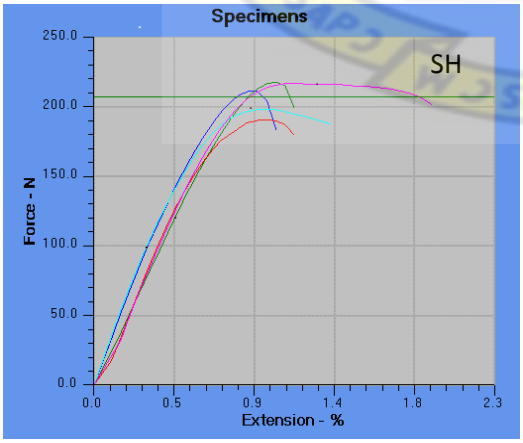

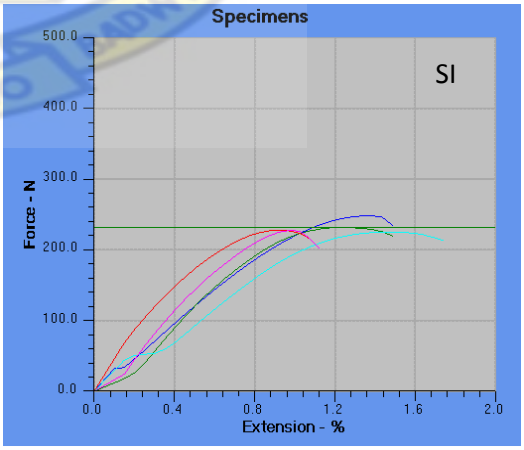

Appendix E – Calculations for percentage water absorption

	day 0			day 5			day 10			day 15			day 20		
No.	25-Jul-14			30-Jul-14			5-Jul-14			10-Jul-14			15-Jul-14		
	SS/ g	**SSI/ g**	**SJ/ g**	**SS/ g**	**SI/g**	**SJ/g**	**SS/g**	**SI/g**	**SJ/g**	**SS/g**	**SI/g**	**SJ/g**	**SS/g**	**SI/g**	**SJ/g**
1	0.74	0.79	0.86	0.81	0.94	0.95	0.78	0.96	0.96	0.79	0.93	1.00	0.78	0.98	0.97
2	0.78	0.78	0.82	0.86	0.84	0.89	0.86	0.88	0.93	0.83	0.89	0.95	0.86	0.90	0.94
3	0.76	0.74	0.81	0.86	0.81	0.88	0.86	0.82	0.90	0.87	0.83	0.92	0.87	0.85	0.92
4	0.79	0.78	0.80	0.86	0.81	0.94	0.90	0.85	0.96	0.89	0.89	0.98	0.91	0.90	0.96
5	0.68	0.80	0.78	0.82	0.93	0.86	0.78	0.97	0.89	0.83	0.96	0.92	0.82	0.95	0.93
6	0.78	0.87	0.80	0.82	0.92	0.91	0.93	0.90	0.94	0.92	0.90	0.96	0.93	0.93	0.95
7	0.77	0.78	0.88	0.89	0.85	0.94	0.90	0.86	0.98	0.93	0.89	0.96	0.93	0.88	0.97
8	0.73	0.84	0.82	0.78	0.91	0.91	0.79	0.93	0.95	0.83	0.96	0.96	0.85	0.96	0.96
9	0.77	0.84	0.84	0.90	0.87	0.93	0.86	0.82	0.94	0.85	0.87	0.98	0.86	0.85	0.95
10	0.83	0.83	0.85	0.94	0.89	0.92	0.95	0.93	0.94	0.96	0.94	0.97	0.95	0.95	0.96
11	0.75	0.80	0.84	0.77	0.84	0.91	0.78	0.86	0.94	0.80	0.89	0.95	0.80	0.88	0.94
12	0.78	0.79	0.82	0.90	0.87	0.89	0.92	0.89	0.93	0.90	0.92	0.95	0.89	0.90	0.91
13	0.76	0.81	0.87	0.85	0.87	0.93	0.92	0.89	0.91	0.89	0.91	0.95	0.90	0.92	0.94
14	0.83	0.77	0.85	0.93	0.82	0.91	0.95	0.84	0.92	0.94	0.84	0.95	0.96	0.84	0.98
15	0.77	0.83	0.86	0.87	0.89	0.93	0.93	0.94	0.91	0.93	0.93	0.93	0.91	0.94	0.93
16	0.76	0.87	0.86	0.94	0.91	0.93	0.96	0.92	0.98	0.93	0.94	0.98	0.94	0.94	0.99
17	0.68	0.80	0.88	0.81	0.87	0.96	0.84	0.89	0.99	0.81	0.85	0.97	0.83	0.86	1.01
18	0.77	0.84	0.85	0.83	0.87	0.93	0.88	0.90	0.96	0.88	0.89	0.97	0.88	0.90	0.97
19	0.74	0.77	0.80	0.84	0.87	0.86	0.81	0.90	0.92	0.81	0.90	0.93	0.84	0.89	0.94
20	0.85	0.80	0.81	0.97	0.90	0.88	0.97	0.89	0.90	0.98	0.91	0.93	1.00	0.90	0.93
MEAN	**0.7660**	**0.8065**	**0.8350**	**0.8625**	**0.8740**	**0.9130**	**0.8785**	**0.8920**	**0.9375**	**0.8785**	**0.9020**	**0.9555**	**0.8855**	**0.9060**	**0.9525**
STDEV	**0.0414**	**0.0335**	**0.0287**	**0.0538**	**0.0371**	**0.0278**	**0.0629**	**0.0412**	**0.0277**	**0.0559**	**0.0354**	**0.0213**	**0.0556**	**0.0387**	**0.0241**
STDERROR	**0.0093**	**0.0075**	**0.0064**	**0.0120**	**0.0083**	**0.0062**	**0.0141**	**0.0092**	**0.0062**	**0.0125**	**0.0079**	**0.0048**	**0.0124**	**0.0086**	**0.0054**
U= (W_w-W_d)				0.0965	0.0675	0.078	0.1125	0.0855	0.1025	0.1125	0.0955	0.1205	0.1195	0.0995	0.1175
U*100				9.65	6.75	7.80	11.25	8.55	10.25	11.25	9.55	12.05	11.95	9.95	11.75
% Water Absorbed = (U*100)/W_d				**12.5979**	8.3695	**9.3413**	**14.6867**	10.6014	**13.3812**	**14.6867**	11.8413	**14.4311**	**15.6005**	**12.3373**	**14.0719**

Appendix E (continues)

day 30			day 60			day 90			day 120		
25-Jul-14									25-Nov-14		
SS/g	**SI/g**	**SJ/g**	**SS/g**	**SI/g**	**SJ/g**	**SS/g**	**SI/g**	**SJ/g**	**SS/g**	**SI/g**	**SJ/g**
0.78	0.96	0.98	0.79	0.94	0.99	0.82	0.87	0.98	0.83	0.85	1.00
0.88	0.91	0.93	0.87	0.91	0.93	0.90	0.90	0.93	0.89	0.90	0.93
0.88	0.87	0.91	0.88	0.87	0.93	0.88	0.86	0.92	0.89	0.86	0.93
0.91	0.89	0.95	0.91	0.89	0.95	0.93	0.89	0.97	0.94	0.90	0.97
0.87	0.97	0.93	0.87	0.97	0.93	0.88	0.96	0.91	0.87	0.96	0.91
0.92	0.91	0.92	0.92	0.91	0.96	0.93	0.95	0.92	0.94	0.96	0.93
0.94	0.90	0.99	0.94	0.91	0.99	0.94	0.91	0.97	0.93	0.91	1.01
0.83	0.94	0.95	0.84	0.94	0.96	0.84	0.96	0.97	0.85	0.98	0.97
0.88	0.87	0.96	0.89	0.87	0.96	0.87	0.89	0.97	0.88	0.90	0.97
0.98	0.94	0.96	0.98	0.94	0.96	0.98	0.95	0.94	0.99	0.95	0.96
0.79	0.88	0.97	0.80	0.88	0.96	0.83	0.88	0.94	0.83	0.90	0.95
0.92	0.92	0.93	0.91	0.92	0.94	0.94	0.91	0.92	0.93	0.91	0.93
0.92	0.91	0.92	0.93	0.91	0.93	0.93	0.92	0.98	0.92	0.92	0.98
0.98	0.85	0.95	0.98	0.86	0.98	0.98	0.87	0.97	0.98	0.87	0.97
0.94	0.93	0.93	0.94	0.93	0.93	0.93	0.94	0.96	0.93	0.94	0.98
0.95	0.94	0.96	0.96	0.95	0.98	0.95	0.97	0.99	0.95	0.97	0.98
0.86	0.87	0.99	0.86	0.87	1.00	0.85	0.89	1.02	0.84	0.89	1.00
0.89	0.89	0.97	0.89	0.89	0.97	0.91	0.85	0.97	0.91	0.82	0.96
0.88	0.90	0.90	0.89	0.90	0.95	0.87	0.88	0.93	0.85	0.88	0.93
1.00	0.91	0.91	1.00	0.92	0.93	0.99	0.92	0.92	0.99	0.94	0.93
0.9000	**0.9080**	**0.9455**	**0.9025**	**0.9090**	**0.9565**	**0.9045**	**0.9100**	**0.9542**	**0.9070**	**0.9105**	**0.9585**
0.0572	**0.0312**	**0.0264**	**0.0551**	**0.0296**	**0.0224**	**0.0489**	**0.0360**	**0.0275**	**0.0511**	**0.0409**	**0.0267**
0.0128	**0.0070**	**0.0059**	**0.0123**	**0.0066**	**0.0050**	**0.0109**	**0.0081**	**0.0062**	**0.0114**	**0.0092**	**0.0060**
0.1340	0.1015	0.1105	0.1365	0.1025	0.1215	0.1385	0.1035	0.1192	0.1410	0.1040	0.1235
13.40	10.15	11.05	13.65	10.25	12.15	13.85	10.35	11.917	14.10	10.40	12.35
17.4935	**12.5852**	**13.2335**	**17.8198**	**12.7092**	**14.5509**	**18.0748**	**12.8320**	**14.2718**	**18.4125**	**12.9002**	**14.7904**

Appendix F – A proposed mechanism of reaction pathway of the blend with hydroxyapatite mediating through hydrogen bonding. The structure was drawn using ChemDraw Professional 15.0.0.106.

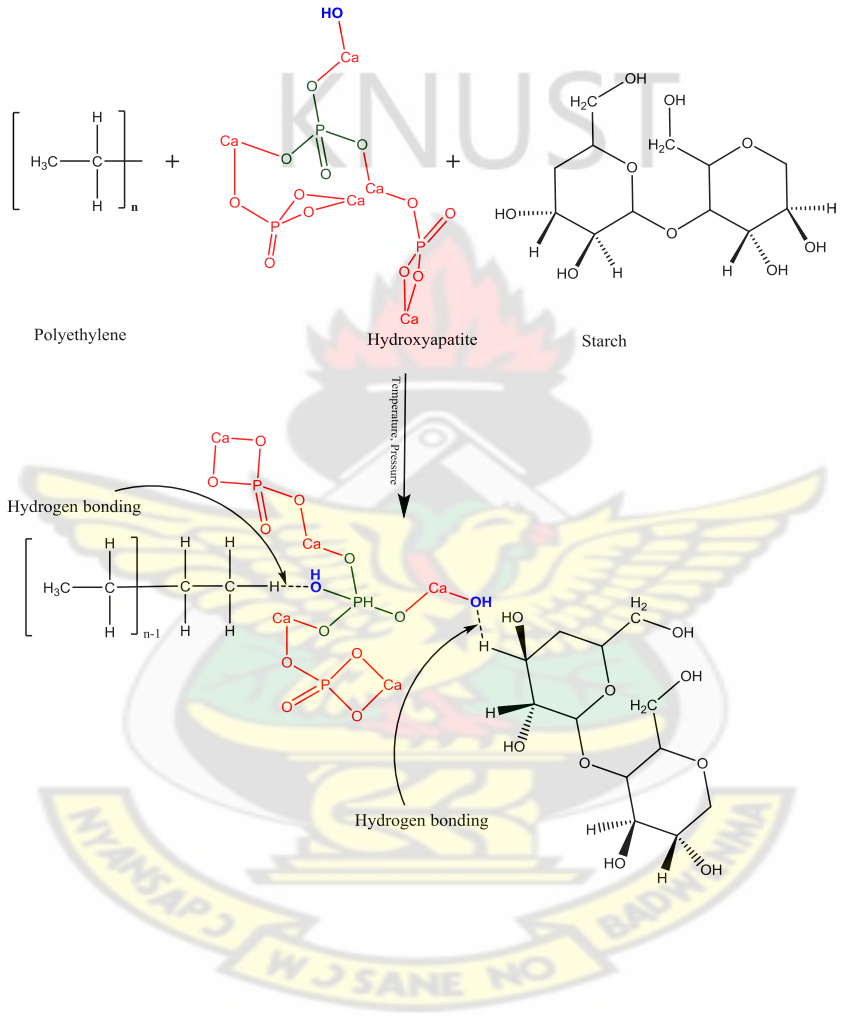

Appendix G

A proposed mechanism of reaction pathway of α-amylase hydrolysis of the blend. The structure were developed using ChemDraw Professional 15.0.0.106.